A molecular simulation study on structural properties and performance investigation of biomimetic artificial water channels

Wu Hao Chen

(Degree)
博士（学術）

(Date of Degree)
2018-03-25

(Date of Publication)
2019-03-01

(Resource Type)
doctoral thesis

(Report Number)
甲第7199号

(URL)
https://hdl.handle.net/20.500.14094/D1007199

Doctoral Dissertation

A molecular simulation study on structural properties and performance investigation of biomimetic artificial water channels

(分子シミュレーションによる生体模倣人工水チャネルの構造特性と性能に関する研究)

January 2018

Graduate school Engineering

Kobe University

WU HAO CHEN

巫 皓臣

Acknowledgement

First, I would like to thank Professor Tomohisa Yoshioka and Hideto Matsuyama. They and their research group provided me the best education and assistance, the working experience with them improved me a lot during these three years. I have been fortunate to meet them in my Ph.D. course period.

I also would like to deliver my gratitude to engineering separation laboratory in Hiroshima. Although, I only studied at Hiroshima University for one year. There were so many wonderful memories not only of research work but also unforgettable experience during my overseas life.

I would like to express appreciation to the committee, Professor Kenji Ishida, and Professor Chiaki Ogino, for their valuable time and judgments.

All members of these group showed great support to me among these three years, they deserve to appreciate. I also have to thank Dr. Abdul Rajjak for the suggestion of simulation software using, the devices and the help to my thesis.

I have been fortunate to meet good friends, Sabrina, every overseas student from Taiwan, and Danran's members, who have been always with me during the good and tough times. I would like to deliver my gratitude to them for their plentiful help and supports.

I deeply appreciate my parents for their selfless love and assistance. They have given the support in every step to help me complete my dreams. I would also like to thank my grandparents and my two sisters for their encouragement and unconditionally love in every stage of my life.

WU HAO CHEN
Kobe University, Japan
January 2018

Contents

Chapter 1

Introduction

1.1 Membrane Process

1.1.1 Introduction of membrane separation

Membrane separation has been widely applied on numerous fields, such as gas separation, water desalination and artificial organs [1]. In simple word, membrane supply separating solvent or particulates from solution [2]. As shown in Fig. 1.1, when feed solution (phase 1) pass through membrane, via the probe size of membrane and different interactions between solvents (particulates) and membrane to achieve the filtration process. Through various driving force, such as concentration difference, electricity potential and pressure drop, with different types of membranes. It can obtain different separation performance base on different requirements. Recently, membrane technique has become an important role, due to the increasing of global population and climate anomaly. With natural resource became more and more precious, membrane separation process shows the high potential on effectively expend or reuse the natural recourse.

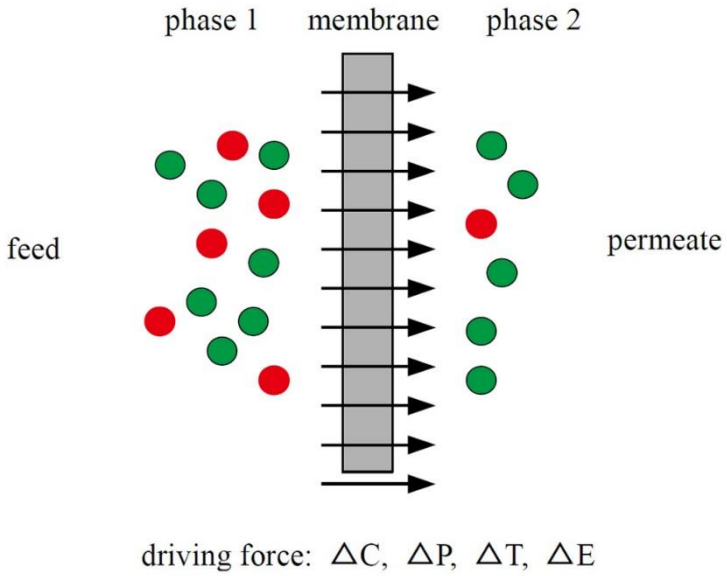

Fig1.1 Membrane separation process in a two-phase system.

1.1.2 Category of membranes

There are many ways to classified membranes [1]. There are flat sheet and hollow fiber membranes, based on different shapes. There are organic, inorganic and organic/inorganic hybrid membranes, based on composition materials. There are symmetric and asymmetric membranes, based on morphology property. Further, with different application, there are solid separation, liquid separation and gas separation membranes and so on. In widely known, microfiltration (MF), ultrafiltration (UF), nanofiltration (NF), reverse osmosis (RO), forward osmosis (FO), electro dialysis (ED), membrane electrolysis (ME), diffusion dialysis (DD), pervaporation (PV), membrane distillation (MD) and membrane contactors (MC), divide membrane categories based on application fields and separation mechanism [3].

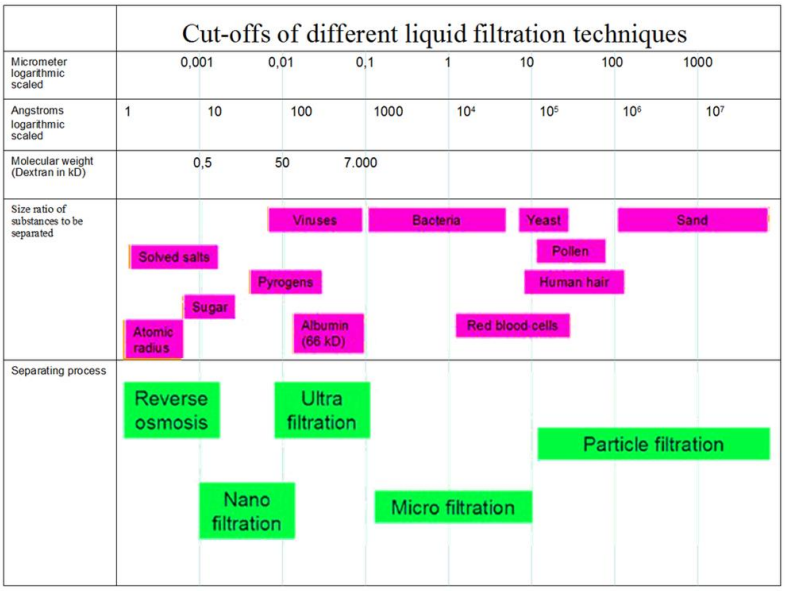

Fig1.2 Common membrane applications and the most used membranes.

Among them, MF, UF, NF and RO have been widely applied on water treatment process. Water treatment is a process to make water acceptable for using. The end of product could be as drinking water, agriculture irrigation…etc. Desalination through artificial water channel on forward osmosis process is introduced in this work. Desalination is a process to remove undesirable components from sea water so as to obtain suitable water for human live using. The brief introduction of desalination via membrane process is introduced in the next chapter.

1.2 Membrane process on water desalination

Desalination is a process to separate minerals from salt water. Through desalination process, salt water is expected to suitable as human drinking water or agriculture irrigation. In simple word, through desalination process to recycle wastewater for effective using the fresh water resource is attracted a lot of interest in recent day [4]. Due to the energy

consumption, the cost of desalinating sea water is much higher than fresh water from ground-water of rivers. However, with the global population increasing, and environment pollution, the problem of water scarcity became a serious problem. Desalination technology was expected to supply as much as 100 million m^3/d of potable water in 2015 [5, 6]. The amount of drinking water required and supplied by utilizing membrane processes will continue to increase in the future. From the increasing percentage, we can see the potential of desalination on sea water desalination or waste water recycling to solve the water scarcity problem.

1.2.1 Reverse osmosis

In recent day, among the membrane process on desalination, reverse osmosis (RO) is mainly applied on desalting salt water [4, 7]. In RO membrane processes, employing semipermeable membranes and applied external pressure on feed side, permeate water pass through the membrane and rejecting salts simultaneously, as shown in Fig. 1.3. Another problem of reverse osmosis process is equipment maintenance. Ionic contamination, viruses, and bacteria…etc. may destroy the reverse osmosis membrane. To prevent damage, some pretreatment sates is necessary such as anti-scaling inhibitors and regular membrane cleaning. Although the cost of seawater desalination is higher than traditional water resource at present day, the cost is expected to decrease with the improvement of technology [8-11].

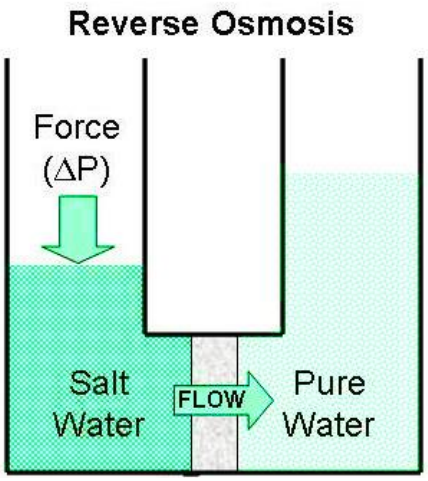

Fig1.3 Water flow direction for reverse osmosis process.

1.2.2 Forward osmosis

Forward osmosis (FO) method is an osmotic process similar with reverse osmosis process, by using semi-permeable membrane to separate water from mineral components [12]. Osmotic pressure gradient is considered as driving force for this separation processes, Different with reverse osmosis, a "draw solution" with high concentration provide the osmosis pressure as driving force to induce water flow through the into draw solution side and rejecting mineral components simultaneously [13]. Without the external pressure to counteract the osmotic pressure gradient, energy requirement of forward osmosis is lower than reverse osmosis [14].

Another distinction between the forward osmosis and reverse osmosis processes is that the permeate water from RO process is fresh water can use directly. On the other hand FO process, the membrane separation process is an "exchange" between the feed solution and the draw solution. Therefore, depending on the concentration of draw solution and the

application of the product of the FO process, how to decide the species or concentration of draw solution is an important issue for forward osmosis process [12]. Generally, reverse osmosis has been mainly applied on sea water desolation process [15]. But water channel was selected as the material in this work, the tube-shape tunnel is considered as benefit for forward osmosis [16-18]. Therefore, the discussion of this work is focus on forward osmosis process and water channel. The introduction of water channel is illustrated in the next chapter.

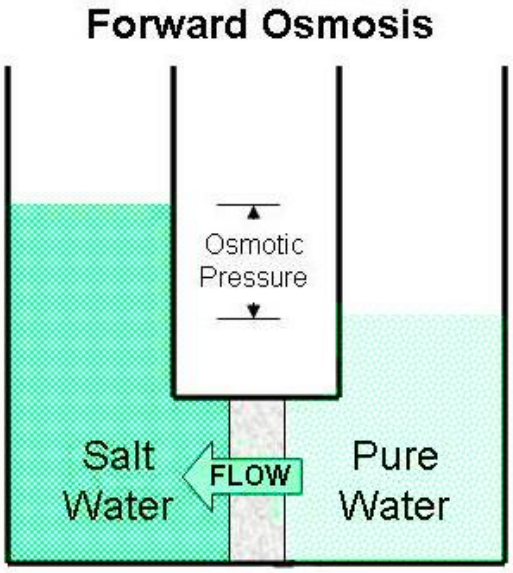

Fig1.4 Water flow direction for reverse forward process.

1.3 Water channel

The water transport mechanism and the promoting water conduction has been widely studied since 1957 [19]. Generally, water transports in and out the lipid component of cell membranes via osmosis. The relative high water permeability in some epithelial cells attracted researchers to study on the probable existence of additional mechanism or water pores. The herald study on water permeability through cell membrane was introduced by

Solomon et al. in late 1950s [20, 21]. Later, in 1960, the behavior of water molecules pass through a lipid phase membrane has been studied by a "partition–diffusion model" [22, 23]. Further, Parisi, Edelman, and Carvounis et al. emphasized that the possibility regulating on water permeability properties of water channel [24-26]. In 1990, Verkman et al. demonstrated functional behavior of water channel, also illustrated water channel is kind of proteins simultaneously [27, 28]. The briefly introduction of water channel are show as follow:

1.3.1 Natural water channel

Natural water channel also called aquaporin was introduced by Peter Agre until 1992 [29]. In 1999, Peter Agre and his co-works demonstrated the three-dimensional structure of aquaporin and named it as aquaporin-1 [30]. The behavior of water molecules transport through channel was introduced via simulation work too [31]. The 2003 Chemistry Nobel Prize was together awarded to Peter Agre and Roderick MacKinnon, for the discovering of aquaporin and for the work on mechanism and structure of potassium channels [32]. On the transport mechanism of aquaporin, water molecules transport through the channel in single file which was considered lead to high the water permeability performance [33]. On the other hand, the channel diameter of channel is around 8~10 Å which large enough for hydrate structure transport but the channel perfectly block ions including protons, essential to apply on desalination process or other industry application [34]. Although aquaporin has the above advantages, it limited by the costly and difficult to product because of the complex three-dimensional structure. Therefore, artificial water channel attracted the interest of researchers in recently day. The briefly introduction is showed as follow.

1.3.2 Artificial water channel

From the concept of natural aquaporin, artificial water channels have been constructed from water pervious pore and surrounding with a hydrophobic bilayer environment [35, 36]. These types of composite membranes function as a selective "water channel" to achieve a high level of water flux. The encouraging advantages shown in these successful pioneering studies have generated a great deal of interest in ways to design an artificial water channel. For example, Gramicidin A is one candidate of a novel protein channel that has a spiral structure as Aquaporin and also has excellent water permeability as well [37], but GA is toxic, it should be carefully handled for its practical application. In order to find simple, stable and safe artificial channel to instead of Aquaporin or GA embedded membranes, a biomimetic water channel is assumed to have a high potential as a novel membrane material. For the purpose to develop a next generation type high water flux membrane, it is indispensable to understand microscopic phenomena such as a relationship between water transport mechanisms and channel structures in molecular scale. This is an issue to be addressed for artificial water channel design, for which a computational scientific method can be useful and reasonably applied. In this study, we focused on developing suitable models for forming an artificial water channel.

1.4 Method of molecular simulation

From the 1980s, simulation technique through computer calculation grew up and has been adopted on physical and chemical atom scale analyses. The reasons show as followed: (1) the improvement of theoretical methods; (2) improvement of force-field describing; (3) high calculation performance computer; and (4) the more efficient calculation method. In general,

there might be some dangerous conditions and limitations during experimental work. For example, toxic chemicals or extreme high pressure not available in laboratory environment, and difficulty to analysis the properties at atom scale. Face above problems, the simulation methods can be an assistant to overcome these problems, which is able to provide some physical or chemical information at atom scale. The predictive properties through the theoretical method shows high potential to reduce the nature and human resource. In addition, the information at atom scale also provides good references for novel materials development [38, 39].

The modeling and theory methods can be categorized to four types by the system dimension and simulation time duration, as the follows: (1) in the description of electronic scale, the quantum mechanics is used to describe the system; (2) in the description of atomic scale, the system is described by statistical mechanics, to rapid achieve results for engineering applications, the semi-empirical functions also adopted to simulate the material characteristics; (3) in the meso-scale level, the dissipative particle dynamics (DPD) is used for the material property; and (4) continuum level, system follow the macroscopic laws, equation of continuity and momentum conservation are used to describe the properties description [40-44]. Figure 1.5 shows the simulation scales classification mentioned above.

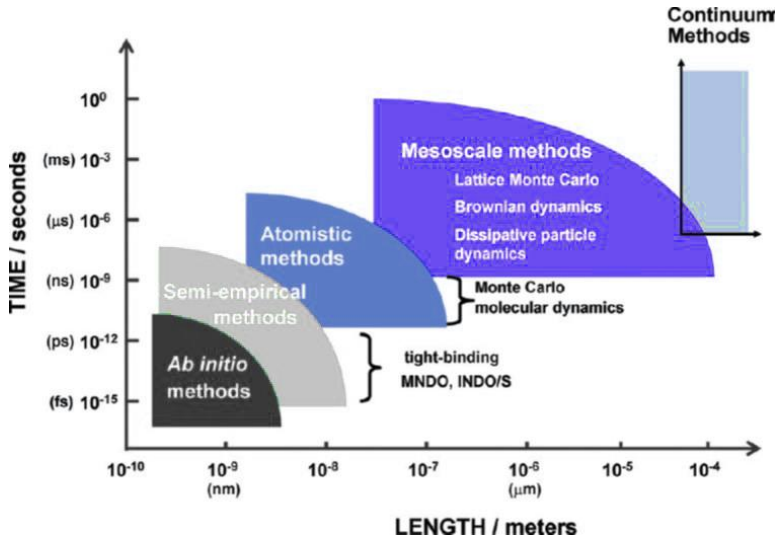

Fig1.5 Theory and simulation scales for ab initio (electronic), semi-empirical, atomistic, meso-scale, and continuum scales.

There are several methodologies in the field of molecular simulation. Such as, Quantum Mechanics, Molecular Mechanics, Molecular Dynamics simulation, and Monte Carlo method. Brief introduction are showed as below.

1.4.1 Quantum Mechanics

ab initio method

Before 1900s, the motion behaviors of particle at a micro-scale can be described through the Newton mechanics. Unfortunately, the Newton mechanics cannot well describe the interaction between the atom and electron. Therefore, quantum mechanics was adopted to get the properties of materials at electronic scale. Besides, the ab initio method is the most stringent method to simulate the electronic structure of material without experimental information. This method satisfied to describe chemical reaction with bond breaking or forming. Regrettably, the ab initio calculations method need high computer ability. With the

limitation of computer resource, the smaller system scale and shorter calculation time are considered during calculation period.

1.4.2 Density Functional Theory (DFT)

In 1964, Hohenberg et al. [45] introduced the DFT theory. The concept of DFT is to explain the interacting between electrons by their density. In simple words, the ground state property of system could be described by their electronic density. DFT could calculate the object property without the movement of electron and is suitable in the huge system. To effectively use DFT, finding an appropriate approximation function of energy on the electron density is necessary.

Mostly, obtaining the objective properties of electronic structures by using the quantum mechanics calculation required more computational resource. As described above, ab initio method is limited by the computer calculation ability. Thus, to decrease the calculation time and keep the accuracy, the semi-empirical approaches method to simplify the calculation program was developed to explain the matter characteristics.

1.4.3 Molecular Mechanics

The molecular mechanics was derived from the foundation of classical mechanics theorem for describing the molecular features and physical characteristics. However, the molecular mechanics could not describe the kinetic energy and dynamic behaviors. Comparing with quantum mechanics, the electronic effect was ignored in molecular mechanics due to the obvious mass difference between electron and atom core, further reduce the calculation resource. Although the results from molecular mechanics show great performance, this approximately estimation still presents certain mismatch in comparison to the results from

quantum mechanics. Thus, the potential function parameters were adopted into the molecular mechanics, the parameters derived from the semi-empirical function were used to eliminate the mismatch and achieve more reasonable results.

1.4.4 Molecular Dynamics (MD)

The molecular structure constructed by molecular model and reveals the static structure property. However, to explain the materials characteristics, some factors like pressure and temperature are essential to be included to suit the realistic state. Therefore, the MD simulation could involve the system free energy, temperature, and pressure, is more feasible to illustrate the material properties. The molecular dynamics simulation use Newton mechanics in the simulation model, randomly setting the velocity or acceleration of atoms to simulate the system structure, and the equilibrated and stable molecular structure could be received. The process of MD simulation were briefly described in Figure 1.6. Details of the MD simulation procedure and arithmetic adopted in this work are illustrated in chapter 1.5.

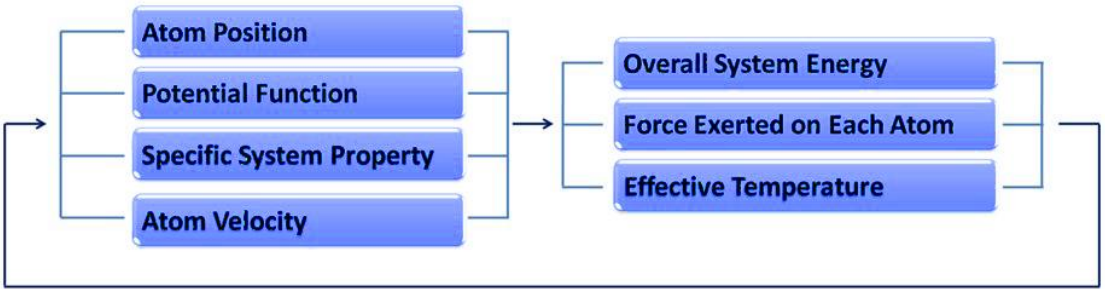

Fig1.6 The essential steps of molecule dynamics simulation.

1.4.5 Monte Carlo (MC) method

The MD and MC theorem are the main statistical mechanics in molecular simulation calculations, which first developed in the late 1940s and 1950s in America [38]. The basic

method of MC theorem showed as follows: The arrangement of atoms/molecules of system corresponds to a specific possibility, which can also provide the potential energy of system by selecting potential functions. Therefore, the system potential energy could be calculated from the atom coordinates decided by the randomly sample. Through this method to calculate the system structures and potential energies, and then the structure with the minimized energy can be obtained.

1.5 Theoretical method

The mirco-structure and water molecules transport behaviors of two type of artificial water channel by using the MD simulation technique were introduced in this study. In this chapter, list the calculation theory, simulation model construction, potential energy selection, and physical property analysis, as show in following.

1.5.1 Artificial water channel and forward osmosis molecular model

Two different materials, cyclic peptide nanotube and amphotericin b, were adopted to construct artificial water channel molecular model by using simulation techniques, as Fig 1.7 and Fig 1.8 shows. In this thesis, four different types of cyclic peptide nanotube and two different types of amphotericin b channel would be constructed. For more discussion, each types of channel would be assigned in forward osmosis process model as shown in Fig 1.9. All the analyses and discussion would be introduced in following chapter, the detail of molecular would describe in each chapter.

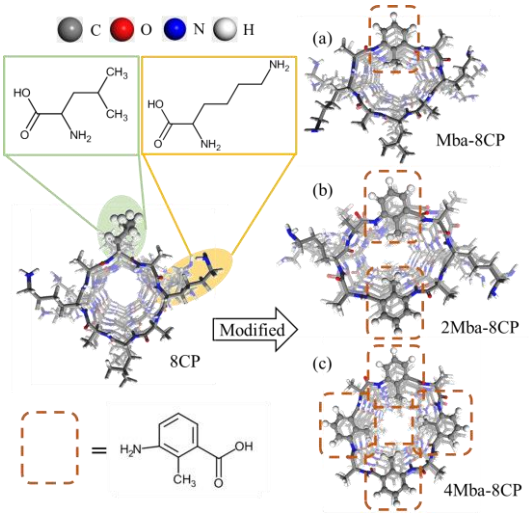

Fig1.7 Four different types of cyclic peptide nanotube.

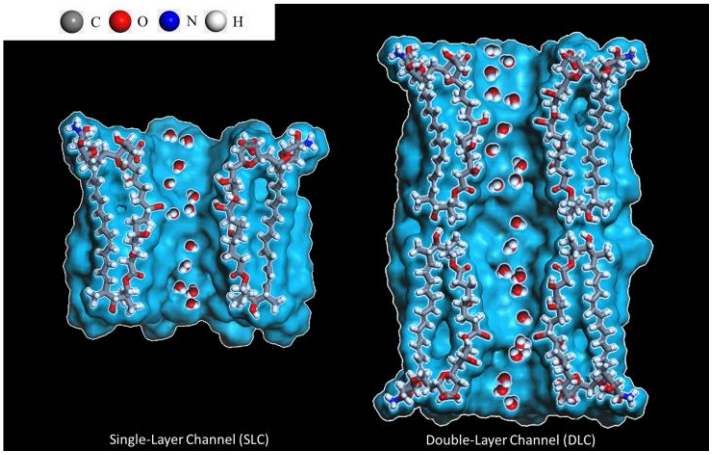

Fig1.8 Two different types of amphotericin b channel.

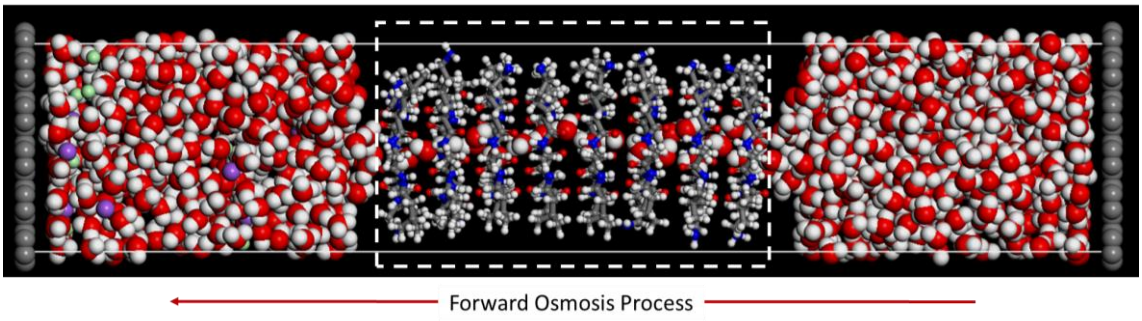

Fig1.9 Forward osmosis simulation model.

1.5.2 COMPASS force field

In this study, the Condensed-phase Optimized Molecular Potential for Atomistic Simulation Studies (COMPASS) force field [46-48] ccwas adopted to perform the energy minimization and MD calculation processes. The various functional forms in this force field are illustrated as follows:

$$
\begin{aligned}
E = & \sum_{b}\left[K_2(b-b_0)^2 + K_3(b-b_0)^3 + K_4(b-b_0)^4\right] \\
& \textbf{(a)} \\
& + \sum_{\theta}\left[H_2(\theta-\theta_0)^2 + H_3(\theta-\theta_0)^3 + H_4(\theta-\theta_0)^4\right] \\
& \textbf{(b)} \\
& + \sum_{\phi}\left\{V_1\left[1-\cos\left(\phi-\phi_1^0\right)\right] + V_2\left[1-\cos\left(2\phi-\phi_2^0\right)\right] + V_3\left[1-\cos\left(3\phi-\phi_3^0\right)\right]\right\} \\
& \textbf{(c)} \\
& + \sum_{x} K_x x^2 + \sum_{b}\sum_{b'} F_{bb'}(b-b_0)(b'-b'_0) + \sum_{\theta}\sum_{\theta'} F_{\theta\theta'}(\theta-\theta_0)(\theta'-\theta'_0) \\
& \textbf{(d)} \qquad\qquad \textbf{(e)} \qquad\qquad \textbf{(f)} \\
& + \sum_{b}\sum_{\theta} F_{b\theta}(b-b_0)(\theta-\theta_0) + \sum_{b}\sum_{\phi}(b-b_0)\left[V_1\cos\phi + V_2\cos 2\phi + V_3\cos 3\phi\right] \\
& \textbf{(g)} \qquad\qquad\qquad\qquad \textbf{(h)} \\
& + \sum_{b'}\sum_{\phi}(b'-b'_0)\left[V_1\cos\phi + V_2\cos 2\phi + V_3\cos 3\phi\right] \\
& \textbf{(i)} \\
& + \sum_{\phi}\sum_{\theta}\sum_{\theta'} K_{\phi\theta\theta'}\cos\phi(\theta-\theta_0)(\theta'-\theta'_0) + \sum_{i>j}\frac{q_i q_j}{\varepsilon r_{ij}} + \sum_{i>j}\left[\frac{A_{ij}}{r_{ij}^9} - \frac{B_{ij}}{r_{ij}^6}\right] \\
& \textbf{(j)} \qquad\qquad \textbf{(k)} \qquad \textbf{(l)}
\end{aligned}
\tag{1}
$$

The energy terms are composed of three categories: bonded energy terms, cross-interaction terms, and non-bonded energy terms. The bonded energy terms include (a) the covalent bond-stretching energy terms, (b) the bond-angle bending energy terms, and (c) the torsion-angle rotation energy terms. The designation (d) is either the out-of-plane energy, or an improper term. The terms for cross-interaction consist of the dynamic variations among bond stretching, bending, and torsion angle rotation interactions ((e)–(j)). The non-bonded energy terms, (k) and (l), represent the Coulombic electrostatic interaction force and the van der Waals (vdW) potential force, respectively.

1.5.3 Geometrical structure optimization and periodical boundary condition

1.5.3.1 Geometrical structure optimization

The reasonable initial simulation structure is very important in calculation period, therefore, the molecular model should find the structure with minimum energy by the energy minimization process. However, the structure with "global minimum energy" is difficult to achieve by the finite iteration. Instead, the structure with "local minimum energy" was collected as the initial structure for following work. The general method for geometrical structure optimization calculation show as follows:

(1) Steepest descents algorithm

In the process of steepest descents method, the revised direction during the minimization calculation is defined along the path of local downgrade gradient $-\nabla E(\vec{R})$, as shown in Figure 1.10. Although the steepest descents method could supply rapid structure relaxation, it would consistently cross over the best route to the minimum, which causes an ineffective oscillating trajectory.

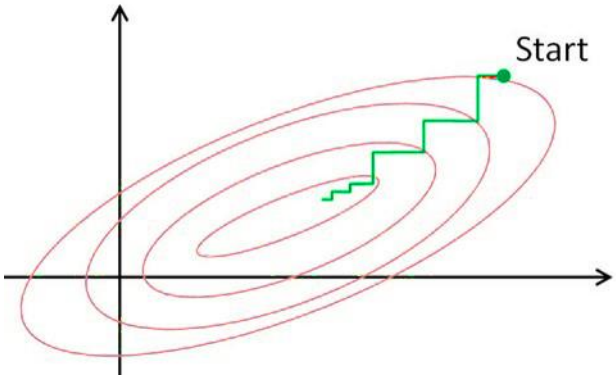

Fig1.10 Schematic of Steepest descents method during the energy minimization process.

(2) Conjugate gradient algorithm

Different with steepest descents method, two directions were adopted in the conjugate gradient method, the present and former modified direction, for the next modification. This added direction can avoid the next direction vector from destructive progress. Through reduce the needless oscillating trajectory, minimization process could rapidly and correctly to find the energy minimum structure.

(3) Newton-Raphson algorithm

A curvature of function is adopted in Newton-Raphson algorithm for predicting where the function passes across a minimum along that path. Because the complete curvature of function matrix assign the curvature in each gradient direction, the inverse of the curvature of function matrix could be multiplied by the gradient to obtain a vector which translates straightly to the nearest minimum.

(4) SMART algorithm

The “SMART” algorithm in the commercial BIOVIA Materials Studio® software include all the above methods. In simple word, through this function could automatically select the suitable method for each occasion. Although “SMART” algorithm might spend more time for calculation, it could obtain more stable molecular structure. From this, SMART algorithm was adopted for geometrical structure optimization process in this work.

1.5.3.2 Periodical boundary condition

Generally, there are around thousands atom within the simulation model during the calculation process. In the small system, it might cause some mismatch or unreasonable results because of the wall effect problem. In order to overcome the problem, the assumption of infinite boundary was adopted within the molecular model. In this work, the periodical boundary conditions (PBC) assumption was used to remove the wall effect problem and to achieve the infinite boundary.

The three dimensional PBC system showed as Figure 1.11. In Figure 1.11, showed one primary cell (brighter region) and several virtual cells (grayer region) in PBC system. Within primary cell, when molecule A (purple) or B (green) pass out to the neighboring virtual cells, the same part of corresponding molecules will come into the main cell, to remain the mass balance. Therefore, this PBC concept could achieve the infinite boundary and eliminate the wall effect simultaneously. In addition, to eliminate the non-bonding interaction of matter in the main cell and virtual cell, the cut-off distance is set during the calculation period.

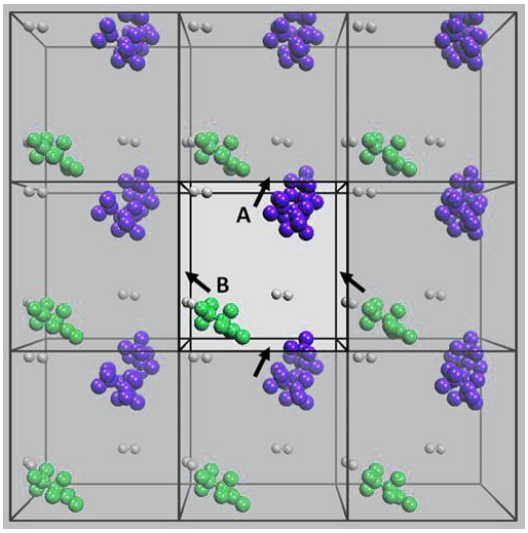

Fig1.11 The PBC is composed of one primary cell (brighter region) and several virtual cells (grayer region).

1.5.4 Molecular Dynamics simulation

The dynamic molecular structure based on local minimum could be determined by the kinetic energy system and internal energy. Currently, most simulated works are performed under a constant temperature. Valid adjusting the temperature of system to maintain the stable structure is important to accomplish a dynamic calculation work. During MD period, the atom velocity is usually used to fit the instantaneous system temperature. Therefore, on microscope view, the simulation in this work could be classified as the non-equilibrium static thermodynamics. In this work, how to decide system temperature and atom velocity is explained as follows.

1.5.4.1 Initial Velocity and temperature of system

(1) Initial velocity determination

The atom initial velocity could be randomly appointed by using the Maxwell– Boltzmann distribution function at specific temperature, Maxwell– Boltzmann functions show as follows:

$$f(v)dv = \left(\frac{m}{2\pi kt}\right)^{3/2} e^{\left(\frac{-mv^2}{2kt}\right)} 4\pi v^2 dv, \qquad (2)$$

Where the meaning is probability *f(v)*, *m*: atom/molecule mass, *v*: velocity, and *T*: temperature. And the velocities at *x*, *y*, *z* components have Gaussian distributions:

$$g(v_x)dv_x = \left(\frac{m}{2\pi kT}\right)^{1/2} e^{\left(\frac{-mv_x^2}{2kT}\right)} dv_x, \qquad (3)$$

The atom/molecule initial velocity could be derived from the Gaussian distribution of v_x, v_y, and v_z ($v^2 = v_x^2 + v_y^2 + v_z^2$).

(2) Temperature determination

In MD calculation, velocity scaling method is considered as a common means to define the temperature from moving atom/molecules. Among the MD simulation period, every atom hold instantaneous velocity. The spontaneous temperature of system could be obtained by the following equation:

$$\langle K \rangle = \frac{N_f K_B T_{ins}}{2}, \quad (4)$$

Where the meaning is that $\langle K \rangle$: the system average kinetic energy, K_B: the Boltzmann constant, T_{ins}: system instantaneous temperature, and N_f: degree of freedom. In this work, N_f is equal to 3N because all of the atom within the space retain three components, v_x, v_y, and v_z. Therefore, the instantaneous temperature could be derived follows:

$$T_{ins} = \frac{2\langle K \rangle}{3NK_B}, \quad (5)$$

The objective temperature could be controlled by ratio of velocity values, as show in following relationship:

$$\left(\frac{v_{new}}{v_{old}} \right)^2 = \frac{T_{tar}}{T_{ins}}, \quad (6)$$

In this process, the speed depends on the energy, parameters, and the vibrational, rotational, translational of molecule. Also, the larger systems take longer time to equilibrate. The temperature-bath coupling Berendsen method was using during the MD calculation process in this work. A smooth thermal energy exchange between the system and heat bath at equilibrium state could be introduced by using velocity scaling method. Through Berendsen method, the velocity re-scale by a factor λ:

$$\lambda = \left[1 - \frac{\Delta t}{\tau} \left(\frac{T_{ins} - T_{tar}}{T_{ins}} \right) \right]^{1/2}, \quad (7)$$

Where the meaning is Δt: time step dimension, τ: relaxation time. Through modifying the relaxation time τ to adjust the temperature, the system could remain as a constant-temperature ensemble. Thus, it is widely used to obtain equilibrium state and achieve target temperature simultaneously.

1.5.4.2 NVT Ensembles

Within the MD processes, most simulation system should match the nature phenomena such as external pressure and heat exchanges with the environment. Under these conditions, the total energy of the system is no longer conserved and extended forms of molecular dynamics are required. There are several methods to control temperature and pressure. The variables of simulation system including energy (E), enthalpy (H), number of atoms (N), pressure (P), volume (V), and temperature (T) could be fixed depended on the calculation necessary. Table 1.1 summarizes the ensembles in BIOVIA Materials Studio®. Among them, the NVT ensemble is adopted in this work.

Table 1.1 Calculation ensembles handled by BIOVIA Materials Studio®.

Ensembles*	Fixed variables		
NPT**	Atom number	System pressure	System temperature
NVE	Atom number	System volume	System enthalpy
NPH**	Atom number	System pressure	System energy
NVT	Atom number	System volume	System temperature

*In all ensembles, the number of atoms is conserved.
**Only for periodic systems, because volume is undefined in non-periodic systems.

NVT ensemble, the constant-atom number, constant-volume, and constant-temperature ensemble, also is called as canonical ensemble, is obtained through control the thermodynamic temperature. The temperature of system is oscillation around the target temperature, it is not a truly isothermal system

1.5.4.3 Dynamics simulation Algorithm

In the MD calculation, the movements of atoms/molecules could be described by the Newton's equation, as show the following:

$$F_i = m_i \frac{\partial^2 r_i}{\partial t^2} = -\frac{\partial U}{\partial r_i} \quad (i = 1, 2, ...n), \tag{8}$$

Where the meaning is *F*: force, *r*: coordinate including x, y, and z components, and *U*: system potential. By integrating the equation could obtain the positions of atom/molecule, force, velocity, etc. within the system. Also, the function *r(t)* which represents atom positions can be obtained. Verlet algorithm and Leapfrog algorithm which are two common numerical methods using in MD process. The briefly description as show in Fig 1.12.

(1) Verlet algorithm

Verlet algorithm method used the displacement function, $\mathrm{r}(\mathrm{t}-\Delta\mathrm{t})$ and the displacement function *r(t)* and acceleration *a(t)* at current time step to calculate the displacement function at following time step, $\mathrm{r}(\mathrm{t}+\Delta\mathrm{t})$. The two displacement functions, $\mathrm{r}(\mathrm{t}+\Delta\mathrm{t})$ and $\mathrm{r}(\mathrm{t}-\Delta\mathrm{t})$ could be expressed by using the Taylor series:

$$r(t+\Delta t) = r(t) + V(t)\Delta t + \frac{1}{2}a(t)\Delta t^2 + \cdots, \quad (9)$$

$$r(t-\Delta t) = r(t) - V(t)\Delta t + \frac{1}{2}a(t)\Delta t^2 + \cdots, \quad (10)$$

Through rearranging the equation, the displacement function, could be described as:

$$r(t+\Delta t) = 2r(t) - r(t-\Delta t) + a(t)\Delta t^2, \quad (11)$$

At the same time, the velocity and kinetic energy of atom could be calculated from the next equation:

$$V(t) = \frac{r(t+\Delta t) - r(t-\Delta t)}{2\Delta t}, \quad (12)$$

(2) Leapfrog algorithm

Leapfrog algorithm method is obtained by revising the Verlet algorithm method. Through placing the atom velocity at the halt time step to calculate the velocity of atom at current time step. The velocities at the halt time steps could be expressed as:

$$V(t-\frac{1}{2}\Delta t) = \frac{r(t) - r(t-\Delta t)}{\Delta t}, \quad (13)$$

$$V(t+\frac{1}{2}\Delta t) = \frac{r(t+\Delta t) - r(t)}{\Delta t}, \quad (14)$$

And *a(t)* could be expressed as:

$$a(t) = \frac{r(t+\Delta t) - 2r(t) + r(t-\Delta t)}{\Delta t^2}, \tag{15}$$

Deriving *a(t)* into Eq. (15) to obtain the following Equation:

$$V(t+\frac{1}{2}\Delta t) - V(t-\frac{1}{2}\Delta t) = \frac{r(t+\Delta t) + r(t-\Delta t) - 2r(t)}{\Delta t} = \Delta t \cdot a(t), \tag{16}$$

$$V(t+\frac{1}{2}\ \Delta t) = V(t-\frac{1}{2}\ \Delta t) + \ \Delta t \cdot a(t), \tag{17}$$

And, $\mathrm{r}(\mathrm{t}+\Delta\mathrm{t})$, and $\mathrm{r}(\mathrm{t}-\Delta\mathrm{t})$ could be obtained as following:

$$r(t+\Delta t) = r(t) + V(t+\frac{1}{2}\Delta t)\Delta t, \tag{18}$$

$$r(t-\Delta t) = r(t) - V(t-\frac{1}{2}\Delta t)\Delta t, \tag{19}$$

Finally, the velocity of atom under current time step could be obtained by using the result as following:

$$V(t) = \frac{1}{2}[V(t+\frac{1}{2}\Delta t) + V(t-\frac{1}{2}\Delta t)], \tag{20}$$

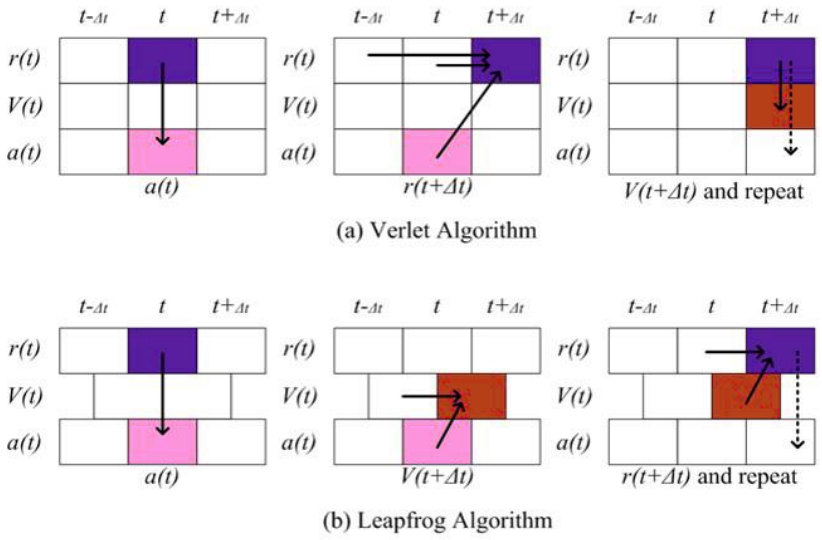

Fig1.12 Schematic presentation of (a) Verlet algorithm, and (b) Leapfrog algorithm.

1.5.5 Physical Property Analyses

1.5.5.1 Structural characteristics

To describe channel morphology of the cyclic peptide nanotubes and amphotericin b channels, the inner diameter were considered. In the case of cyclic peptide nanotube, the inner diameter of each cyclic peptide subunit was estimated to compare the channel morphology between the simulation models. In the case of amphotericin b channel, the narrowest distance was estimate as channel diameter. The internal diameter were estimated based on the van der Walls radii of the simulation models obtained using the Visualizer Module in BIOVIA Materials Studio® commercial software.

1.5.5.2 Hydrogen bond number analysis

The affinity between water molecules and nanotubes/channel is an important factor to affect water mobility. Thus, the distribution of hydrogen bonds was analyzed to explore the inner affinity of the nanotube/channel simulation models. The distribution of the hydrogen bonds between water molecules and nanotubes was obtained using the Visualizer Module in BIOVIA Materials Studio® commercial software.

1.5.5.3 Sorption isotherm of water molecules

The process of water molecule sorption in nanotubes/channel can be described using the Grand Canonical Monte Carlo (GCMC) method. During the simulation, the relative probabilities of the different states of a system were simulated using the Metropolis algorithm. There are four types of configurations for adsorbed water molecules: conformer, rotation, translation, and regrowth. The detail theory of sorption calculation was shown in supplementary information. The sorption analysis calculation in this work was processed one million times. The number of water molecules that were adsorbed by the inner nanotube/channel was recorded and the sorption loading was evaluated as a function of the water vapor pressure.

1.5.5.4 Mean-squared displacement (MSD) and self-diffusivity

The mean-squared displacement (MSD) of water molecules within nanotube/channel was calculated using NVT MD simulation to analyze the differences in the diffusion behaviors of

water molecules for each of the molecular models. The diffusion coefficient of water molecule could be easily obtained using the Einstein relationship:

$$MSD(t) = \frac{1}{N}\sum_{i=1}^{N}\{[r_i(t_0 + t) - r_i(t_0)]^2\} = B + 6D \times \mathrm{t} \quad (21)$$

where N is the total number of atoms, r_i (t_0+t) and r_i (t_0) are the positions at time t_0+t and time t_0, respectively, B is a constant, and D is the diffusion coefficient. The diffusion coefficient can be calculated from the slope of the MSD curve.

1.5.5.5 Water molecule permeability

In this work, the water molecule permeability performance was predicted by two different methods, solution-diffusion model and forward osmosis method.

Solution-diffusion model

The overall permeability was based on the solubility and diffusivity by the solution-diffusion model [49]. Water molecule permeation through nanotube/channel is an indicator to reflect membrane performance, and is dominated by the diffusion and sorption behavior of water molecule. To describe the water molecule permeation through nanotube/channel, the "solution-diffusion" mechanism is generally used in theoretical work. Through the production of diffusion and solution calculation, the permeability of water molecule could be calculated. In this study, the sorption behavior of water molecule in nanotube/channel was examined under 298 K.

Forward osmosis permeability

During the calculation period, the number of water molecules within nanotubes in both pure water, and salt water reservoirs were traced and recorded. According to these data, we can obtain time course curve of water molecules in three different divisions of simulation model, respectively as a function of elapsed time through NVT MD simulations. The curves of the number of water molecules were analysed to study the differences in the permeation behaviors of water molecules for each of the nanotube/channel models. Osmotic pressure was considered as the driving force during FO simulation period which can be calculated from Van't Hoff equation. The predictive water permeability can be calculated from the slope of the water molecules alteration curve by Eq. (22),

$$Permeability\ [mol\ m/(m^2 s\ Pa)] = \frac{\Delta N\ L}{A\ \Delta t\ \Delta \pi N_A} \quad (22)$$

where, ΔN [-] is the change of the number of molecules during a certain period Δt [s], A [m^2] the area of cross section of nanotube/channel, $\Delta \pi$ mean osmotic pressure during Δt, N_A [mol^{-1}] Avogadro's number, and L [m] channel length. In this work, a long time calculation period was provided to obtain diagrams for the time course of the number of water molecules.

1.6 Purpose of this study

Membrane separation process has been considered as one of the promising methods for water treatment. With, the global water scarcity and pollution became a serious problem around the world. The efficient membrane separation process or high performance separation membrane is necessary. In this work, I focused on the biomimetic membrane application on

forward osmosis process for desalination. Among biomimetic materials, artificial water channel was considered as one of candidate to replace the high performance but expensive natural water channel (Aquarian). However, to design a stable and safe artificial water channel is still a tough work in recent day. Therefore, to deeply understand the characteristic of materials, simulation technique was carried out as an assistant for material design. The information such as energy distribution, transport mechanism…etc. at atom scale could be the useful message for designing an artificial water channel using biomimetic materials. Two types of materials were selected as the candidate of artificial water channel in this work. The structural properties, water transport mechanism, and application on forward osmosis process was studied through simulation technique under atom scale. Aiming to find a high performance biomimetic material for application in desalination process.

1.7 Extent of this study

There are 6 parts in this thesis. The briefly describing of each part is shown as below:

In chapter 1 presented the background, introduction, and the purpose of this study.

In chapter 2, molecular dynamics technique was used to construct four different molecular models of nanotubes: an octamer prototypical cyclic peptide (8CP); and, three cyclic peptides modified by replacing one or two L-Lysine or L-Leucine groups with an aromatic amino acid, 3-amino-2-methylbenzoic acid (γ-Mba-OH). The results was showed and compared to understand how the hydrophobic modification functional group effect on the structural properties and transport mechanism of cyclic peptide nanotube.

In chapter 3, water molecules transport performance and ion rejection ability of cyclic peptide nanotubes were explored via simulation of forward osmosis (FO) filtration phenomena under molecular level. FO filtration model and three different types of cyclic peptide nanotube (with different level of modification by hydrophobic functional group) were constructed by using molecular dynamics technique. Molecular dynamics simulation was adopted to explicate the diversity transport mechanism between different types of CPNTs, that is, how the hydrophobic modified functional group affects FO filtration process.

In chapter 4, molecular simulation was used to explore the structural characteristics and water transport performance of Amphotericin B-Brgosterol (AmBEr) channels. A molecular dynamics technique was used to construct two types of molecular models of AmBEr channels: single-layer channel (SLC) and double-layer channel (DLC). A molecular dynamic simulation was used to illustrate the differences between SLC and DLC AmBEr models with respect to structure, channel diameter, interior affinity, and transportation behavior of water molecules. A Monte Carlo (MC) method was adopted to investigate the sorption behavior in these two types of AmBEr channels. The intramolecular properties and intermolecular interactions indicated the feasibility of the simple model construction method adopted in this study.

In chapter 5, water molecules transport property Amphotericin B-Ergosterol (AmBEr) channel via simulation of forward osmosis (FO) filtration phenomena were explored under molecular level. FO filtration model and double-layer channel (DLC) AmBEr channel model were constructed by using molecular dynamics technique. Molecular dynamics simulation

was adopted to explicate the diversity transport mechanism of novel AmBEr channel, meanwhile, the performance comparison with commercial membrane was introduced too.

In chapter 6, introduced the conclusion of this thesis.

References

[1] E. Staude, Marcel Mulder: Basic Principles of Membrane Technology, Kluwer Academic Publishers, Dordrecht, Boston, London, 1991, ISBN 0‐7923‐0978‐2, 363 Seiten, Preis: DM 200,—, Berichte der Bunsengesellschaft für physikalische Chemie, 96 (1992) 741-742.
[2] B. Nicolaisen, Developments in membrane technology for water treatment, Desalination, 153 (2003) 355-360.
[3] P. Van de Witte, P.J. Dijkstra, J. Van den Berg, J. Feijen, Phase separation processes in polymer solutions in relation to membrane formation, Journal of membrane science, 117 (1996) 1-31.
[4] C. Fritzmann, J. Löwenberg, T. Wintgens, T. Melin, State-of-the-art of reverse osmosis desalination, Desalination, 216 (2007) 1-76.
[5] K. Wangnick, International Desalination Association IDA, Worldwide Desalting Plants Inventory Report, (2004).
[6] K. Wangnick, International Desalination Association worldwide desalting plants inventory report no. 18, Produced by Wangnick Consulting for International Desalination Association, Topsfield, MA, (2004).
[7] J. Glater, The early history of reverse osmosis membrane development, Desalination, 117 (1998) 297-309.
[8] C.H. Ahn, Y. Baek, C. Lee, S.O. Kim, S. Kim, S. Lee, S.-H. Kim, S.S. Bae, J. Park, J. Yoon, Carbon nanotube-based membranes: Fabrication and application to desalination, Journal of Industrial and Engineering Chemistry, 18 (2012) 1551-1559.
[9] K.P. Lee, T.C. Arnot, D. Mattia, A review of reverse osmosis membrane materials for desalination—development to date and future potential, Journal of Membrane Science, 370 (2011) 1-22.
[10] S. Lee, R.M. Lueptow, Reverse osmosis filtration for space mission wastewater: membrane properties and operating conditions, Journal of Membrane Science, 182 (2001) 77-90.
[11] Y.-y. Lu, Y.-d. Hu, D.-m. Xu, L.-y. Wu, Optimum design of reverse osmosis seawater desalination system considering membrane cleaning and replacing, Journal of membrane science, 282 (2006) 7-13.

[12] T.Y. Cath, A.E. Childress, M. Elimelech, Forward osmosis: principles, applications, and recent developments, Journal of membrane science, 281 (2006) 70-87.
[13] S. Phuntsho, H.K. Shon, S. Hong, S. Lee, S. Vigneswaran, A novel low energy fertilizer driven forward osmosis desalination for direct fertigation: evaluating the performance of fertilizer draw solutions, Journal of Membrane Science, 375 (2011) 172-181.
[14] M. Elimelech, W.A. Phillip, The future of seawater desalination: energy, technology, and the environment, science, 333 (2011) 712-717.
[15] B. Peñate, L. García-Rodríguez, Current trends and future prospects in the design of seawater reverse osmosis desalination technology, Desalination, 284 (2012) 1-8.
[16] W. Ding, J. Cai, Z. Yu, Q. Wang, Z. Xu, Z. Wang, C. Gao, Fabrication of an aquaporin-based forward osmosis membrane through covalent bonding of a lipid bilayer to a microporous support, Journal of Materials Chemistry A, 3 (2015) 20118-20126.
[17] H.T. Madsen, N. Bajraktari, C. Hélix-Nielsen, B. Van der Bruggen, E.G. Søgaard, Use of biomimetic forward osmosis membrane for trace organics removal, Journal of Membrane Science, 476 (2015) 469-474.
[18] S. Wang, J. Cai, W. Ding, Z. Xu, Z. Wang, Bio-inspired aquaporinz containing double-skinned forward osmosis membrane synthesized through layer-by-layer assembly, Membranes, 5 (2015) 369-384.
[19] M. Parisi, R.A. Dorr, M. Ozu, R. Toriano, From membrane pores to aquaporins: 50 years measuring water fluxes, Journal of biological physics, 33 (2007) 331.
[20] D.A. Goldstein, A. Solomon, Determination of equivalent pore radius for human red cells by osmotic pressure measurement, The Journal of general physiology, 44 (1960) 1-18.
[21] C.V. Paganelli, A. Solomon, The rate of exchange of tritiated water across the human red cell membrane, The Journal of general physiology, 41 (1957) 259-277.
[22] J. Dainty, C. House, An examination of the evidence for membrane pores in frog skin, The Journal of physiology, 185 (1966) 172-184.
[23] T. Hanai, D. Haydon, The permeability to water of bimolecular lipid membranes, Journal of theoretical biology, 11 (1966) 370-382.
[24] C.P. Carvounis, S.D. Levine, R.M. Hays, pH-Dependence of water and solute transport in toad urinary bladder, Kidney international, 15 (1979) 513-519.
[25] P.F. Gulyassy, I.S. Edelman, Hydrogen-ion dependence of the antidiuretic action of vasopressin, oxytocin and deaminooxytocin, Biochimica et Biophysica Acta (BBA)-Biophysics including Photosynthesis, 102 (1965) 185-197.
[26] M. Parisi, J. Bourguet, Effects of cellular acidification on ADH-induced intramembrane particle aggregates, American Journal of Physiology-Cell Physiology, 246 (1984) C157-C159.
[27] R. Zhang, S. Alper, B. Thorens, A. Verkman, Evidence from oocyte expression that the erythrocyte water channel is distinct from band 3 and the glucose transporter, Journal of Clinical Investigation, 88 (1991) 1553.
[28] R. Zhang, K. Logee, A. Verkman, Expression of mRNA coding for kidney and red cell water channels in Xenopus oocytes, Journal of Biological Chemistry, 265 (1990) 15375-15378.

[29] P. Agre, G.M. Preston, B.L. Smith, J.S. Jung, S. Raina, C. Moon, W.B. Guggino, S. Nielsen, Aquaporin CHIP: the archetypal molecular water channel, American Journal of Physiology-Renal Physiology, 265 (1993) F463-F476.
[30] K. Mitsuoka, K. Murata, T. Walz, T. Hirai, P. Agre, J.B. Heymann, A. Engel, Y. Fujiyoshi, The structure of aquaporin-1 at 4.5-Å resolution reveals short α-helices in the center of the monomer, Journal of structural biology, 128 (1999) 34-43.
[31] B.L. de Groot, H. Grubmüller, The dynamics and energetics of water permeation and proton exclusion in aquaporins, Current opinion in structural biology, 15 (2005) 176-183.
[32] M.A. Knepper, S. Nielsen, Peter agre, 2003 Nobel Prize winner in chemistry, Journal of the American Society of Nephrology, 15 (2004) 1093-1095.
[33] E. Kruse, N. Uehlein, R. Kaldenhoff, The aquaporins, Genome biology, 7 (2006) 206.
[34] T. Gonen, T. Walz, The structure of aquaporins, Quarterly reviews of biophysics, 39 (2006) 361-396.
[35] M. Barboiu, Artificial water channels, Angewandte Chemie International Edition, 51 (2012) 11674-11676.
[36] Y. Le Duc, M. Michau, A. Gilles, V. Gence, Y.M. Legrand, A. van der Lee, S. Tingry, M. Barboiu, Imidazole‐Quartet Water and Proton Dipolar Channels, Angewandte Chemie International Edition, 50 (2011) 11366-11372.
[37] P.A. Rosenberg, A. Finkelstein, Water permeability of gramicidin A-treated lipid bilayer membranes, The Journal of general physiology, 72 (1978) 341-350.
[38] K.E. Gubbins, J.D. Moore, Molecular modeling of matter: Impact and prospects in engineering, Industrial & Engineering Chemistry Research, (2010).
[39] E. Maginn, J. Elliott, Historical perspective and current outlook for molecular dynamics as a chemical engineering tool, Industrial & Engineering Chemistry Research, 49 (2010) 3059-3078.
[40] A. Dwivedi, A.N. Cormack, A computer simulation study of the defect structure of calcia-stabilized zirconia, Philosophical Magazine A, 61 (1990) 1-22.
[41] G. Lewis, C. Catlow, Potential models for ionic oxides, Journal of Physics C: Solid State Physics, 18 (1985) 1149.
[42] H.-C. Wu, T. Yoshioka, H. Nagasawa, M. Kanezashi, T. Tsuru, D. Saeki, H. Matsuyama, Preparation of cyclic peptide nanotube structures and molecular simulation of water adsorption and diffusion, Journal of Membrane Science, 537 (2017) 101-110.
[43] H.-C. Wu, T. Yoshioka, K. Nakagawa, T. Shintani, T. Tsuru, D. Saeki, Y.-R. Chen, K.-L. Tung, H. Matsuyama, Water transport and ion rejection investigation for application of cyclic peptide nanotubes to forward osmosis process: A simulation study, Desalination, 424 (2017) 85-94.
[44] H.-C. Wu, T. Yoshioka, K. Nakagawa, T. Shintani, T. Tsuru, D. Saeki, A.R. Shaikh, H. Matsuyama, Preparation of Amphotericin B-Ergosterol structures and molecular simulation of water adsorption and diffusion, Journal of Membrane Science, 545 (2018) 229-239.
[45] P. Hohenberg, W. Kohn, Inhomogeneous electron gas, Physical review, 136 (1964) B864.

[46] D. Rigby, H. Sun, B. Eichinger, Computer simulations of poly (ethylene oxide): force field, pvt diagram and cyclization behaviour, Polymer International, 44 (1997) 311-330.
[47] H. Sun, COMPASS: an ab initio force-field optimized for condensed-phase applications overview with details on alkane and benzene compounds, The Journal of Physical Chemistry B, 102 (1998) 7338-7364.
[48] H. Sun, P. Ren, J. Fried, The COMPASS force field: parameterization and validation for phosphazenes, Computational and Theoretical Polymer Science, 8 (1998) 229-246.
[49] J.G. Wijmans, R.W. Baker, The solution-diffusion model: a review, Journal of membrane science, 107 (1995) 1-21.

Chapter 2

Preparation of cyclic peptide nanotube structures and molecular simulation of water adsorption and diffusion

2.1 Introduction

Global water scarcity and pollution became a serious problem around the world. In order to address this issue, membranes processes have been widely applied to water treatment. The main function of a membrane is to separate solvents or particulates from water [1]. For example, reverse osmosis (RO) successfully uses the membrane process to accomplish desalination and water purification. Desalination technology was expected to supply as much as 100 million m^3/d of potable water in 2015 [2]. The amount of drinking water required and supplied by utilizing membrane processes will continue to increase in the future. Due to the increasing requirement for water, it is necessary to continue search for membranes that can function in the high levels of water flux that are required for separation processes. In order to obtain enhanced water mobility, Kumar et al. introduced the idea of embedding Aquaporin (water channel protein) properties into membranes that show exceptional water permeability [3]. Some previous studies have shown that carbon nanotube (CNT) composite membranes show optimal levels of tensile strength and membrane performance [4-7]. These types of composite membranes function as a selective "water channel" to achieve a high level of water flux. The encouraging advantages shown in these successful pioneering studies have generated a great deal of interest in ways to design an artificial water channel using

biomimetic materials. Aquaporin embedded lipid bilayer membranes are said to show around 100 times higher water permeability than ordinary polymeric RO membranes [8, 9]. However, Aquaporin is fragile due to its complex three-dimensional molecular structure and is very expensive, which prevent its industrial massive application to RO membrane processes. Gramicidin A is another candidate of a novel protein channel that has a spiral structure as Aquaporin and also has excellent water permeability as well [10]. GA could be successfully introduced to a lipid bilayer of liposome, and it was expanded on to a sulfonated polyethersulfone nanofiltration support membrane to form an active layer with high water permeability and high salt rejection as an RO membrane [11]. The strong point of GA is its simpler peptide structure and, therefore, it can be relatively easily synthesized artificially, and embedded to a lipids bilayer to form a thin membrane on a porous support. Unfortunately, since GA is toxic, it should be carefully handled for its practical application. If a biomimetic membrane with an artificially designed channel whose structure is simple, stable, and safe can be prepared instead of Aquaporin or GA embedded membranes, an extremely higher water permeability than that of ordinary RO membranes made of organic polymers can be expected even under lower applied pressure conditions. This high water flux membrane enables us to save cost of drinking water production innovatively coupled with the reduction of required membrane area and foot print of a water treatment plant. In addition, these types of designed water channel has a possibility to be formed suitably for the forward osmosis (FO) membrane process in which ordinary polymeric membranes are difficult to exhibit enhanced water flux. Therefore, a biomimetic water channel is assumed to have a high potential as a novel membrane material. In order to develop a next generation type high water

flux membrane, it is indispensable to understand microscopic phenomena such as a relationship between water transport mechanisms and channel structures in molecular scale. This is an issue to be addressed for an efficient channel design, for which a computational scientific method can be useful and reasonably applied. In this study, we focused on developing suitable models for forming an artificial water channel.

Organic nanotubes have been widely studied to gain techniques and expertise in the use of their structural transport properties [12-14], and some organic nanotubes have been developed for applications such as water desalination, carbon capture, and protective coatings [15-18]. This study was focused on the properties of cyclic peptide nanotubes (CPNT). The CPNT is a type of organic nanotube that is formed through self-assembly. In 1993, Ghadiri et al. pioneered the design of CPNTs by stacking tailored cyclic peptides composed of even numbers of amino acids [19]. The CPNTs showed interesting properties including a specific nanostructure and high biocompatibility. CPNTs with hydrophobic side chains can be inserted into biological membranes [20, 21]. Due to these useful characteristics, CPNTs have high potential for applications in biology, chemistry, and materials science and were considered potential candidates for the biomimetic material used in artificial water channels.

In the development of novel materials, exploring the characteristics at the microscopic level is necessary. A large number of previous studies have used simulation to develop an artificial water channel. For instance, the mechanical properties and transport properties of carbon nanotubes have been investigated from theoretical studies [22-28]. The Gramicidin A channel model has been well explored via molecular mechanics, dynamics simulations [29-

32], and Monte Carlo simulations [33]. For the use of Aquaporin, characteristics involving single-channel water permeability [34-36], mechanisms of permeation [37, 38], and selectivity [39, 40] were investigated by computational simulation. Molecular simulation techniques have succeeded in describing how the aspect ratio of cyclic peptides can be modified by inserting a specific amino acid into a cyclic peptide [41]. The above studies have provided much useful information and have shown great agreement with the experiment data, which proves that molecular simulation is a feasible method for designing and analyzing nano-channels.

In this study, four types of nanotubes, octamer cyclic peptide, cyclo-[L-Lys-D-Ala-L-Leu-D-Ala]$_2$ (8CP) nanotube and three modified cyclic peptide nanotubes, cyclo-[L-Lys-D-Ala-L-Leu-D-Ala-L-Lys-D-Ala-γ-Mba-D-Ala] (Mba-8CP), cyclo-[L-Lys-D-Ala-γ-Mba-D-Ala-L-Lys-D-Ala-γ-Mba-D-Ala] (2Mba-8CP), and cyclo-[γ-Mba-D-Ala-γ-Mba-D-Ala-γ-Mba-D-Ala-γ-Mba-D-Ala] (4Mba-8CP), were constructed and explored. First, alterations to the inner diameter and channel volume after modification were simulated via MD techniques. Second, simulated hydrogen bonds and interaction energy distributions were analyzed for the ability to reflect the affinity between water molecules and CPNTs. Finally, MD techniques were used to explore water diffusion, and Monte Carlo (MC) simulations were introduced to study water sorption behaviors. The MC method allowed us to further investigate the effects that modified functional groups can exert on water sorption. All these analytical tools are introduced in researching four different types of simulation nanotubes within this work. Common 8CP and Mba-8CP which inspired from previous study [41], two more modified nanotubes, 2Mba-8CP and 4Mba-8CP nanotubes were constructed to further understand how

the hydrophobic functional group affect the properties of structure.. Simulated permeability can be calculated via the values of diffusivity and solubility. Thus, the simulated permeabilities of different models can be compared to analyze the value of optimized modification conditions. As a result, we found that the materials modified from common 8CP nanotubes had outstanding potential for water transportation. The modified hydrophobic functional groups enhance permeability, which is a key issue for designing an artificial water channel using biomimetic materials.

In short, the purpose of this work was to use molecular simulation to evaluate the performance of CPNTs after inserting γ-Mba-OH functional groups. Four types of nanotubes were constructed: a common 8CP and three modified versions: Mba-8CP, 2Mba-8CP, and 4Mba-8CP. The influence by hydrophobic modified functional group were be studied from two perspectives based on structural and transport features. The results showed that the modification was useful for enhancing water transport, which was proven by the MD and MC simulations for the estimation of water permeability. These information from theory calculation can be a helpful assistant for designing high performance RO or FO membranes. The details are discussed in the following sections.

2.2 Simulation method

This study was focused on how the hydrophobic functional group 3-amino-2methyl-benzoic acid (γ-Mba-OH) modifies the nanotube structures, adsorption, and transport behaviors of water molecules. Four types of CPNT molecular models, 8CP, Mba-8CP, 2Mba-8CP and 4Mba-8CP, were created based on the MD simulation procedures that were used to analyze the effects of the modified functional group. Furthermore, two simulation techniques, MD and MC, were adopted to analyze three essential features of the research: nanotube structure as well as sorption and diffusion behaviors. All these molecular models were constructed using BIOVIA Materials Studio® commercial software. The model construction, simulation parameters, and physical property estimations are shown in the following sections.

2.2.1. Cyclic peptide nanotube molecular model

As shown in Fig. 2.1, L-Lys, D-Ala, L-Leu, and D-Ala are key components that formed the common 8CP via the tailoring of cyclo-[L-Lys-D-Ala-L-Leu-D-Ala]$_2$. Moreover, the Mba modified cyclic peptide, cyclo-[L-Lys-D-Ala-L-Leu-D-Ala-L-Lys-D-Ala-γ-Mba-D-Ala] (Mba-8CP) was constructed by replacing the L-Lys with a single aromatic amino acid (γ-Mba-OH). Based on the same concept, a modified 2Mba-8CP was built by replacing one more L-Lys with γ-Mba-OH. In a similar manner, a modified 4Mba-8CP was constructed using four aromatic amino acid functional groups to replace the original two L-Lysines and two L-Leucines. The chemical structural formulas are shown in Fig. 2.2.

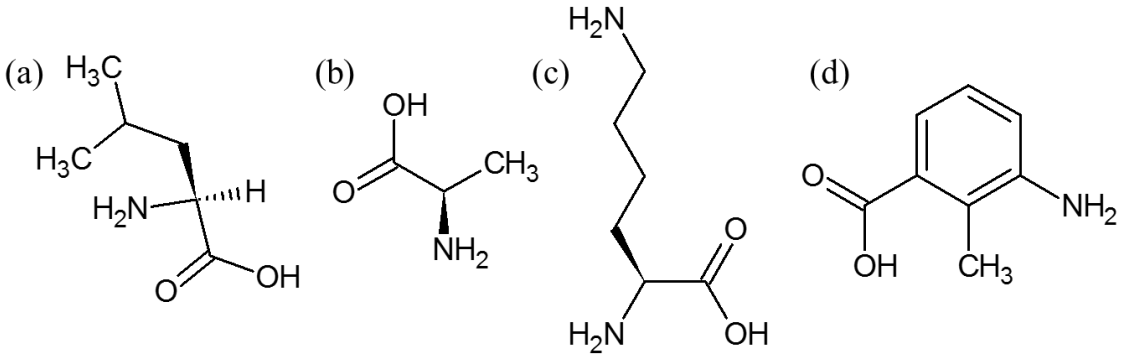

Fig. 2.1 Structures of (a) L-Lysine, (b) D-Alanine, (c) L-Leucine, and (d) 3-amino-2-methylbenzoic acid (γ-Mba-OH)

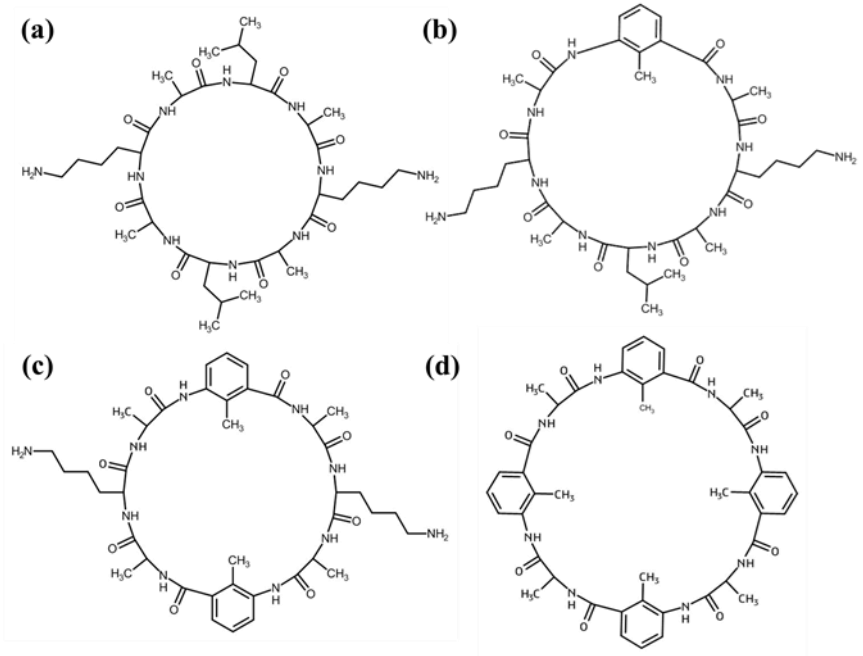

Fig. 2.2 Chemical structures of (a) conventional 8CP, (b) modified Mba-8CP, (c) modified 2Mba-8CP, and (d) modified 4Mba-8CP

In this work, each CP subunit model was built via an Amorphous Cell module. Then these cyclic peptides were used as the subunits and were stacked eight times to form CP nanotube models, according to a previously established manner [42]. The dimensional properties of these four models are shown in Table 2.1.

Table 2.1 Details of the molecular models built in this study.

	Repeat subunit	No. of Atom	Cell length [Å]
8CP	8	960	18*18*40
Mba-8CP	8	944	18*18*40
2Mba-8CP	8	928	18*18*40
4Mba-8CP	8	864	18*18*40

First, Geometry Optimization was introduced to optimize the energy of the model structure. In this process, energy calculation and changes in the structures of 5,000 iterations were carried out to establish each sensible initial nanotube structure. Afterwards, an MD duration with an NVT ensemble (fixed atom number, system volume and temperature) at 298 K for 100-ps was applied to reach molecular structures under an equilibrium state. Finally, the equilibrium structures were adopted into the structural characterization and analysis of water transport behavior. The details of the simulation procedures for preparing cyclic peptide nanotube (CPNT) models are described in the supplementary information. In this study, the Condensed-phase Optimized Molecular Potential for Atomistic Simulation Studies (COMPASS) force field [43-45] was adopted to perform the energy minimization and MD calculation processes. The various functional forms in this force field are illustrated as follows:

$$E = \sum_{b}\left[K_2(b-b_0)^2 + K_3(b-b_0)^3 + K_4(b-b_0)^4\right]$$

(a)

$$+\sum_{\theta}\left[H_2(\theta-\theta_0)^2 + H_3(\theta-\theta_0)^3 + H_4(\theta-\theta_0)^4\right]$$

(b)

$$+\sum_{\phi}\left\{V_1\left[1-\cos\left(\phi-\phi_1^0\right)\right]+V_2\left[1-\cos\left(2\phi-\phi_2^0\right)\right]+V_3\left[1-\cos\left(3\phi-\phi_3^0\right)\right]\right\}$$

(c)

$$+\sum_{x}K_x x^2 + \sum_{b}\sum_{b'}F_{bb'}(b-b_0)(b'-b'_0) + \sum_{\theta}\sum_{\theta'}F_{\theta\theta'}(\theta-\theta_0)(\theta'-\theta'_0)$$

(d) **(e)** **(f)**

$$+\sum_{b}\sum_{\theta}F_{b\theta}(b-b_0)(\theta-\theta_0) + \sum_{b}\sum_{\phi}(b-b_0)\left[V_1\cos\phi + V_2\cos 2\phi + V_3\cos 3\phi\right]$$

(g) **(h)**

$$+\sum_{b'}\sum_{\phi}(b'-b'_0)\left[V_1\cos\phi + V_2\cos 2\phi + V_3\cos 3\phi\right]$$

(i)

$$+\sum_{\phi}\sum_{\theta}\sum_{\theta'}K_{\phi\theta\theta'}\cos\phi(\theta-\theta_0)(\theta'-\theta'_0) + \sum_{i>j}\frac{q_i q_j}{\varepsilon r_{ij}} + \sum_{i>j}\left[\frac{A_{ij}}{r_{ij}^9} - \frac{B_{ij}}{r_{ij}^6}\right] \qquad (1)$$

(j) **(k)** **(l)**

The energy terms are composed of three categories: bonded energy terms, cross-interaction terms, and non-bonded energy terms. The bonded energy terms include (a) the covalent bond-stretching energy terms, (b) the bond-angle bending energy terms, and (c) the torsion-angle rotation energy terms. The designation (d) is either the out-of-plane energy, or an improper term. The terms for cross-interaction consist of the dynamic variations among bond stretching, bending, and torsion angle rotation interactions ((e)–(j)). The non-bonded energy terms, (k) and (l), represent the Coulombic electrostatic interaction force and the van der Waals (vdW) potential force, respectively.

2.2.2. Physical property analysis

The aim was to elucidate the structural properties and water-molecule transport behaviors in cyclic peptide nanotubes by applying MD simulation techniques. Details of the physical properties are described in this section.

2.2.2.1 Structural characteristics

To describe how the γ-Mba-OH functional group modification altered the channel morphology of the CP nanotubes, the inner diameter and channel volume were considered. First, the inner diameter of each cyclic peptide subunit was estimated to compare the channel morphology between the simulation models. Second, the channel volumes were analyzed to understand how their free volumes might affect the transport of water molecules through the nanotubes. Both the internal diameter and channel volume were estimated based on the van der Walls radii of the simulation models obtained using the Visualizer Module in BIOVIA Materials Studio® commercial software.

2.2.2.2 Hydrogen bond analysis

The affinity between water molecules and nanotubes is an important factor for water mobility in CPNTs. Thus, the distribution of hydrogen bonds was analyzed to explore the inner affinity of the nanotube simulation models. The standards of hydrogen bond analysis were listed in supplementary information. The distribution of the hydrogen bonds between water molecules and nanotubes was obtained using the Visualizer Module in BIOVIA Materials Studio® commercial software.

2.2.2.3 Water transportation behavior

The process of water molecule sorption in nanotubes can be described using the Grand Canonical Monte Carlo (GCMC) method. During the simulation, the relative probabilities of the different states of a system were simulated using the Metropolis algorithm. There are four types of configurations for adsorbed water molecules: conformer, rotation, translation, and regrowth. The detail theory of sorption calculation was shown in supplementary information. The sorption analysis calculation in this work was processed one million times. The number of water molecules that were adsorbed by the inner peptide nanotube was recorded and the sorption loading was evaluated as a function of the water vapor pressure.

2.2.2.4 Mean-squared displacement (MSD)

The mean-squared displacement (MSD) of water molecules in CPNTs was calculated using *NVT* MD simulation to analyze the differences in the diffusion behaviors of water molecules for each of the CPNT models. The diffusion coefficient of water in CPNTs can be easily obtained using the Einstein relationship:

$$MSD(t) = \frac{1}{N}\sum_{i=1}^{N}\{[r_i(t_0+t) - r_i(t_0)]^2\} = B + 6D \times \mathrm{t} \qquad (2)$$

where N is the total number of atoms, r_i (t_0+t) and r_i (t_0) are the positions at time t_0+t and time t_0, respectively, B is a constant, and D is the diffusion coefficient. The diffusion coefficient can be calculated from the slope of the MSD curve. In general, the biomimetic membranes such as CPNTs was surrounded with a lot of lipids to stable the channel structure. It is took

giant calculation cost under this state. In order to reduce the load of computer and simulation time, $CHCl_3$ molecule were added to replace the lipids layer. These 10 molecules were added as solvent to protect the nanotube structure. These solvent molecules can stabilize the channel complex. This method was used in previous study too [46]. In this work, 25 water molecules were inserted into a nanotube and a 1-ns calculation period was provided to obtain the MSD diagrams as a function of elapsed MD simulation time.

2.3. Results and discussion

2.3.1. Model validation

To confirm the feasibility of all the molecular models in this work, we first constructed two types of cyclic peptide nanotube models (CPNT models) to validate the correctness and applicability of the simulation. Two CPNT models with prototypical octamer CPs composed of the sequence cyclo-[L-Lys-D-Ala-L-Leu-D-Ala]$_2$ (8CP) and modified with Mba-8CP were established for the model validation. The model structures of these cyclic peptide nanotubes were experimentally investigated [41], and the inner diameters were found to be tunable via the insertion of a specific functional group. The equilibrated structures of these two types of nanotubes were achieved by MD simulation using NVT ensemble calculation. Fig. 2.3 shows the internal diameters of the 8CP and Mba-8CP, as estimated based on the van der Waals radii. The shape of the nanotube was changed by the γ-Mba-OH functional group, which disrupted the inner symmetrical structure. As a result, the internal diameter was reduced from 10.3 Å in 8CP to 7.5 Å in Mba-8CP. The difference between the original and the modified version was 28%. In a previous study [41], the diameter of Mba-8CP is estimated to be 4.7

Å, and the 7.6 Å of the 8CP nanotube, a 38% reduction in size after modification was reported. The mismatch between these two results could have been caused by a different method for the model construction and by the adoption of a different force field. Although the values were different, the changes in the channel aspect ratio and in the reduction of the inner diameter were successful, which was a tendency that was qualitatively similar to that observed in a previous study. Thus, in this work, the simulation model for describing the effect by hydrophobic functional group in CPNTs including structural catachrestic and transport behavior is convincing.

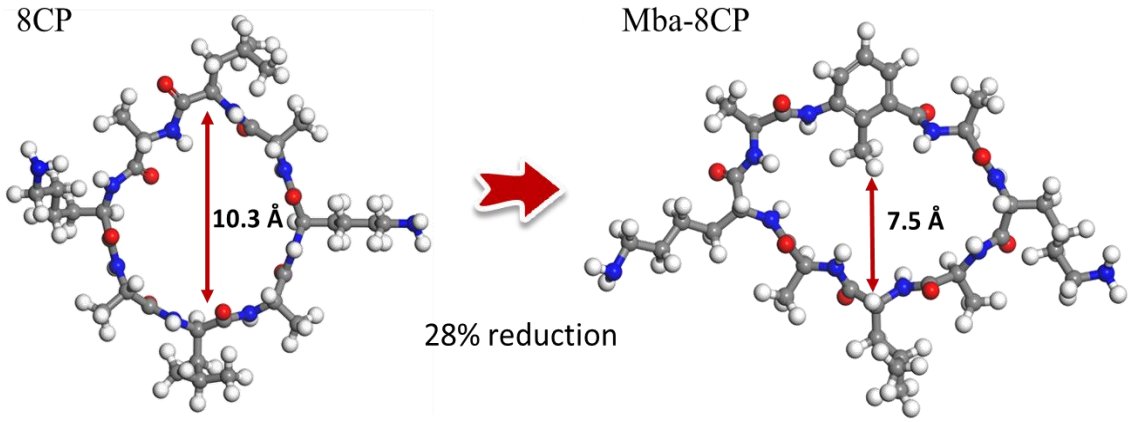

Fig. 2.3 Change in ring size and shape caused by replacing an L-Lysine with γ-Mba-OH (from 8CP to Mba-8CP).

2.3.2. Channel volume analysis

The four types of nanotube models (8CP, Mba-8CP, 2Mba-8CP and 4Mba-8CP) are shown in Fig. 2.4. The upper side of Fig. 2.4 shows the top view of their structures, and demonstrates the different aspect ratios in the ring structures of the four nanotubes. This was caused when the symmetry of the interior structure was disrupted by the modified γ-Mba-OH functional

group. Slight tilts were also observed in the regions of the aromatic rings of γ-Mba-OH in the three modified models of the side views of the structures, as shown in the downside of Fig. 2.4. These structural features of asymmetry and tilt in the modified nanotubes agreed with the findings in a previous study on simulation [41].

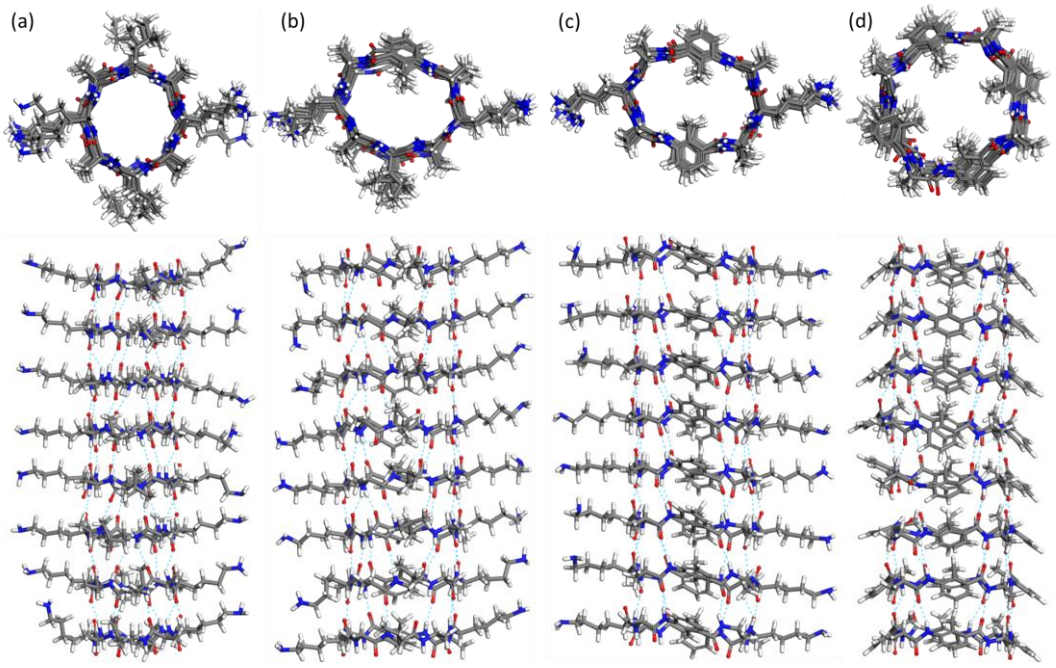

Fig. 2.4 CPNT structures of (a) conventional 8CP, (b) modified Mba-8CP, (c) modified 2Mba-8CP, and (d) modified 4Mba-8CP prepared by Materials Studio® software.

The characteristics of the channel volume size and shape were dominant factors in the water transport performance. To study the effect exerted by the channel volume change with the hydrophobic functional group modification, the volume and morphology of CPNTs was examined in detail. Four different configurations are shown in Fig. 2.5, which provided information on the effect of morphology. The blue regions represent the volume occupied by nanotubes, the black regions indicate the pathways inside the nanotubes. In the case of the

8CP nanotube, the tunnel was presented as a circle. However, the other three channels were transformed by varying the numbers of γ-Mba-OH functional groups. From the snapshot of 2Mba-8CP, the complete channel was divided into two smaller tunnels, which could have increased the barrier for water diffusion in the nanotubes.

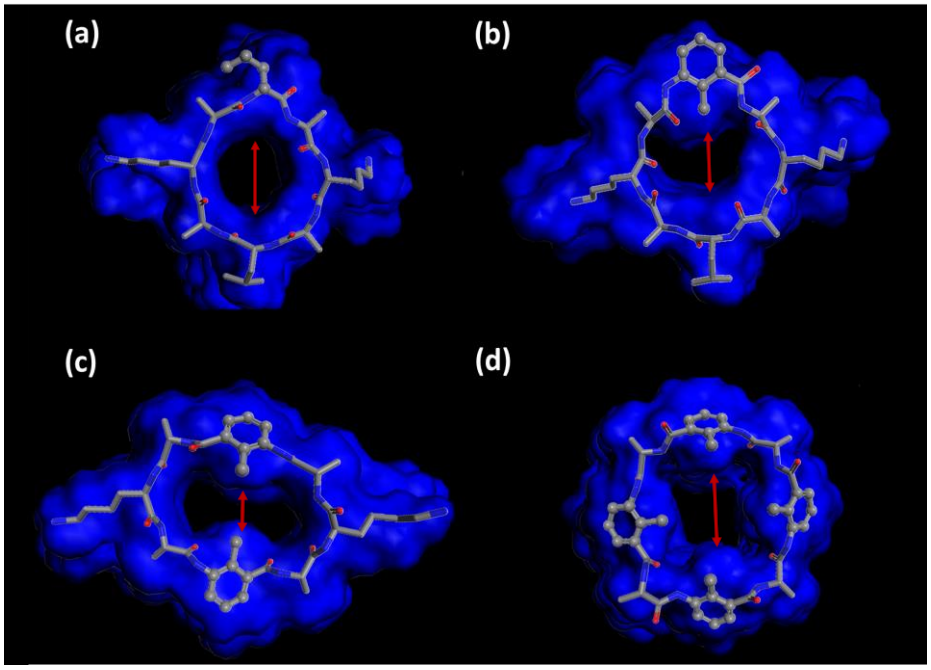

Fig.2.5 Channel volume morphology of (a) conventional 8CP, (b) modified Mba-8CP, (c) modified 2Mba-8CP, and (d) modified 4Mba-8CP.

The results of the internal diameter and channel volume calculated from the data are shown in Table 2.2. Although the internal diameter was decreased by the modification, there was no clear trend for the internal diameters of each model with increases in the number of modified functional groups. On the other hand, the channel volumes of the three modified simulation models were increased to different levels. The detailed analysis of the effects of these factors will be discussed in the next section.

Table 2.2 Details of the internal diameter and channel volume of the simulated models constructed in this work.

	Internal Diameter [Å]	Channel Volume [Å^3]
8CP	10.3	1320
Mba-8CP	7.51	1460
2Mba-8CP	5.58	1430
4Mba-8CP	8.30	1970

2.3.3. Hydrogen bond and Interaction energy analysis

As mentioned in previous discussions, this research was undertaken to enhance the diffusivity of water molecules by adjusting the hydrophilicity of a common CPNT. To understand how the affinity between water molecules and nanotubes affects the transport behavior of water, the hydrogen bonds between CPNTs and water molecules were discussed. The distribution of the hydrogen bonds between the CPNTs and water molecules in the four types of molecular models is presented in Fig. 2.6. From the observations of each of these models, the hydrogen-bond distributions were obviously altered when γ-Mba-OH functional groups were introduced to the channel. In other words, the regions modified by γ-Mba-OH functional groups were apparently changed to hydrophobic segments. This finding agrees with the fact that a γ-Mba-OH functional group has a methyl group, which is hydrophobic in nature and can possibly show low affinity to water molecules. As indicated in Fig. 2.7, the number of hydrogen bonds between a nanotube and water molecules was decreased with the addition of more γ-Mba-OH functional groups. The 2Mba-8CP simulation model, however, showed exceptional behavior. That is, the number of hydrogen bonds was unexpectedly

greater than that of the Mba-8CP model and a little lower than that in the unmodified 8CP model. This could have been the result of two prominent γ-Mba-OH functional groups of the 2Mba-8CP model dividing the channel space into two smaller pore regions, where the interaction between a water molecule and the nanotube was enhanced due to the water molecules being closely surrounded by other major hydrophilic groups. The largest number of hydrogen bonds was observed in the 8CP nanotube molecular model. Thus, the 8CP structure showed the highest level of water affinity of all the molecular simulation models examined in this study. The number of hydrogen bonds and the level of hydrophilicity of the 8CP nanotube model both were reduced by the γ-Mba-OH functional group modification.

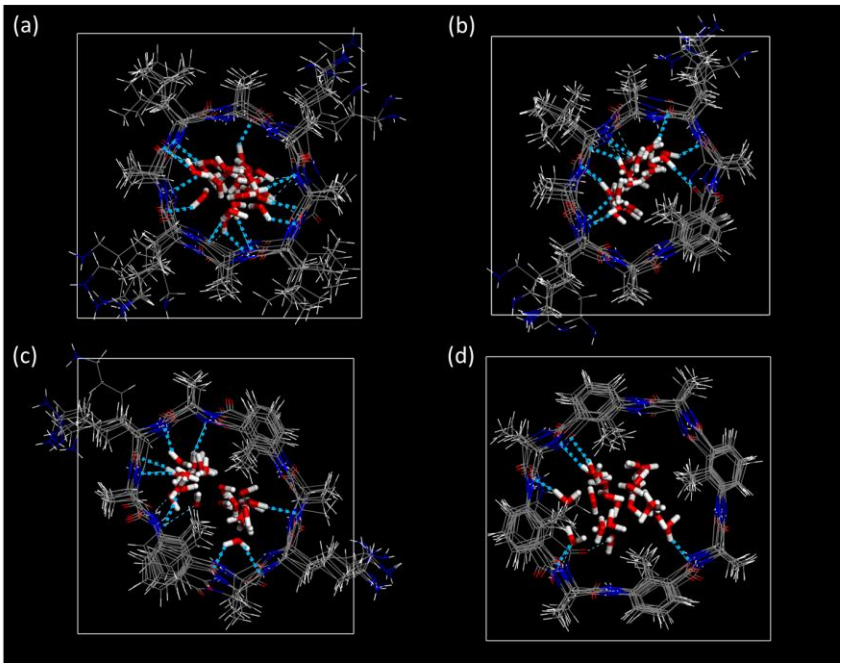

Fig.2.6 Hydrogen bonds between water molecules and (a) conventional 8CP, (b) modified Mba-8CP, (c) modified 2Mba-8CP, and (d) modified 4Mba-8CP nanotubes. (Hydrogen bond is represented by a blue dotted line.)

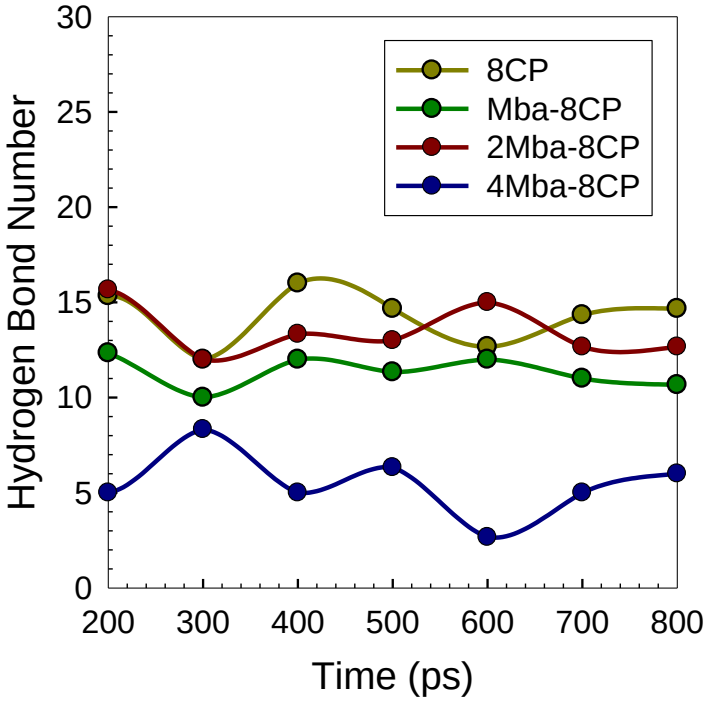

Fig.2.7 Time course of the number of hydrogen bonds between water molecules and a CP nanotube under a steady state during NVT simulations.

Further, quantized interaction energies between water molecules and the nanotube were calculated and are compared in Fig. 2.8(a). The observed interaction energies were clustered around the mean values with a small level of deviation. The order of the interaction energy was similar to that of the hydrogen bond, as shown in Fig. 2.7. The Mba-8CP model showed the highest attractive interaction, which was caused by the hydrophilicity of the nanotube. The 8CP model showed attractive interactions that were lower than that of the Mba-8CP, which had the smallest channel volume. For the 4Mba-8CP simulation model, the interaction energy changed from attraction (negative) to repulsion (positive). The 2Mba-8CP version showed the lowest level of attractive interaction because the interaction energy was simultaneously affected by strong attractive and repulsive forces.

The interaction energy was further examined via van der Waals (vdW) and Coulombic energy comparisons. As shown in Fig. 8(b), the vdW energy was affected by channel volume and by the hydrophobic functional groups used to modify the CPNTs. The 2Mba-8CP version showed the highest value, which implied that the two prominent γ-Mba-OH functional groups had strongly repulsed the water molecules within the nanotube. The Mba-8CP and 4Mba-8CP versions showed lower values because of the enlarged channel volume following modifications. Although the 8CP version had the smallest channel volume from among these four types, the vdW energy value was not considered high. The carbon atoms that form the nanotube backbone easily repulsed the water molecules in the 8CP model.

The values for Coulombic energy are shown in Fig. 8(c). First, the highest Coulombic energy was shown by the 4Mba-8CP version, which obviously was caused by its hydrophobicity, and this is consistent with the results of the hydrogen bond numbers shown in Fig. 7. Next, the 8CP and Mba-8CP versions showed simular values due to hydrophilicity. The 2MBa-8CP, which is indeed hydrophilic, showed the lowest value for average Coulombic energy. This revealed the great attractive interaction energy that the 2MBa-8CP version had with water.

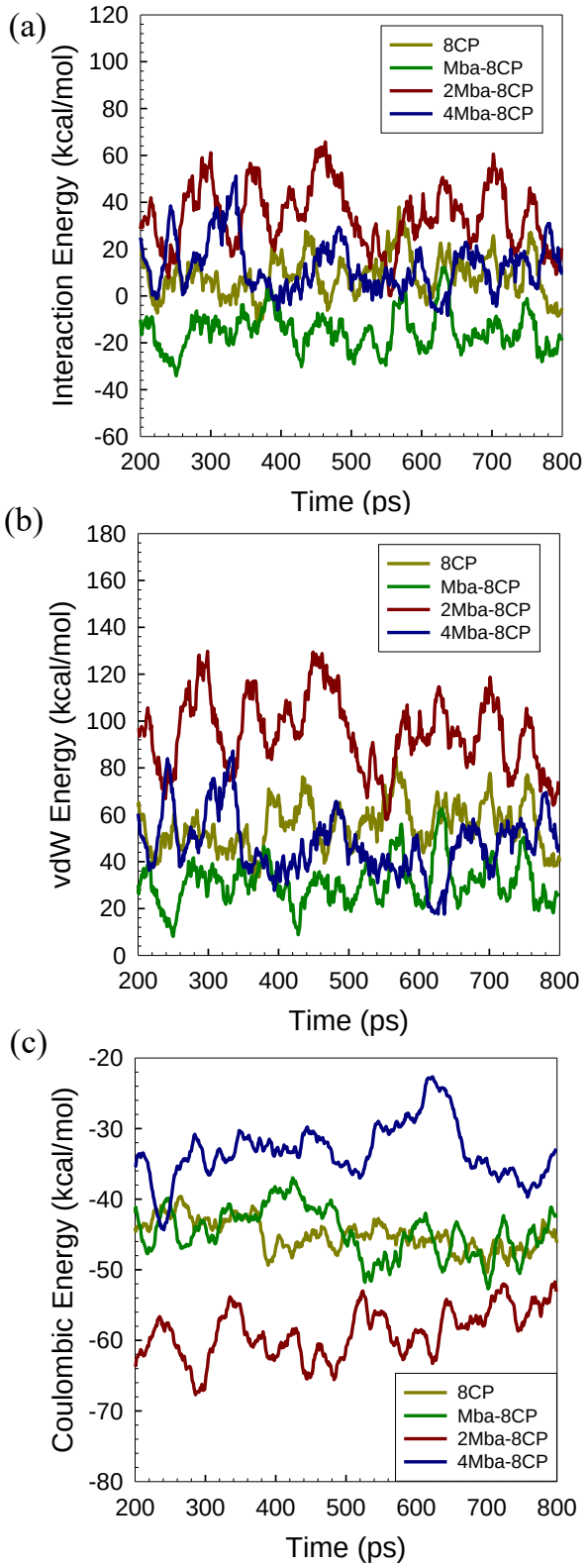

Fig.2.8 Time course of (a) interaction energy, (b) vdW energy and (c) coulombic energy between water molecules and a CP nanotube under a steady state during NVT simulations.

2.3.4. Molecular transport behaviors

The solution-diffusion mode can be used to examine transport behavior during theoretical calculation [47]. In other words, permeability is dependent on both the sorption and diffusion behaviors. Therefore, these two dominating factors will be discussed separately in order to promote full development of an understanding of water transport in modified CPNTs.

(a) Sorption of water molecules: The sorption sites of water molecules in the 8CP, Mba-8CP, 2Mba-8CP, and 4Mba-8CP nanotube models are shown in Fig. 2.9. The molecules tended to adsorb on the inner surface of the nanotube channel. Also, the sorption locations fit well with the channel configurations of each of the nanotubes. This result agreed well with the previous analyses of morphology in section 2.3.2.

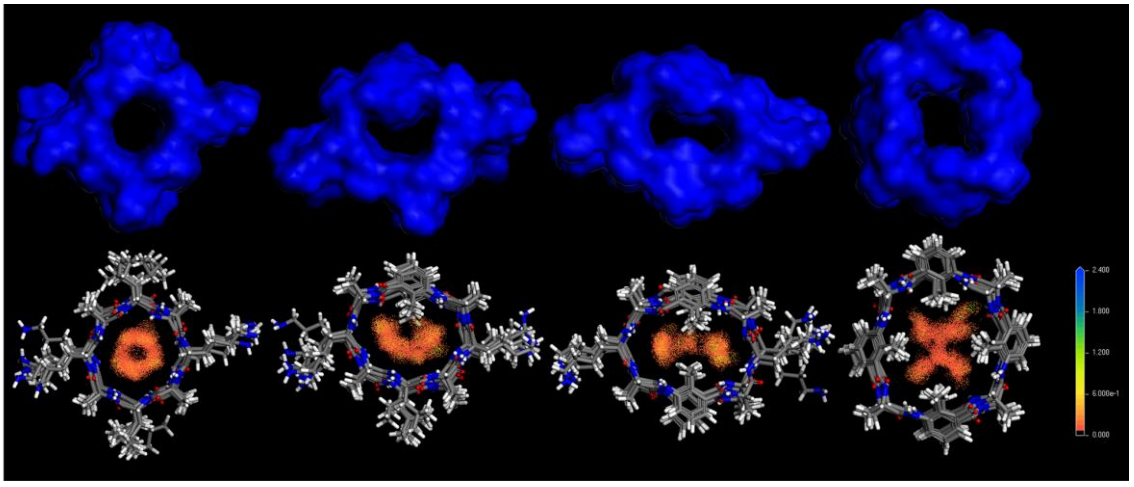

Fig.2.9 Sorption sites of water molecules in the four types of nanotubes.

Moreover, the channel volume and water-nanotube affinity could affect the sorption behaviors. To further understand the sorption behaviors inside the nanotubes, the sorption isotherms of the 8CP, Mba-8CP, 2Mba-8CP and 4Mba-8CP nanotubes were examined. Fig.

2.10 shows the water molecular sorption isotherms at 298 K up to a pressure of 1 atm. The sorption isotherm curves indicated two particular sorption behaviors for different CPNT models. One was that the high affinity between water molecules and nanotubes introduced the hydrophilic adsorption phenomenon, which was expressed in the curves of the conventional 8CP, Mba-8CP and 2Mba-8CP models. Second, in the 4Mba-8CP nanotube, the shape of the adsorption isotherm was of the type-III form, as it is referred to in the BDDT classification [48]. This form is characterized by a convex and downward orientation, and is often observed in adsorbate-phobic materials. This was expected because of the high number of modified γ-Mba-OH functional groups, which changed the properties of the nanotube inner surface from hydrophilic to hydrophobic.

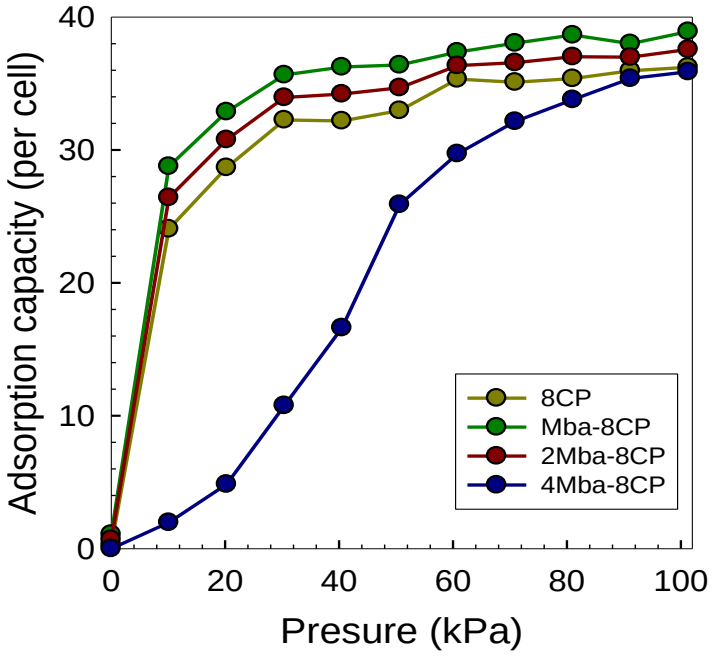

Fig.2.10 Sorption isotherms of water molecules in the four types of nanotubes.

(b) MSD and diffusivity: Fig.2.11 shows the mean square displacement (MSD) diagrams of water molecules for the four types of nanotubes during the *NVT* MD simulation for a period of 1 ns. The displacement and slope indicated the transport ability of water molecules inside the nanotube. In the 4Mba-8CP nanotube model, large values were observed for the displacement and slope, which indicated high mobility of water molecules. This result was due to the largest channel volume and lowest affinity to water molecules inside the nanotube from among the four CPNTs. The larger internal volume provided more space and less of a transport barrier. The hydrophobic functional groups allowed water molecules to move more rapidly inside the cyclic peptide nanotube.

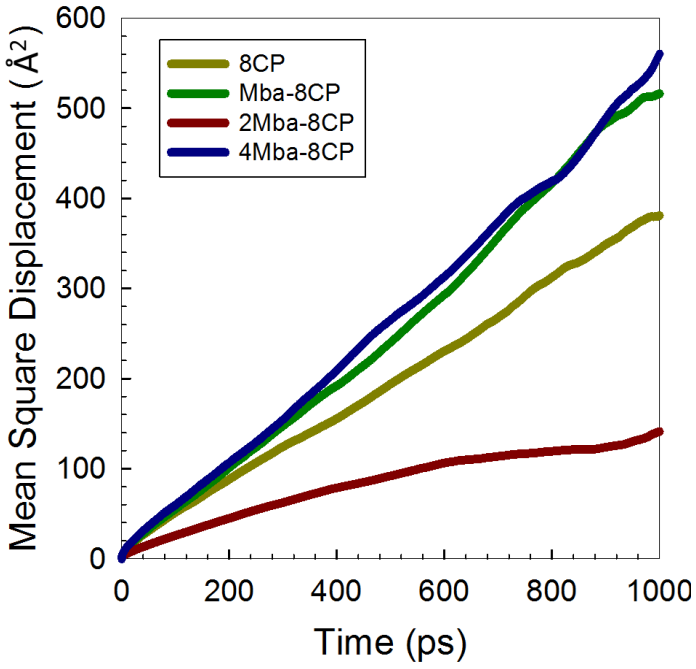

Fig.2.11 MSD curves of water in the four types of nanotube models.

In general, an increase in the number of γ-Mba-OH functional groups introduced into a nanotube enhanced its water transport performance. As shown by the 4Mba-8CP model

discussed above, this was the result of a larger channel volume and a lower affinity for water. As shown by the MSD curves, the 2Mba-8CP model provided extremely low water transport. The modification using two γ-Mba-OH functional groups only slightly increased the channel volume, but it significantly decreased the internal diameter (Table 2.2). In this situation, the two protruding modified functional groups were placed too closely together, and they divided the inner space of the nanotube from one large channel to two smaller tunnels, as shown in Fig. 2.5. This apparently increased the barrier of water molecular diffusivity, which reflected a lower level of displacement and a lower slope in the MSD curve.

(c) Water permeability: The overall permeability was based on the solubility and diffusivity by the solution-diffusion model [47]. The values for the solubility and diffusivity coefficients of the four types of simulation models are shown in Table 2.3. We calculated the values of water permeability based on the sorption and diffusion simulations of the four types of nanotubes. Fig. 2.12 shows the permeability data that was calculated for this study. The water permeability data showed how the water molecular permeation behaviors for different types of nanotubes were dominated by both the diffusion and sorption mechanisms. The highest permeability value was observed for the Mba-8CP model, which was followed in order by the 8CP, 2Mba-8CP, and 4Mba-8CP models. The different trends that the permeability and diffusion data reveal is noteworthy. In particular, the 4Mba-8CP model presented completely opposite properties with respect to these two forms of data. As previously discussed, the 4Mba-8CP model provided a large space for diffusion and no barriers to the diffusion analysis. Nonetheless, this model also showed the lowest levels of permeability. To understand this controversial result, the different viewpoints of affinity and

diffusivity must be accounted for in the valence of solubility and how these are affected by the geometry of nanotubes. The point is that both the solubility and diffusivity are affected by affinity. Low levels of nanotube-water affinity create difficulties for the adsorption of water molecules in low-pressure regions. As a result, low amounts of adsorption lead to low levels of solubility, which then leads to low levels of permeability. On the other hand, the permeability of the 2Mba-8CP model was lower than that of either the 8CP or Mba-CP models, which was due to the low contribution to MSD.

Table 2.3 Diffusivity and solubility coefficients of the four types of nanotube models.

	Diffusion Coefficient [m^2/s]	Solubility Coefficient [mol/m^3]
8CP	$1.9*10^{-9}$	2.99
Mba-8CP	$2.6*10^{-9}$	3.23
2Mba-8CP	$7.1*10^{-10}$	2.52
4Mba-8CP	$2.8*10^{-9}$	0.16

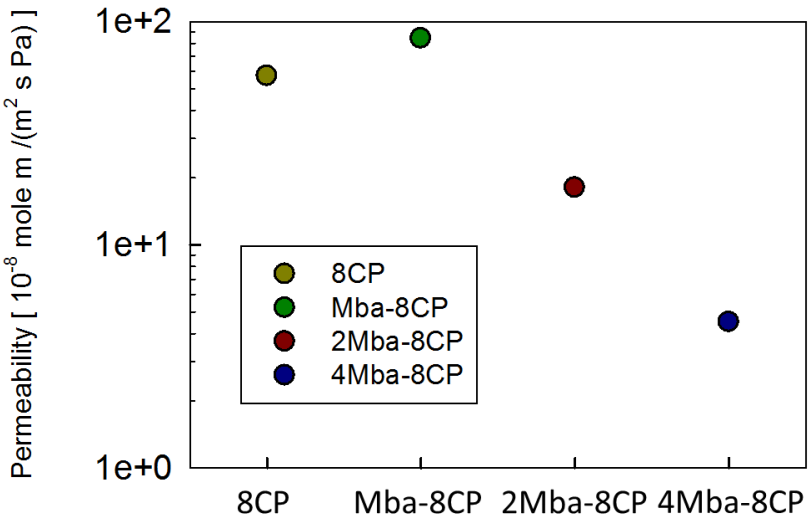

Fig.2.12 Water permeability in the four types of nanotube models.

As an artificial water channel, the predictive water permeabilities were compared to the experimental data of real aquaporin channel. The average single-channel osmotic water permeability in AQPs is 4×10^9 (water molecules per s), and effective channel radii is measured as 1.4 Å [49] and osmotic pressure is 29.6 atm which obtain from Van't Hoff equation. After convert, permeability value of AQPs channel turn to 0.04 (mol $m^{-2}\ s^{-1}\ Pa^{-1}$). On the other hand, the predication value of four types of CPNTs in this work is 0.25~1.68 (mol $m^{-2}\ s^{-1}\ Pa^{-1}$). There is some divergence in the comparison, which was attributed to the over-estimated water molecule adsorption. The vapor phase permeability presented in this work which is much higher than experimental liquid phase data as shown in pioneer study. Although with some incongruity in comparison, the qualitative relationship in different CPNTs were described. Accurately illustrating the channel structure and effectively predicting the water molecule transport in the qualitative investigation is necessary. In this work, the Mba-8CP modified nanotube model showed high

permeability, which could provide high efficiency in the water transport process for a wide range of applications. Thus, the permeability results demonstrated that the transport ability of water through CPNTs could be adjusted via the modification of some specific functional groups.

2.4. Conclusions

The structural characteristics and transport behaviors of the 8CP, Mba-8CP, 2Mba-8CP, 4Mba-8CP models of nanotubes were thoroughly analyzed via MD and MC. The channel morphology and internal diameter results revealed that the modification with a γ-Mba-OH functional group disrupted the symmetry by adjusting the channel morphology. The simulated channel volume suggested that internal volume size of the CP nanotube was enlarged at different levels after the modification. Hydrogen bond analysis indicated that modification of the nanotubes changed the affinity between water molecules and the CPNTs. The results demonstrated that an increase in the number of γ-Mba-OH functional group segments in nanotube models increased the level of hydrophobicity. In other words, the nanotube structures that contained hydrophobic γ-Mba-OH functional groups had fewer attractive interactions with water molecules. Based on the channel volume and hydrogen bond distribution analyses, the Mba-8CP and 4Mba-8CP modified nanotube models had a larger channel volume and a lower affinity to water molecules. In the 2Mba-8CP model, however, the total channel volume was divided into two smaller tunnels by the two protruding γ-Mba-OH functional groups, which increased the diffusivity barrier in this modification situation. In addition, although transport behavior was dominated by molecular diffusion, it

also was controlled by sorption behavior. The performance of sorption behavior was governed by the channel volume and by the affinity to water of the inner CP nanotube. Among the four different nanotubes tested, the affinity of the nanotubes to water molecules was the critical issue. The 4Mba-8CP model was modified by four γ-Mba-OH functional groups, and this model was the most hydrophobic in nature. In this case, water molecules had difficulty being adsorbed in the low-pressure regions of nanotubes due to low affinity. By combining the results of diffusion and sorption, the Mba-8CP model showed the largest predicted level of permeability due to the low diffusion barrier presented by the channel surface and volume and also to a moderately attractive interaction with water molecules. The 2Mba-8CP and 4Mba-8CP models showed relatively poor performances in permeability due to a divided small channel volume and a low level of sorption behavior, respectively.

In summary, the addition of a 3-amino-2-methylbenzoic acid (γ-Mba-OH) functional group increased the channel volume and adjusted the inner affinity of CPNTs. The larger channel volume and lower affinity of nanotubes for water molecules enhanced the water transport ability in CPNTs. However, the results in this study show that the transport behavior inside nanotubes is simultaneously controlled by molecular diffusion and sorption behavior, which shows that finding the optimized modification conditions is important in the design of a high-performance water channel. Molecular simulation shows great promise as a method that could assist in the design and development of nanotube material.

2.5 References

[1] D. Sammon, Membrane processes, Pure and Applied Chemistry, 37 (1974) 423-436.
[2] K. Wangnick, International Desalination Association (IDA), in, Worldwide Desalting Plants Inventory Report, 2004.
[3] M. Kumar, M. Grzelakowski, J. Zilles, M. Clark, W. Meier, Highly permeable polymeric membranes based on the incorporation of the functional water channel protein Aquaporin Z, Proceedings of the National Academy of Sciences, 104 (2007) 20719-20724.
[4] L. Brunet, D.Y. Lyon, K. Zodrow, J.-C. Rouch, B. Caussat, P. Serp, J.-C. Remigy, M.R. Wiesner, P.J. Alvarez, Properties of membranes containing semi-dispersed carbon nanotubes, Environmental Engineering Science, 25 (2008) 565-576.
[5] E. Celik, H. Park, H. Choi, H. Choi, Carbon nanotube blended polyethersulfone membranes for fouling control in water treatment, Water research, 45 (2011) 274-282.
[6] J.-H. Choi, J. Jegal, W.-N. Kim, Fabrication and characterization of multi-walled carbon nanotubes/polymer blend membranes, Journal of Membrane Science, 284 (2006) 406-415.
[7] S. Kim, J.R. Jinschek, H. Chen, D.S. Sholl, E. Marand, Scalable fabrication of carbon nanotube/polymer nanocomposite membranes for high flux gas transport, Nano letters, 7 (2007) 2806-2811.
[8] M.Ø. Jensen, O.G. Mouritsen, Single-channel water permeabilities of Escherichia coli aquaporins AqpZ and GlpF, Biophysical journal, 90 (2006) 2270-2284.
[9] P. Pohl, S.M. Saparov, M.J. Borgnia, P. Agre, Highly selective water channel activity measured by voltage clamp: analysis of planar lipid bilayers reconstituted with purified AqpZ, Proceedings of the National Academy of Sciences, 98 (2001) 9624-9629.
[10] P.A. Rosenberg, A. Finkelstein, Water permeability of gramicidin A-treated lipid bilayer membranes, The Journal of general physiology, 72 (1978) 341-350.
[11] D. Saeki, T. Yamashita, A. Fujii, H. Matsuyama, Reverse osmosis membranes based on a supported lipid bilayer with gramicidin A water channels, Desalination, 375 (2015) 48-53.
[12] G. Chen, S. Su, R. Liu, Theoretical Studies of Monomer and Dimer of Cyclo [(-l-Phe 1-d-Ala 2-) n] and Cyclo [(-l-Phe1-d-Me N-Ala2-) n](n= 3-6), The Journal of Physical Chemistry B, 106 (2002) 1570-1575.
[13] J.P. Lewis, N.H. Pawley, O.F. Sankey, Theoretical Investigation of the Cyclic Peptide System Cyclo [(d-Ala-Glu-d-Ala-Gln) m= 1-4], The Journal of Physical Chemistry B, 101 (1997) 10576-10583.
[14] Z. Liu, Y. Xu, P. Tang, Steered molecular dynamics simulations of Na+ permeation across the gramicidin A channel, The Journal of Physical Chemistry B, 110 (2006) 12789-12795.
[15] D.L. Gin, R.D. Noble, Designing the next generation of chemical separation membranes, Science, 332 (2011) 674-676.
[16] M.S. Kaucher, M. Peterca, A.E. Dulcey, A.J. Kim, S.A. Vinogradov, D.A. Hammer, P.A. Heiney, V. Percec, Selective transport of water mediated by porous dendritic dipeptides, Journal of the American Chemical Society, 129 (2007) 11698-11699.

[17] M.A. Shannon, P.W. Bohn, M. Elimelech, J.G. Georgiadis, B.J. Marinas, A.M. Mayes, Science and technology for water purification in the coming decades, Nature, 452 (2008) 301-310.
[18] T. Xu, N. Zhao, F. Ren, R. Hourani, M.T. Lee, J.Y. Shu, S. Mao, B.A. Helms, Subnanometer porous thin films by the co-assembly of nanotube subunits and block copolymers, ACS nano, 5 (2011) 1376-1384.
[19] M.R. Ghadiri, J.R. Granja, R.A. Milligan, D.E. McRee, N. Khazanovich, Self-assembling organic nanotubes based on a cyclic peptide architecture, Nature, 366 (1993) 324-327.
[20] S. Fernandez-Lopez, H.-S. Kim, E.C. Choi, M. Delgado, J.R. Granja, A. Khasanov, K. Kraehenbuehl, G. Long, D.A. Weinberger, K.M. Wilcoxen, Antibacterial agents based on the cyclic D, L-α-peptide architecture, Nature, 412 (2001) 452-455.
[21] W.S. Horne, C.M. Wiethoff, C. Cui, K.M. Wilcoxen, M. Amorin, M.R. Ghadiri, G.R. Nemerow, Antiviral cyclic d, l-α-peptides: Targeting a general biochemical pathway in virus infections, Bioorganic & medicinal chemistry, 13 (2005) 5145-5153.
[22] T. Belytschko, S. Xiao, G.C. Schatz, R. Ruoff, Atomistic simulations of nanotube fracture, Physical Review B, 65 (2002) 235430.
[23] G. Hummer, J.C. Rasaiah, J.P. Noworyta, Water conduction through the hydrophobic channel of a carbon nanotube, Nature, 414 (2001) 188-190.
[24] K. Koga, G. Gao, H. Tanaka, X.C. Zeng, Formation of ordered ice nanotubes inside carbon nanotubes, Nature, 412 (2001) 802-805.
[25] D.J. Mann, M.D. Halls, Water alignment and proton conduction inside carbon nanotubes, Physical review letters, 90 (2003) 195503.
[26] A. Waghe, J.C. Rasaiah, G. Hummer, Filling and emptying kinetics of carbon nanotubes in water, The Journal of chemical physics, 117 (2002) 10789-10795.
[27] Z. Yao, C.-C. Zhu, M. Cheng, J. Liu, Mechanical properties of carbon nanotube by molecular dynamics simulation, Computational Materials Science, 22 (2001) 180-184.
[28] U. Zimmerli, P.G. Gonnet, J.H. Walther, P. Koumoutsakos, Curvature induced L-defects in water conduction in carbon nanotubes, Nano letters, 5 (2005) 1017-1022.
[29] W. Lee, P.C. Jordan, Molecular dynamics simulation of cation motion in water-filled gramicidinlike pores, Biophysical journal, 46 (1984) 805.
[30] D. Mackay, P.H. Berens, K.R. Wilson, A. Hagler, Structure and dynamics of ion transport through gramicidin A, Biophysical journal, 46 (1984) 229.
[31] A. Skerra, J. Brickmann, Structure and dynamics of one-dimensional ionic solutions in biological transmembrane channels, Biophysical journal, 51 (1987) 969.
[32] A. Skerra, J. Brickmann, Simulation of voltage-driven hydrated cation transport through narrow transmembrane channels, Biophysical journal, 51 (1987) 977.
[33] K. Kim, D. Vercauteren, M. Welti, S. Chin, E. Clementi, Interaction of K+ ion with the solvated gramicidin A transmembrane channel, Biophysical journal, 47 (1985) 327.
[34] M. Hashido, A. Kidera, M. Ikeguchi, Water transport in aquaporins: osmotic permeability matrix analysis of molecular dynamics simulations, Biophysical journal, 93 (2007) 373-385.

[35] F. Zhu, E. Tajkhorshid, K. Schulten, Theory and simulation of water permeation in aquaporin-1, Biophysical Journal, 86 (2004) 50-57.
[36] F. Zhu, E. Tajkhorshid, K. Schulten, Collective diffusion model for water permeation through microscopic channels, Physical review letters, 93 (2004) 224501.
[37] B.L. de Groot, H. Grubmüller, Water permeation across biological membranes: mechanism and dynamics of aquaporin-1 and GlpF, Science, 294 (2001) 2353-2357.
[38] D.F. Savage, P.F. Egea, Y. Robles-Colmenares, J.D. O'Connell III, R.M. Stroud, Architecture and selectivity in aquaporins: 2.5 Å X-ray structure of aquaporin Z, PLoS Biol, 1 (2003) e72.
[39] J.S. Hub, B.L. de Groot, Does CO 2 permeate through Aquaporin-1?, Biophysical journal, 91 (2006) 842-848.
[40] J.S. Hub, B.L. De Groot, Mechanism of selectivity in aquaporins and aquaglyceroporins, Proceedings of the National Academy of Sciences, 105 (2008) 1198-1203.
[41] R. Hourani, C. Zhang, R. van der Weegen, L. Ruiz, C. Li, S. Keten, B.A. Helms, T. Xu, Processable cyclic peptide nanotubes with tunable interiors, Journal of the American Chemical Society, 133 (2011) 15296-15299.
[42] M.R. Ghadiri, K. Kobayashi, J.R. Granja, R.K. Chadha, D.E. McRee, The Structural and Thermodynamic Basis for the Formation of Self‐Assembled Peptide Nanotubes, Angewandte Chemie International Edition in English, 34 (1995) 93-95.
[43] D. Rigby, H. Sun, B. Eichinger, Computer simulations of poly (ethylene oxide): force field, pvt diagram and cyclization behaviour, Polymer International, 44 (1997) 311-330.
[44] H. Sun, COMPASS: an ab initio force-field optimized for condensed-phase applications overview with details on alkane and benzene compounds, The Journal of Physical Chemistry B, 102 (1998) 7338-7364.
[45] H. Sun, P. Ren, J. Fried, The COMPASS force field: parameterization and validation for phosphazenes, Computational and Theoretical Polymer Science, 8 (1998) 229-246.
[46] J. Cheng, J. Zhu, B. Liu, Molecular modeling investigation of adsorption of self-assembled peptide nanotube of cyclo-[(1R, 3S)-γ-Acc-d-Phe] 3 in CHCl 3, Chemical physics, 333 (2007) 105-111.
[47] J. Wijmans, R. Baker, The solution-diffusion model: a review, Journal of membrane science, 107 (1995) 1-21.
[48] S. Brunauer, L.S. Deming, W.E. Deming, E. Teller, On a theory of the van der Waals adsorption of gases, Journal of the American Chemical society, 62 (1940) 1723-1732.
[49] M.L. Zeidel, S.V. Ambudkar, B.L. Smith, P. Agre, Reconstitution of functional water channels in liposomes containing purified red cell CHIP28 protein, Biochemistry, 31 (1992) 7436-7440.

Chapter 3

Water transport and ion rejection investigation for application of cyclic peptide nanotubes to forward osmosis process: a simulation study

3.1. Introduction

As populations grow and climates change, water resources have escalated in importance. To meet the ever-increasing demand, desalination processes via membrane filtration technologies are being widely applied. Nevertheless, the requirements for drinking water have increased, which means the development of novel membranes that combine high levels of flux and solvents/particulate rejection is required in energy-saving processes. Aquaporin was isolated from the human kidney [1]. Aquaporin is a type of protein channel that simultaneously transports water rapidly while completely rejecting ions [2]. This excellent transport performance has obviously attracted the interest of scientists working in related fields, and attempts to embed "water channel" properties into membranes are now being developed. Kumar et al. successfully revealed Aquaporin-embedded lipid bilayer membranes that have outstanding water permeability [3]; other pioneering studies have shown these types of membranes to have water permeability that is as much as 100-fold that of common polymeric RO membranes [2, 4]. Even so, Aquaporin has drawbacks that include expensive acquisition and a complex molecular structure, which makes it difficult to produce on an

industrial scale. On the other hand, Gramicidin A (GA) is considered another candidate because of a relatively simple peptide structure that can form a nano-scale porous membrane with a lipid bilayer. Although GA has shown performance similar to Aquaporin in RO application [5, 6], GA is toxic, and must be treated cautiously, which limits the applications. Therefore, ways to develop inexpensive, stable and safe water channels with high levels of water flux remains an interesting theme.

Ideas for artificial water channels have been developed using carbon nanotubes [7-10], an I-quartet [11-13], and a macrocycle 4 [14-16]. These form nano-scale porous materials with a lipid bilayer, and show properties similar to Aquaporin that are less expensive. With the successes of these pioneer studies, artificial water channels are expected to herald a new generation in desalination membranes. In this study, cyclic peptide nanotubes (CPNTs) were studied as another candidate for an artificial water channel. CPNTs are a type of organic nanotube that is formed through self-assembly of hydrophobic side chains that can be placed into a lipid bilayer to form a specific nanoporous structure that forms a biological membrane with high biocompatibility [17-19]. Therefore, CPNTs are a candidate for the biomimetic material that is used in artificial water channels. In addition, membranes with these types of water channel properties are expected to be applicable to forward osmosis (FO) filtration [20-24]. A biomimetic water channel with high levels of water flux, high levels of solvent rejection, and energy savings, would be a novel membrane material.

In the development of novel materials, it is necessary to study the characteristics on a molecular scale. Microscopic information such as interaction energy between materials and

water-transport mechanisms is helpful in material development. Many pioneering simulation studies in the construction of water channels are available to assist in this type of experimental work. Water permeability, transport mechanisms, and selectivity of Aquaporin channels have been discussed in the development of natural water channels [25-29] . GA channel simulation has been explored using molecular dynamic simulations and Monte Carlo methods [30-34]. For artificial water channels, carbon nanotubes have been widely investigated via theoretical studies [35-40]. The structural characteristics and predictions for water transport performance based on solution-diffusion models for different types of CPNTs were presented in our previous work [41]. The above studies have provided much useful information that would have been difficult to obtain from actual experimental work, and the results agree well with those from experimental data.

In this study, three types of CPNTs were adopted in FO filtration simulation. First, the performance of water molecular transport with different types of CPNTs was simulated using MD techniques. Second, the interaction energy of water molecules entering CPNTs and water permeabilities were discussed to elucidate the transport mechanisms for different types of CPNTs in the FO process. Finally, an ion with a hydrated structure was placed into a nanotube to study the rejection mechanism. Selectivity was discussed according to the relative mobility between water molecules and ions via mean square displacement (MSD) analysis. The potential charge distribution in cyclic peptide cages was used to illustrate the ion rejection mechanism.

3.2. Simulation method

This study used a forward osmosis (FO) simulation model to examine the water permeability performance and ion rejection ability of CPNTs. Three types of CPNT molecular models, 8CP, Mba-8CP, and 4Mba-8CP, were created based on the MD simulation procedures that were used to observe the FO calculation process. Furthermore, predictive water permeabilities and ion rejection were examined. All molecular models were constructed using BIOVIA Materials Studio® commercial software. The model construction, simulation parameters, and physical property estimations are discussed in the following sections.

3.2.1. Cyclic peptide nanotube molecular model

From our previous study [41], shown in Fig.3.1, three types of CPNTs were adopted in this FO process simulation work. Common 8CP via the tailoring of cyclo-[L-Lys-D-Ala-L-Leu-D-Ala]$_2$, Mba modified cyclic peptide, and cyclo-[L-Lys-D-Ala-L-Leu-D-Ala-L-Lys-D-Ala-γ-Mba-D-Ala] (Mba-8CP) was constructed by replacing the L-Lys with a single aromatic amino acid (γ-Mba-OH). Based on a similar procedure, a modified 4Mba-8CP was constructed using four aromatic amino acid functional groups to replace the original two L-Lysines and two L-Leucines. In this work, each CP subunit model was built via an Amorphous Cell module of the BIOVIA Materials Studio® software. These cyclic peptides were then used as subunits and were stacked eight times to form CP nanotube models. The dimensional and structural properties of these three models are shown in Table 3.1.

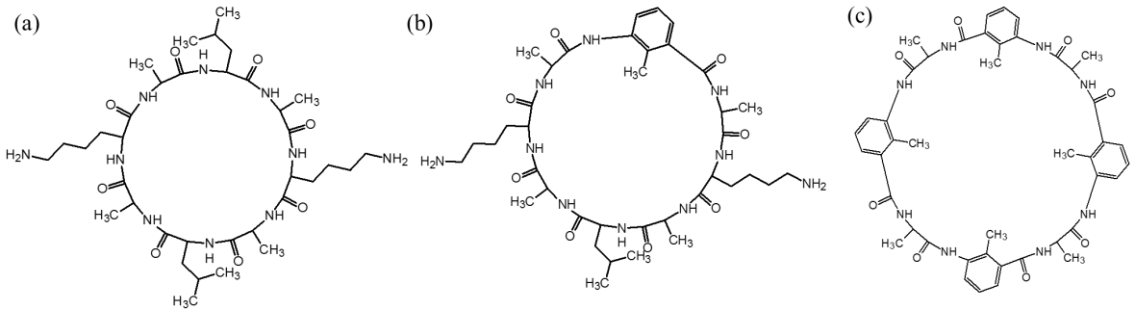

Fig.3.1 Chemical structures of (a) 8CP, (b) Mba-8CP, (c) 4Mba-8CP

Table 3.1 Details of the properties of cyclic peptide nanotube built in this study

	No. of atoms	Internal Diameter [Å]	Channel Volume [Å^3]
8CP	960	10.3	1320
Mba-8CP	944	7.15	1460
4Mba-8CP	928	8.3	1970

First, Geometry Optimization was introduced to optimize the energy of the model structure. In this process, energy calculation and changes in the structures of 5,000 iterations were carried out to establish each of the sensible initial nanotube structures. Afterward, a MD duration with an NVT ensemble (fixed atom number, system volume, and temperature) at 298 K for 100 ps was applied to reach the molecular structures under an equilibrium state. Finally, the equilibrium structures were adopted for the structural characterization and analysis of water transport behavior. The details of the simulation procedures for preparing cyclic peptide nanotube (CPNT) models are described in the supplementary information. In this study, the Condensed-phase Optimized Molecular Potential for Atomistic Simulation

Studies (COMPASS) force field [42-44] was adopted to perform the energy minimization and MD calculation processes. The various functional forms in this force field are illustrated as follows:

$$
\begin{aligned}
E = & \sum_{b}\left[K_2(b-b_0)^2 + K_3(b-b_0)^3 + K_4(b-b_0)^4\right] \\
& \textbf{(a)} \\
& + \sum_{\theta}\left[H_2(\theta-\theta_0)^2 + H_3(\theta-\theta_0)^3 + H_4(\theta-\theta_0)^4\right] \\
& \textbf{(b)} \\
& + \sum_{\phi}\left\{V_1\left[1-\cos\left(\phi-\phi_1^0\right)\right] + V_2\left[1-\cos\left(2\phi-\phi_2^0\right)\right] + V_3\left[1-\cos\left(3\phi-\phi_3^0\right)\right]\right\} \\
& \textbf{(c)} \\
& + \sum_{x} K_x x^2 + \sum_{b}\sum_{b'} F_{bb'}(b-b_0)(b'-b'_0) + \sum_{\theta}\sum_{\theta'} F_{\theta\theta'}(\theta-\theta_0)(\theta'-\theta'_0) \\
& \textbf{(d)} \qquad\qquad \textbf{(e)} \qquad\qquad \textbf{(f)} \\
& + \sum_{b}\sum_{\theta} F_{b\theta}(b-b_0)(\theta-\theta_0) + \sum_{b}\sum_{\phi}(b-b_0)\left[V_1\cos\phi + V_2\cos 2\phi + V_3\cos 3\phi\right] \\
& \textbf{(g)} \qquad\qquad\qquad\qquad \textbf{(h)} \\
& + \sum_{b'}\sum_{\phi}(b'-b'_0)\left[V_1\cos\phi + V_2\cos 2\phi + V_3\cos 3\phi\right] \\
& \textbf{(i)} \\
& + \sum_{\phi}\sum_{\theta}\sum_{\theta'} K_{\phi\theta\theta'}\cos\phi(\theta-\theta_0)(\theta'-\theta'_0) + \sum_{i>j}\frac{q_i q_j}{\varepsilon r_{ij}} + \sum_{i>j}\left[\frac{A_{ij}}{r_{ij}^9} - \frac{B_{ij}}{r_{ij}^6}\right] \qquad (3.1) \\
& \textbf{(j)} \qquad\qquad \textbf{(k)} \qquad \textbf{(l)}
\end{aligned}
$$

The energy terms are composed of three categories: bonded energy terms, cross-interaction terms, and non-bonded energy terms. The bonded energy terms include (a) the covalent bond-stretching energy terms, (b) the bond-angle bending energy terms, and (c) the torsion-angle rotation energy terms. The designation (d) is either the out-of-plane energy or an improper term. The terms for cross-interaction consist of the dynamic variations among bond stretching, bending, and torsion angle rotation interactions ((e)–(j)). The non-bonded energy terms, (k)

and (l), represent the Coulombic electrostatic interaction force and the van der Waals (vdW) potential force, respectively.

3.2.2. Molecular model of forward osmosis simulation

In order to set up the model for the FO simulation of water and solute conduction, the simulation model was divided into three parts. First, the CPNT filled with water molecules within the channel and was located in the middle of the simulation cell. The CPNT was set between two reservoirs. The reservoir on the left-hand side was filled with 400 molecules of pure water, and another reservoir on the right-hand side was filled with an ion aqueous solution of 12 Na^+, 12 Cl^- ion atoms, and 360 water molecules, which corresponded to a molarity concentration of about 1.71 M.

In order to simulate FO process filtration, as shown in Fig. 3.2, the periodic boundary conditions in the z-direction were cut off using two fixed graphene layers with size x and y directions of 20 Å. Each graphene layer played a role in avoiding interactions between the pure-water and seawater reservoirs [45]. This type of artificial water channel is surrounded mostly by lipid bilayers that form a biomimetic membrane. These systems, however, are too large for computer calculation. Therefore, in this work, instead of setting the lipid bilayer, some carbon atoms on CPNTs were fixed to reduce the computer calculation load. To permit the motions, rotations and vibrations of nanotube molecules, only approximately 5% of the nanotube atoms were pinned to fixed points in the center of the cell during the simulation period, which allowed a much more free response to water flowing situations by the nanotube structure. This structure allowed us to mimic the concentration-driven filtration process.

Generally, fixing a relatively small number of membrane atoms may slightly affect the water transport performance, but it does not cause enormous alterations in the transport mechanisms of a nanotube under molecular-scale operation [46], which was the central issue of this study.

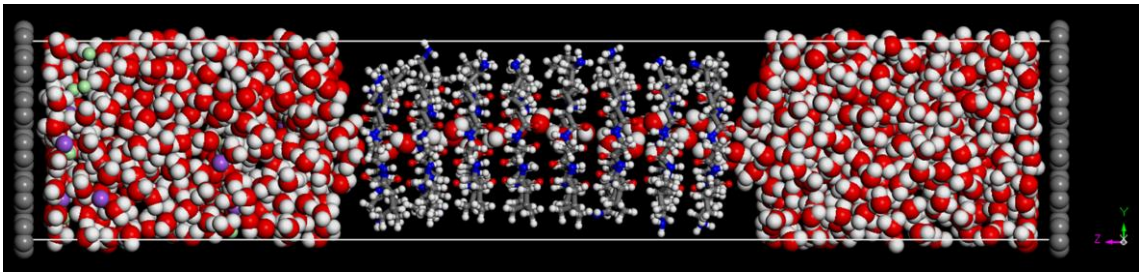

Fig.3.2 Forward osmosis filtration simulation model.

3.2.3. Physical property analysis

The aim of this study was to spell out the water-molecule transport behaviors and ion-rejection ability of different types of CPNTs in the FO process by applying MD simulation techniques. Details of the physical properties are described in this section.

3.2.3.1 Hydrated structure of Na^+ and Cl^- ions

In this work, the hydrated structure of ions was constructed and analyzed to validate the feasibility of the COMPASS force field to describe ion transport behavior. Validation was accomplished via a radial distribution function (RDF). The RDF expresses the relative number of water molecule around a distance, *r*, in a hydrated ion structure. The hydration number (coordination number) can be computed by integrating Eq. (3.2).

$$N_{water}^{ion}(r) = 4\pi\rho \int_0^{rmin} g_{O-ion}(r) r^2 dr \qquad (3.2)$$

where ρ is the bulk density of water and g(r) is the radial distribution function. Hydration numbers can be correlated with the size and mobility of ions and also used to illustrate the selectivity of CPNTs. These two values were calculated and compared with a previous reference [47] as an important part of the validation process.

3.2.3.2 Prediction of water permeability

During the calculation period, the number of water molecules within nanotubes for pure-water and seawater reservoirs were traced and recorded. Using these data, we obtained the time course curve of water molecules for three different divisions of the simulation model as a function of elapsed time via *NVT* MD simulations. The curves of the water molecules were analyzed to study the differences in the permeation behaviors of water molecules for each of the CPNT models. Osmotic pressure was considered as the driving force during the FO simulation period, which could be calculated from the Van't Hoff equation. The water permeability was predicted from the slope of the water molecules alteration curve using Eq. (3.3).

$$Permeability\ [mol\ m/(m^2 s\ Pa)] = \frac{\Delta N\ L}{A\ \Delta t\ \Delta\pi N_A} \qquad (3.3)$$

where, ΔN [-] is the change in the number of molecules during a certain period Δt [s], and A [m^2] is the area of the cross section of CPNT, $\Delta\pi$ is the mean osmotic pressure during Δt, N_A [mol^{-1}] is Avogadro's number, and L [m] is the channel length. 25 water molecules were inserted into a nanotube in the initial state as a hydrated water channel and a 10-ns calculation

period was provided to obtain diagrams for the time course of the number of water molecules. The details of the calculation procedure are described in the supplementary information.

3.2.3.3 Ion rejection capability

Ion rejection ability is a critical issue in the desalination process. The permeation of ions was a concern that also was traced. In the seawater reservoir, 12 sodium ion atoms, 12 chlorine ion atoms, and 360 water molecules consisted of a solute portion corresponding to a molarity concentration of about 1.71 M. During the calculation process, the diffusion behavior of ions can be observed. In other words, the ion rejection ability of CPNTs can be gauged according to the number of ion atoms that permeate. Also, the ability of CPNTs to repulse ions can be discussed by analyzing the relative displacement of water molecules and ions within each of the different types of simulation nanotube models. The hydrated ions were straight put into nanotube and the displacement and trajectory were recorded as MSD distribution for the analysis.

3.2.3.4 Partial charge distribution

In order to illustrate the ion rejection mechanisms among the three types of CPNTs. Partial charge distribution was introduced to explain the interaction between a cyclic peptide cage and the hydrated structure of an ion. Details of the theory of partial charge distribution calculation are shown in the supplementary information.

3.3 Results and discussion

3.3.1. Ion model validation

The feasibility, structural characteristics, and transport performance of CPNTs were validated and discussed in our previous study [41]. Therefore, in this work, the validation procedure was focused on the hydrated structure of seawater, as shown in Fig. 3.3. To confirm the hydrated structure, a reservoir of seawater was constructed that consisted of sodium ions, chlorine ions, and water molecules. After MD calculation using an NVT ensemble, the hydrated structure of sodium and chlorine ions under an equilibrium state was analyzed. The hydration number and hydration radius were calculated and compared with the results from a previous study [47] to validate whether the COMPASS force field had truly described the ion hydrated structure or not.

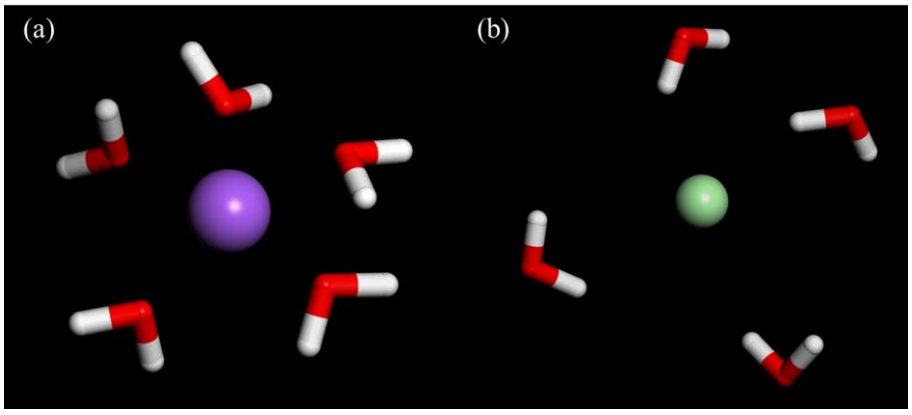

Fig.3.3 Hydration structure of (a) sodium, and (b) chlorine ion.

The first hydration layer of an ion can be analyzed via the radial distribution function between an ion and water molecules. The radial distribution function, $g(r)$, indicates the relative number of water molecules that surround a given distance, r, from an ion. As shown

in Fig. 3.4(a), the first peak in the O-Na^+ distribution was located at approximately 2.3 Å and the second peak was around 4.6 Å. In the case of Cl^-, the first peak in the O-Cl^- distribution was located at approximately 3.4 Å, and no significant second peak was shown. These results indicated that water molecules formed the first hydration shell to a length of approximately 2.5 Å for Na^+ and about 3.5 Å for Cl^-. Furthermore, the hydration numbers (coordination numbers) could be calculated. The hydration numbers reveal the number of water molecules within the first hydration shell. The hydration number for Na^+ was approximately 6 and that for Cl^- was about 7.5, as shown in Fig. 3.4(b). The values of the hydration radius and coordination numbers showed good agreement with the results from a previous study [47] and are listed in Table 3.2. We concluded that the COMPASS force field was suitable for this calculation. After validation, we noticed the hydrated structure was larger than the channel diameter of the 2Mba-8CP nanotube model reported in our previous study [41]. Therefore, only three types of nanotubes, 8CP, Mba-8CP, and 4Mba-8CP, were adopted in this work.

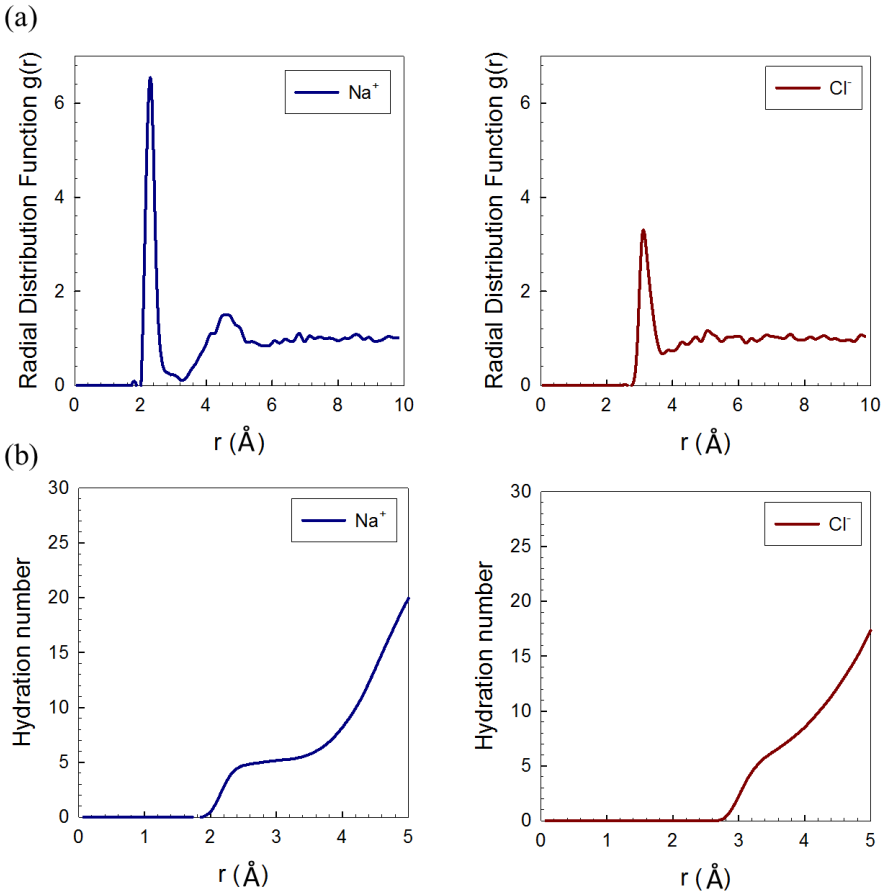

Fig.3.4 (a) Radial distribution functional (RDF) and (b) hydration number of sodium and chlorine ion.

Table 3.2 Comparison of the hydration structure properties

		Ref. [48]	This work
Na^+	Hydration radius [Å]	2~4	2.3
	Hydration numbers	5.6	6
Cl^-	Hydration radius [Å]	2~3	3.4
	Hydration numbers	6.5	7.5

3.3.2. Interaction energy analysis

The interaction between a water molecule and the nanotube it enters is a critical property in the FO filtration process, and, therefore, the quantized interaction energies between water molecules and nanotube entrance (first cyclic peptide cage) were calculated and are compared in Fig. 3.5(a). The observed interaction energies were clustered around the mean values at different levels of deviation. In terms of interaction energy, 4Mba-8CP exhibited the highest level of repulsive energy (positive) because of the largest number of hydrophobic functional groups. On the other hand, there was not a significant energy difference between 8CP and Mba-8CP, but a higher level of deviation was observed in the 8CP nanotube. A greater amount of water molecules in the first cage of the cyclic peptide could have contributed to this phenomenon. The gathering of water molecules around the entrance reflected an attractive force (negative) because of the hydrophilicity of the 8CP nanotube. When water molecules passed through and stayed in the same plane as the cyclic peptide cage, a high repulsive force (positive) was created by the hydrophobic nature of its backbone carbon chain.

The interaction energy was further examined via van der Waals (vdW) and Coulombic energy comparison. As shown in Fig. 3.5(b), the vdW energy was affected by the hydrophobic functional groups that were used to modify the CPNTs. The 4Mba-8CP version showed the highest value, which indicated that the four protruding γ-Mba-OH functional groups had strongly repulsed the water molecules at the entrance. The 8CP and Mba-8CP versions showed lower values because there was no, or only one, modified hydrophobic

functional group. These three types of CPNTs all showed a certain level of repulsive force because the carbon atoms that form the nanotube backbone easily repulsed the water molecules during the simulation process.

The values for Coulombic energy are shown in Fig. 3.5(c). All of the simulation models showed an attractive force (negative) in this analysis. The carbonyl functional groups of the cyclic peptide cage would have contributed to this phenomenon. An unexpected result was observed, however, for the 4Mba-8CP nanotube. Despite the fact that the 4Mba-8CP was the most hydrophobic nanotube of the three simulation models, it nonetheless showed the strongest attractive force. This could have been due to the hydrophobicity of the nanotube and water molecules gathering around the entrance instead of being conducted inside. With this condition, the distance between carbonyl functional groups and water molecules is extremely close, which causes a strong attractive force. To the contrary, the repulsive force of the 4Mba-8CP nanotube was strong enough to overcome the attractive force, which agrees well with the interaction energy analysis shown in Fig. 3.5(a).

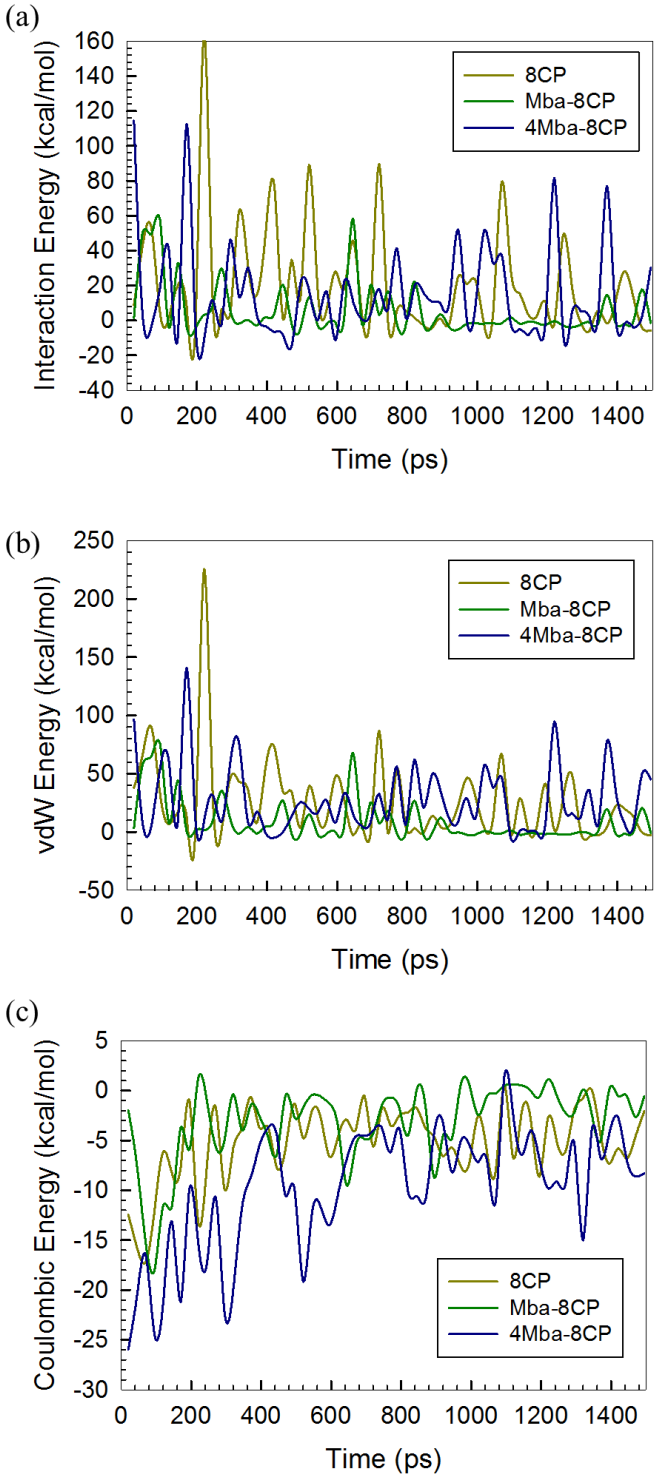

Fig.3.5 Time course of (a) interaction energy, (b) vdW energy and (c) coulombic energy between water molecules and a first cyclic peptide cage (entrance of nanotube) under an equilibrated state during NVT simulations.

3.3.3. Water permeability calculation

The FO filtration process was used to calculate the water permeabilities via alteration of the number of water molecules in the simulation reservoir. This research compared the transport behavior and ion rejection ability of water molecules within three types of CPNTs.

(a) 8CP nanotube: As shown in Fig. 3.6(a). The simulation process transported water molecules from the seawater side to the pure-water side, and the number of water molecules within the pure-water reservoir increased while the number in the seawater reservoir decreased until the simulation system reached a state of equilibrium. The amount of water molecules inside the nanotube stayed nearly constant at approximately the initial number. As shown in Fig. 3.6(b), the number of water molecules dramatically changed after the calculation was started, then the slope gradually stabilized until it reached a state of equilibrium at approximately 3,000 ps. Based on this tendency, the alteration of the slope was used to predict water permeability. A rough comparison between the slope of pure water and that of seawater showed a similar tendency, which explains the validity of this simulation method and the feasibility of comparing other types of modification nanotubes. The value of predicting water permeability from the slope of the curve was 1.8×10^{-11} (mole m s^{-1} m^{-2} Pa^{-1}).

For comparison, the experimentally estimated water flux of a commercial RO membrane (polyamide membrane) was introduced around 2 (L m^{-2} h^{-1} bar^{-1}), which is equivalent to 3×10^{-7} (mole m^{-2} s^{-1} Pa^{-1}) [48]. Also, some commercial RO membranes with chemical treatment for using in FO, the water permeability performance showed around 2 ~ 45 (L m^{-2}

h^{-1} bar^{-1}), which is equivalent to $3 \times 10^{-7} \sim 6.8 \times 10^{-6}$ (mole m^{-2} s^{-1} Pa^{-1}) [49]. For a novel CPNT material, a channel should be embedded into a lipid bilayer to form a biomimetic membrane with a porosity of 1%. Based on this assumption, the water permeance of 8CP could be calculated to an approximate value of 4.5×10^{-5} (mole m^{-2} s^{-1} Pa^{-1}). As a result, we would expect this membrane to show an approximately 100-fold higher water permeance performance than a commercial RO polyamide membrane, even, 10-fold higher than the membrane after chemical treatment for improving the performance.

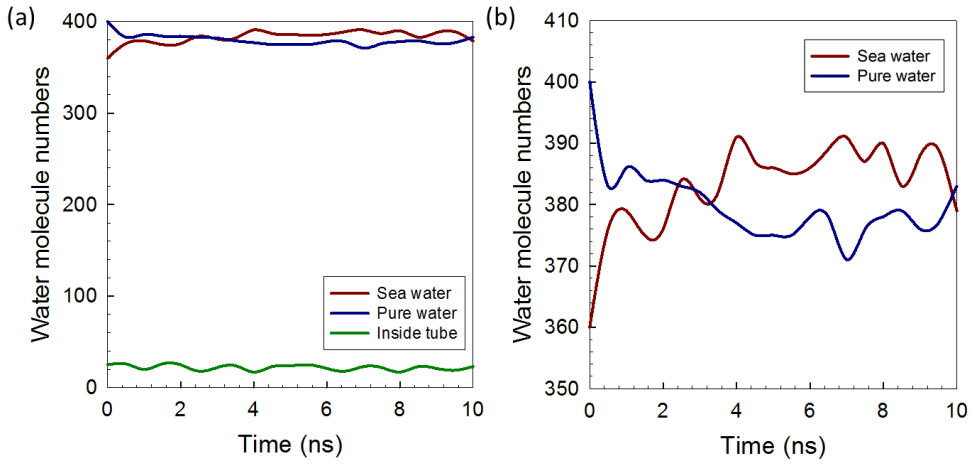

Fig.3.6 Time course of water molecules number during FO simulation with 8CP nanotube. Fig.3.6 (b) has the enlarged vertical axis. Data are the same as those shown in Fig.3.6 (a).

(b) Mba-8CP nanotube: The number of water molecules in 8CP showed a similar tendency toward variation, as shown in Fig. 3.7. The number of water molecules changed in the two different reservoirs but the amounts remained constant in the nanotube. However, the variation period was a bit longer for Mba-8CP, as shown in Fig. 3.7(b). As mentioned in our previous study [41], the Mba-8CP nanotube was modified by a hydrophobic functional group.

This hydrophobic functional group at the entrance made it difficult for water molecules to enter the nanotube, which resulted in a longer transport period. In comparing the results with those of 8CP, the same duration of time of 3,000 ps, was adopted when calculating the water permeability. The value predicted from the slopes of the pure-water and seawater curves was about 1.4×10^{-11} (mole m s^{-1} m^{-2} Pa^{-1}). The value of the water permeability for the modified Mba-8CP was a little bit lower than the value of the 8CP nanotube. In our previous study [41], water molecules diffusion was analyzed under adsorption equilibrium state via solution-diffusion model, which illustrated that a hydrophobic functional group can dramatically enhance the water mobility within a nanotube. However, when we consider the interfacial phenomenon caused by the repulsive interaction at the entrance, there would be a resistance to the transportation of water molecules into a nanotube. Therefore, the modified Mba-8CP showed a slightly lower level of water permeability performance compared with that of common 8CP, even though the permeability remained excellent.

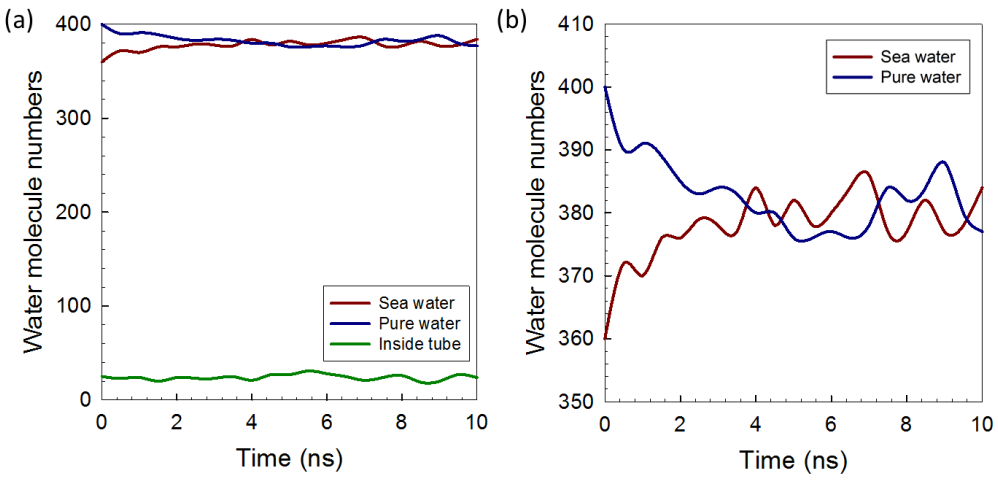

Fig.3.7 Time course of water molecules number during FO simulation with Mba-8CP nanotube. Fig.3.7 (b) has the enlarged vertical axis. Data are the same as those shown in Fig.3.7 (a).

(c) 4Mba-8CP nanotube: 4Mba-8CP was the most hydrophobic nanotube of the three types of simulation models, and demonstrated unique performance in altering the number of water molecules. As Fig, 3.8(a) shows, this version differed from the 8CP and Mba-8CP nanotubes, in that the number of water molecules within the nanotube and seawater reservoir changed but the number in the pure-water reservoir remained constant. This phenomenon reflected the hydrophobicity of this nanotube. Water molecules were transported rapidly within the nanotube to the seawater reservoir, but water molecules could not enter the nanotube from the pure-water reservoir because of the effect of the modified hydrophobic functional groups. The permeability of 4Mba-8CP seemed to be the highest among the three types of nanotubes based on the slope of seawater, as shown in Fig. 3.8(b), but this transport behavior was aided by the hydrophobicity of the nanotube rather than by concentration-driven conduction. Therefore, we could not compare the water permeability of 4Mba-8CP

with that of the other two types of CPNTs in this work. The 4Mba-8CP channel had high hydrophobicity and seemed unsuitable for the FO process.

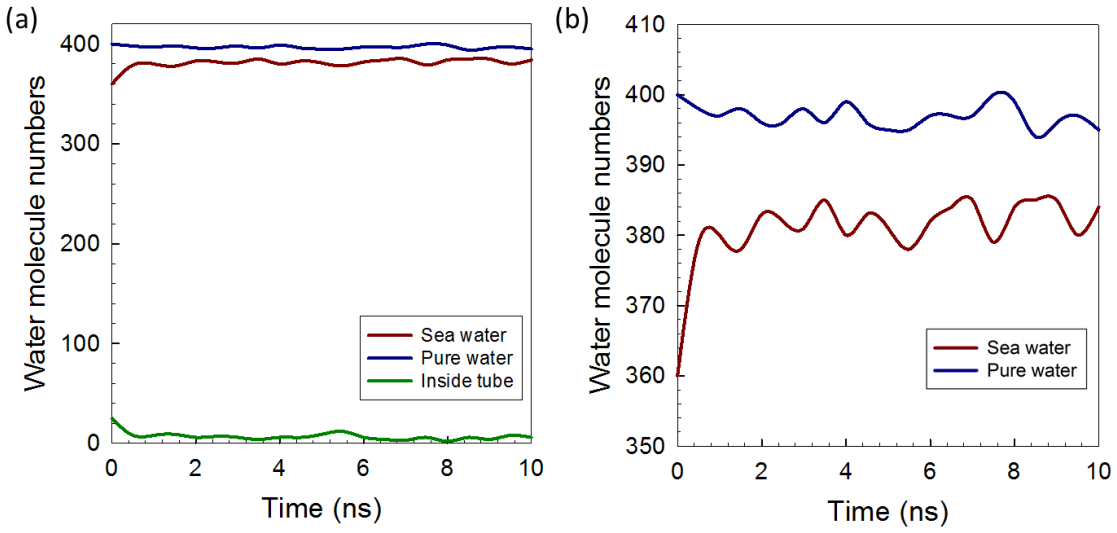

Fig. 3.8 Time course of water molecules number during FO simulation with 4Mba-8CP nanotube. Fig.3.8 (b) has the enlarged vertical axis. Data are the same with Fig.3.8 (a).

3.3.4. Ion transport behaviors

In the last section, we compared the water permeability of three types of CPNTs by using the concentration-driven FO filtration simulation process. We found no ion transport in the three types of nanotubes simulation models during a 10-ns calculation period. This high ion rejection ability attracted our interest. In order to understand how the CPNTs reject ion atoms, and the selectivity between water molecules and ion atoms, a longer simulation period would be necessary, but would have the drawback of requiring an exorbitant calculation load and an extensive amount of simulation time. Fortunately, a previous study [50] provided discussion on this topic. In that pioneer study, after a 50 ns-long simulation period, the

negative ions (Cl^-) were 100% rejected by the contribution from carbonyl functional groups at the entrance. These results agreed well with the partial charge distribution analysis shown in Fig. 3.9.

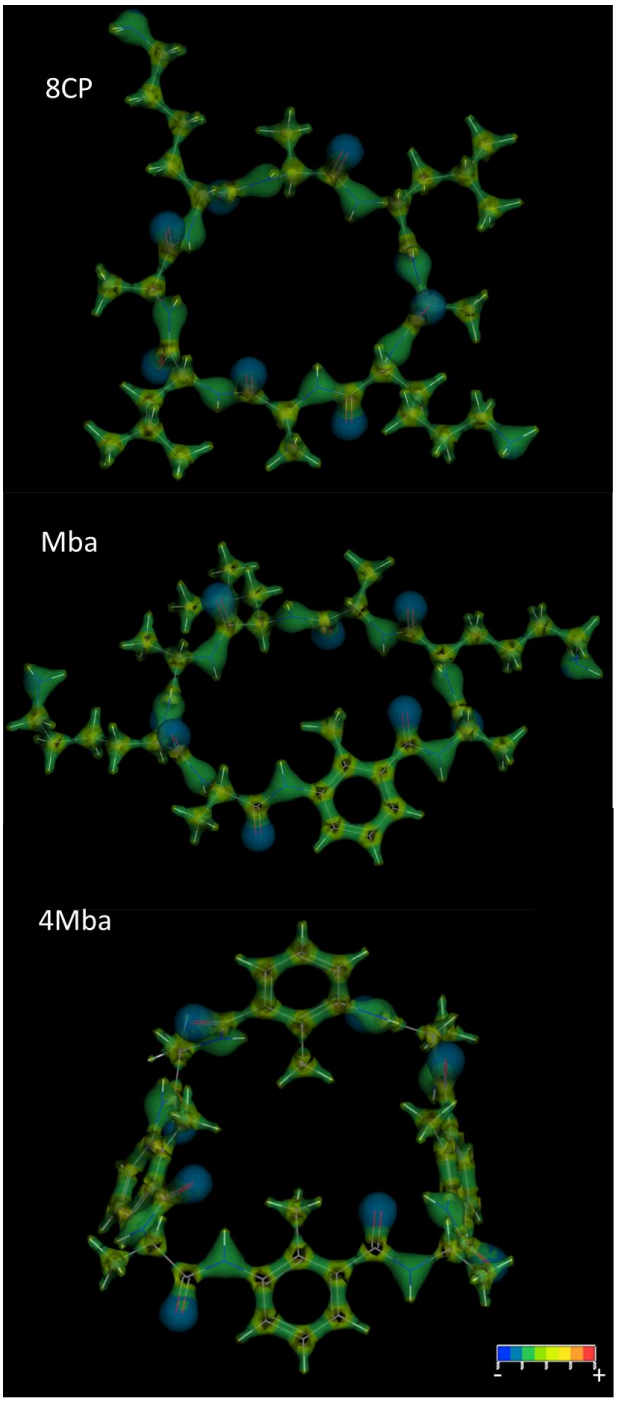

Fig.3.9 Partial charge distribution of (a) 8CP, (b) Mba-8CP and (c) 4Mba-8CP subunit.

Based on the distribution of the different colors, we concluded there was effective electronegative distribution around the carbonyl functional groups in the cyclic peptide cage. Like charges repel one another, and the electronegative distribution at the entrance promoted the repulsion of Cl^- ions during the calculation period. On the other hand, Na^+ ions were attracted and entered the nanotube with a certain level of external force. Therefore, we inserted a hydration structure composed of Na^+ into the CPNT simulation models for a 500-ps simulation period to understand the ion rejection mechanism of CPNTs via the use of MSD analysis. The results are shown in Fig. 3.10. We observed a high level of selectivity in all types of CPNT simulation models. In the 8CP and Mba-8CP simulation models, the MSD of the water molecules agreed well with the results found in our previous study [41], which showed that the hydrophobic functional groups definitely enhanced the mobility of the water molecules within the nanotube. Meanwhile, the relatively lower displacement of Na^+ shown in Fig.3.10 (a) and (b) can be explained by the potential charge distribution shown in Fig. 3.9. There are two positions where Na^+ ions reside within a nanotube: either between the two cyclic peptide cages or in the plane of the cyclic peptide cage. When Na^+ ions were present in the plane of the cage, cations were repulsed by the carbon backbone. When, however, cations were located between the two cages, they were attracted by the carbonyl functional groups. Simply put, cations were trapped in the cyclic peptide cages in most instances when they existed in the CPNTs, and this phenomenon was reflected by the low displacement in the MSD calculation. Some unexpected results were observed in the 4Mba-8CP simulation model shown in Fig. 3.10 (c). The displacement of water molecules was relatively higher than that of Na^+ ions but much lower than the results found in our previous study [41].

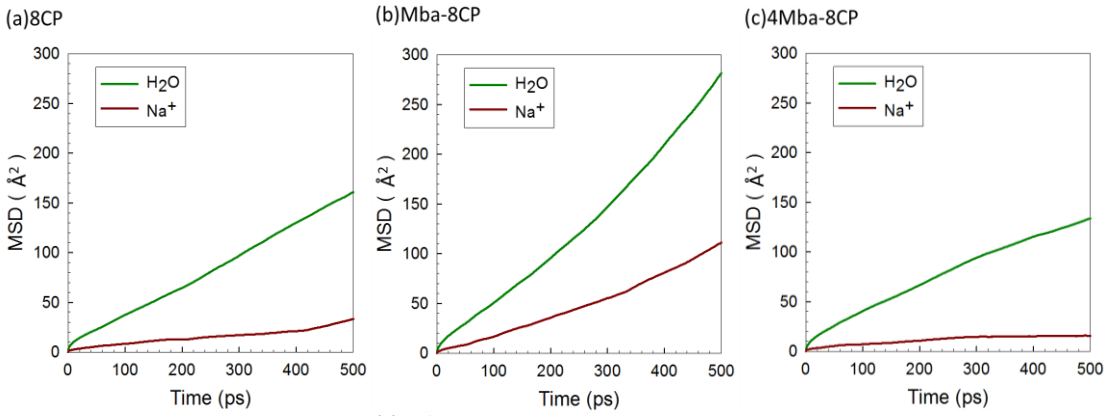

Fig. 3.10 Relative displacement between water molecules and sodium ion within (a) 8CP, (b) Mba-8CP and (c) 4Mba-8CP.

That result was caused by the huge hydration structure of Na^+ located within the 4Mba-8CP simulation model, as the hydrophobicity of the hydrophobic nanotube created a hydration structure that was too strong to be destroyed. The gigantic bulk of the hydration structure reduced the relatively mobility of water and caused its displacement in the 4Mba-8CP simulation model. Furthermore, since both the mobility of water molecules and Na^+ ions can be adjusted according to the presence of hydrophobic functional groups, the different modification levels showed varied transport performances, as illustrated in Fig. 3.11. This means that when one hydrophobic functional group is introduced, both the water and Na^+ displacement increase, while more introduction of functional group leads to the decrease in both the water and Na^+ displacement. This tunable transport performance reflects the high potential of CPNTs for applications to the separation process.

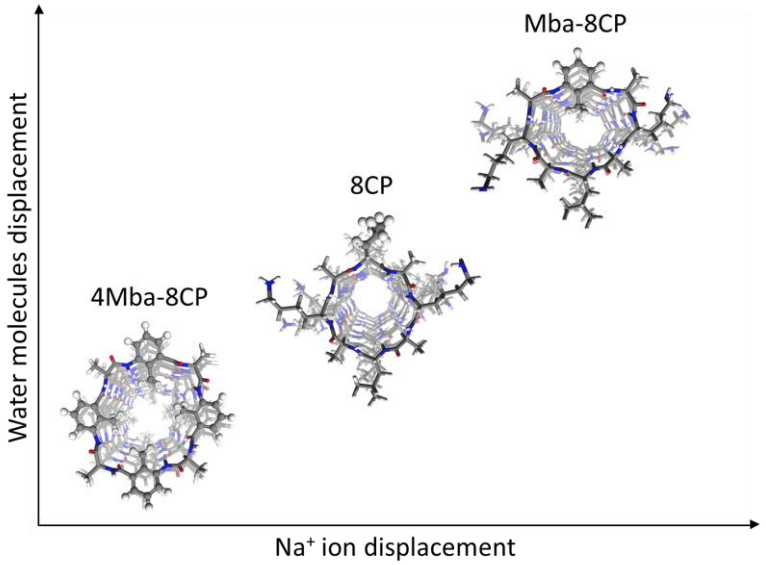

Fig.3.11 Trends of displacements of water molecules and Na^+ ion inside three types of nanotubes at 500 ps NVT calculation.

3.4. Conclusions

The concentration-driven transport behaviors of water and salt molecules were investigated via MD simulation of the FO filtration process for three types of CPNT models. The feasibility and structural properties of CPNTs were discussed in our previous study [41], , and the hydration structures of Na^+ and Cl^- were validated for the feasibility of an applied force field via RDF distribution (between ion and water molecules) and hydration levels. In order to characterize the interaction between nanotube entrance and water molecules, the interaction energy analysis including vdW and coulombic energy were presented. The concentration-driven FO simulation model consisted of two reservoirs containing pure water and seawater ($wt\% = 10\%$), and was performed using three types of CPNTs over a calculation period of 10 ns. Significantly different results were found between these three

types of CPNTs, which suggested that the presence of modified hydrophobic functional groups was effective. The combined results of the interactive energy and FO simulation demonstrated that carbonyl functional groups in cyclic peptide cages easily attract water molecules. In contrast, the hydrophobic γ-Mba functional groups in the modified Mba-8CP and 4Mba-8CP repulsed water molecules, which made it difficult for water molecules to enter the nanotube. As a result, we found that the presence of hydrophobic functional groups make it difficult for water molecules to enter nanotubes in a FO process, but significantly enhances water mobility within a nanotube [41]. On the other hand, no ion transport was found in these three types of CPNTs. This performance is impressive since a high level of ion rejection is a critical asset in desalination processes. Therefore, in order to reduce the calculation load and simulation time, a hydration structure that consisted of sodium ions was inserted directly into a nanotube for ion selectivity analysis via MSD calculation. Selectivity was gauged by the relative displacement between water molecules and sodium ions. All three types of simulation nanotubes used in this work showed high selectivity. The mobility of ions within the nanotube was much lower than that of water molecules, and the partial charge distributions of the three types of cyclic peptide cages could provide an explanation. Cations were trapped within CPNTs due to the carbon backbone, and this led to a relatively low displacement of cations.

Based on the results of this work, hydrophobic γ-Mba functional groups within modified nanotubes not only altered the mobility of water molecules but also adjusted the movement of cations. The selectively between water molecules and cations can be easily adjusted via modification of the functional groups. This feature reflected the high potential for multiple

applications of CPNTs, because the performance can be modified to meet separation requirements. Nanotubes that consist of cyclic peptides with different numbers, or varied types, of functional groups have the potential to be used in the construction of artificial water channels. Although molecular simulation provided unique opportunities for examination at the molecular level in the investigation of these three types of CPNTs, the simulation model was still need to improve. The simulation time was limited by the simulation model, because of the total number of molecules were constant, the osmotic pressure decreased with the simulation time decreasing. Therefore, it was difficult to obtain the ion rejection performance and long-time calculation result via this model. Even so, this study shows that computational simulation paired with analytical methods at the microscopic level can be a helpful and reliable tool in the design and development of novel materials for biomimetic membranes.

3.5 References

[1] P. Agre, The aquaporin water channels, Proceedings of the American Thoracic Society, 3 (2006) 5-13.
[2] P. Pohl, S.M. Saparov, M.J. Borgnia, P. Agre, Highly selective water channel activity measured by voltage clamp: analysis of planar lipid bilayers reconstituted with purified AqpZ, Proceedings of the National Academy of Sciences, 98 (2001) 9624-9629.
[3] M. Kumar, M. Grzelakowski, J. Zilles, M. Clark, W. Meier, Highly permeable polymeric membranes based on the incorporation of the functional water channel protein Aquaporin Z, Proceedings of the National Academy of Sciences, 104 (2007) 20719-20724.
[4] M.Ø. Jensen, O.G. Mouritsen, Single-channel water permeabilities of Escherichia coli aquaporins AqpZ and GlpF, Biophysical journal, 90 (2006) 2270-2284.
[5] P.A. Rosenberg, A. Finkelstein, Water permeability of gramicidin A-treated lipid bilayer membranes, The Journal of general physiology, 72 (1978) 341-350.
[6] D. Saeki, T. Yamashita, A. Fujii, H. Matsuyama, Reverse osmosis membranes based on a supported lipid bilayer with gramicidin A water channels, Desalination, 375 (2015) 48-53.
[7] L. Brunet, D.Y. Lyon, K. Zodrow, J.-C. Rouch, B. Caussat, P. Serp, J.-C. Remigy, M.R. Wiesner, P.J. Alvarez, Properties of membranes containing semi-dispersed carbon nanotubes, Environmental Engineering Science, 25 (2008) 565-576.
[8] E. Celik, H. Park, H. Choi, H. Choi, Carbon nanotube blended polyethersulfone membranes for fouling control in water treatment, Water research, 45 (2011) 274-282.

[9] J.-H. Choi, J. Jegal, W.-N. Kim, Fabrication and characterization of multi-walled carbon nanotubes/polymer blend membranes, Journal of Membrane Science, 284 (2006) 406-415.
[10] S. Kim, J.R. Jinschek, H. Chen, D.S. Sholl, E. Marand, Scalable fabrication of carbon nanotube/polymer nanocomposite membranes for high flux gas transport, Nano letters, 7 (2007) 2806-2811.
[11] Y. Le Duc, M. Michau, A. Gilles, V. Gence, Y.M. Legrand, A. van der Lee, S. Tingry, M. Barboiu, Imidazole‐Quartet Water and Proton Dipolar Channels, Angewandte Chemie International Edition, 50 (2011) 11366-11372.
[12] E. Licsandru, I. Kocsis, Y.-x. Shen, S. Murail, Y.-M. Legrand, A. Van Der Lee, D. Tsai, M. Baaden, M. Kumar, M. Barboiu, Salt-excluding artificial water channels exhibiting enhanced dipolar water and proton translocation, Journal of the American Chemical Society, 138 (2016) 5403-5409.
[13] Y.-x. Shen, W. Si, M. Erbakan, K. Decker, R. De Zorzi, P.O. Saboe, Y.J. Kang, S. Majd, P.J. Butler, T. Walz, Highly permeable artificial water channels that can self-assemble into two-dimensional arrays, Proceedings of the National Academy of Sciences, 112 (2015) 9810-9815.
[14] X. Li, K. Yang, J. Su, H. Guo, Water transport through a transmembrane channel formed by arylene ethynylene macrocycles, RSC Advances, 4 (2014) 3245-3252.
[15] K. Ono, K. Tsukamoto, R. Hosokawa, M. Kato, M. Suganuma, M. Tomura, K. Sako, K. Taga, K. Saito, A Linear Chain of Water Molecules Accommodated in a Macrocyclic Nanotube Channel, Nano letters, 9 (2008) 122-125.
[16] D. Pasini, The click reaction as an efficient tool for the construction of macrocyclic structures, Molecules, 18 (2013) 9512-9530.
[17] S. Fernandez-Lopez, H.-S. Kim, E.C. Choi, M. Delgado, J.R. Granja, A. Khasanov, K. Kraehenbuehl, G. Long, D.A. Weinberger, K.M. Wilcoxen, Antibacterial agents based on the cyclic D, L-α-peptide architecture, Nature, 412 (2001) 452-455.
[18] M.R. Ghadiri, J.R. Granja, R.A. Milligan, D.E. McRee, N. Khazanovich, Self-assembling organic nanotubes based on a cyclic peptide architecture, Nature, 366 (1993) 324-327.
[19] W.S. Horne, C.M. Wiethoff, C. Cui, K.M. Wilcoxen, M. Amorin, M.R. Ghadiri, G.R. Nemerow, Antiviral cyclic d, l-α-peptides: Targeting a general biochemical pathway in virus infections, Bioorganic & medicinal chemistry, 13 (2005) 5145-5153.
[20] W. Ding, J. Cai, Z. Yu, Q. Wang, Z. Xu, Z. Wang, C. Gao, Fabrication of an aquaporin-based forward osmosis membrane through covalent bonding of a lipid bilayer to a microporous support, Journal of Materials Chemistry A, 3 (2015) 20118-20126.
[21] H.T. Madsen, N. Bajraktari, C. Hélix-Nielsen, B. Van der Bruggen, E.G. Søgaard, Use of biomimetic forward osmosis membrane for trace organics removal, Journal of Membrane Science, 476 (2015) 469-474.
[22] J. Parodi, M. Flynn, J. Romero-Mangado, O. Stefanson, R. Mancinelli, S. Trieu, B. Kawashima, Testing of synthetic biological membranes for forward osmosis applications, in, 46th International Conference on Environmental Systems, (2016) 1-11.
[23] C. Tang, Y. Zhao, R. Wang, C. Hélix-Nielsen, A. Fane, Desalination by biomimetic aquaporin membranes: Review of status and prospects, Desalination, 308 (2013) 34-40.
[24] S. Wang, J. Cai, W. Ding, Z. Xu, Z. Wang, Bio-inspired aquaporinz containing double-skinned forward osmosis membrane synthesized through layer-by-layer assembly, Membranes, 5 (2015) 369-384.
[25] B.L. de Groot, H. Grubmüller, Water permeation across biological membranes: mechanism and dynamics of aquaporin-1 and GlpF, Science, 294 (2001) 2353-2357.

[26] M. Hashido, A. Kidera, M. Ikeguchi, Water transport in aquaporins: osmotic permeability matrix analysis of molecular dynamics simulations, Biophysical journal, 93 (2007) 373-385.
[27] J.S. Hub, B.L. De Groot, Mechanism of selectivity in aquaporins and aquaglyceroporins, Proceedings of the National Academy of Sciences, 105 (2008) 1198-1203.
[28] D.F. Savage, P.F. Egea, Y. Robles-Colmenares, J.D. O'Connell III, R.M. Stroud, Architecture and selectivity in aquaporins: 2.5 Å X-ray structure of aquaporin Z, PLoS Biol, 1 (2003) 334-340.
[29] F. Zhu, E. Tajkhorshid, K. Schulten, Theory and simulation of water permeation in aquaporin-1, Biophysical Journal, 86 (2004) 50-57.
[30] K. Kim, D. Vercauteren, M. Welti, S. Chin, E. Clementi, Interaction of K+ ion with the solvated gramicidin A transmembrane channel, Biophysical journal, 47 (1985) 327-335.
[31] W. Lee, P.C. Jordan, Molecular dynamics simulation of cation motion in water-filled gramicidinlike pores, Biophysical journal, 46 (1984) 805-819.
[32] D. Mackay, P.H. Berens, K.R. Wilson, A. Hagler, Structure and dynamics of ion transport through gramicidin A, Biophysical journal, 46 (1984) 229-248.
[33] A. Skerra, J. Brickmann, Structure and dynamics of one-dimensional ionic solutions in biological transmembrane channels, Biophysical journal, 51 (1987) 969-976.
[34] A. Skerra, J. Brickmann, Simulation of voltage-driven hydrated cation transport through narrow transmembrane channels, Biophysical journal, 51 (1987) 977-983.
[35] T. Belytschko, S. Xiao, G. Schatz, R. Ruoff, Atomistic simulations of nanotube fracture, Physical Review B, 65 (2002) 235430_1-235430_8.
[36] G. Hummer, J.C. Rasaiah, J.P. Noworyta, Water conduction through the hydrophobic channel of a carbon nanotube, Nature, 414 (2001) 188-190.
[37] K. Koga, G. Gao, H. Tanaka, X.C. Zeng, Formation of ordered ice nanotubes inside carbon nanotubes, Nature, 412 (2001) 802-805.
[38] D.J. Mann, M.D. Halls, Water alignment and proton conduction inside carbon nanotubes, Physical review letters, 90 (2003) 195503_1-195503_4.
[39] A. Waghe, J.C. Rasaiah, G. Hummer, Filling and emptying kinetics of carbon nanotubes in water, The Journal of chemical physics, 117 (2002) 10789-10795.
[40] Z. Yao, C.-C. Zhu, M. Cheng, J. Liu, Mechanical properties of carbon nanotube by molecular dynamics simulation, Computational Materials Science, 22 (2001) 180-184.
[41] H.-C. Wu, T. Yoshioka, H. Nagasawa, M. Kanezashi, T. Tsuru, D. Saeki, H. Matsuyama, Preparation of cyclic peptide nanotube structures and molecular simulation of water adsorption and diffusion, Journal of Membrane Science, (2017) 101-110.
[42] D. Rigby, H. Sun, B. Eichinger, Computer simulations of poly (ethylene oxide): force field, pvt diagram and cyclization behaviour, Polymer International, 44 (1997) 311-330.
[43] H. Sun, COMPASS: an ab initio force-field optimized for condensed-phase applications overview with details on alkane and benzene compounds, The Journal of Physical Chemistry B, 102 (1998) 7338-7364.
[44] H. Sun, P. Ren, J. Fried, The COMPASS force field: parameterization and validation for phosphazenes, Computational and Theoretical Polymer Science, 8 (1998) 229-246.
[45] W. Gao, F. She, J. Zhang, L.F. Dumée, L. He, P.D. Hodgson, L. Kong, Understanding water and ion transport behaviour and permeability through poly (amide) thin film composite membrane, Journal of Membrane Science, 487 (2015) 32-39.

[46] M. Kotelyanskii, N. Wagner, M. Paulaitis, Molecular dynamics simulation study of the mechanisms of water diffusion in a hydrated, amorphous polyamide, Computational and Theoretical Polymer Science, 9 (1999) 301-306.
[47] B. Tansel, J. Sager, T. Rector, J. Garland, R.F. Strayer, L. Levine, M. Roberts, M. Hummerick, J. Bauer, Significance of hydrated radius and hydration shells on ionic permeability during nanofiltration in dead end and cross flow modes, Separation and Purification Technology, 51 (2006) 40-47.
[48] K.P. Lee, T.C. Arnot, D. Mattia, A review of reverse osmosis membrane materials for desalination—development to date and future potential, Journal of Membrane Science, 370 (2011) 1-22.
[49] X. Wang, E. Duitsman, N. Rajagopalan, V. Namboodiri, Chemical treatment of commercial reverse osmosis membranes for use in FO, Desalination, 319 (2013) 66-72.
[50] R. García-Fandiño, M. Amorín, L. Castedo, J.R. Granja, Transmembrane ion transport by self-assembling α, γ-peptide nanotubes, Chemical Science, 3 (2012) 3280-3285.

Chapter 4

Preparation of Amphotericin B-Ergosterol structures and molecular simulation of water adsorption and diffusion

4.1 Introduction

Membrane technology has been widely applied to water treatment, because it is highly effective and economic for the separation of solvents or particulates from water [1]. For instance, the membrane process is used in reverse osmosis (RO) to achieve water desalination and purification [2, 3]. As the human population increases, the amount of required and supplied water that utilizes membrane processing will continue to increase. Due to the increased requirement for water, the search for higher performance membranes for separation processes will result in ever-increasing interest among scientists.

Biomimetic materials have been intensively studied for modification of their properties to enhance separation performance [4-8]. In order to obtain improved water mobility, Kumar et al. introduced the idea of embedding the properties of aquaporin into membranes that show exceptional water permeability [9]. Aquaporin is a type of protein channel that was discovered in 2003 by Peter Agre [10]. Aquaporin is a porous protein that resides on cell membranes to function as a selective “water channel,” and is expected to be applied to high-performance water treatment processes. The techniques involved in these structural transport properties have been widely studied in experimentation [11-15] and simulation [16-20]. However, aquaporin is very expensive and difficult to produce on a large scale. Therefore,

artificial water channels using biomimetic materials have been widely studied and applied to water treatment membranes.

In recent decades, many specific materials have been considered as candidates for use as artificial water channels. For example, the structural properties and membrane performance of carbon nanotube (CNT) composite membranes were introduced in previous studies [21-24]. Cyclic peptide nanotubes (CPNTs) have been designed for insertion into biological processes, and their specific nanostructures have revealed a high level of biocompatibility properties [25-27]. Gramicidin A (GA) is an ion-selective channel that can be inserted into a lipid bilayer, and it has shown water permeability that is comparable to aquaporin [28-32]. Besides the experimental research, theoretical study on a microscopic scale is considered a favorable method for exploring the characteristics of novel materials. Many simulation studies have investigated artificial water channels. As shown below, the mechanical and transport properties of carbon nanotubes have been explored via theoretical study [33-37]. The Gramicidin A channel model has been studied via molecular mechanics, dynamics simulation, and Monte Carlo technique [38-42]. Some theoretical studies have also been introduced to reveal the properties of cyclic peptide and their potential in biomaterials [43-48]. The above studies have provided much useful information and have shown great agreement with the experimental data, which proves that molecular simulation is feasible as a method to design and analyze novel artificial water channels.

In this study, two models of Amphotericin B-Ergosterol (AmBEr) channels, single-layer channel (SLC) and double-layer channel (DLC), were constructed and explored. First, intermolecular and intramolecular properties were simulated via MD techniques. Second,

simulated hydrogen bonds and adsorption site snapshots were analyzed to reflect the affinity between water molecules and channel surfaces. Finally, MD techniques were used to explore water diffusion, and Monte Carlo (MC) simulation was introduced to study water sorption behaviors. All these analytical tools were used to study SLC and DLC AmBEr models in this work. Simulated permeability can be calculated via the values of diffusivity and solubility. Thus, the simulated permeabilities of different models can be compared to understand the transport mechanisms. Further, from previous studies, Amphotericin B was proved that it can enhance water transport performance in membrane separation process [49-52]. Therefore, this kind of artificial water channel had a high potential for designing next generation biomimetic membranes.

In short, the objective of this work was to use molecular simulation to evaluate the difference in structural properties and compare the performances of SLC and DLC AmBEr simulation models. The results showed similar structural characteristics but indicated slightly different transport mechanisms. The details are discussed in the following sections.

4.2. Simulation method

This study was focused on an Amphotericin B-Ergosterol (AmBEr) channel model, and included the construction, structures, adsorption, and transport behaviors of water molecules. The difference between the two forms of the AmBEr model, SLC and DLC, was also explored in this work. In order to analyze the characteristics of the AmBEr channel, both simulation models were created using the MD simulation procedure. Furthermore, three essential features of this work, channel structure, sorption and diffusion, were analyzed via

MD and MC simulation techniques. All these molecular models were constructed using BIOVIA Materials Studio® commercial software. The model construction, simulation parameters and physical property estimations are shown in the following sections.

4.2.1. Amphotericin B-Ergosterol Channel Molecular Model

Fig. 4.1(a) shows amphotericin B monomers consisting of three different segments: an amino sugar mycosamine (head of amphotericin B monomer), a rigid polyene chromophore with seven conjugated double bonds, and a flexible fragment on the opposite side with hydroxyl functional groups. Fig. 4.1(b) shows the chemical structure of ergosterol, which is simultaneously comprised of a hydrophobic portion and a hydrophilic hydroxyl group. Some specific atoms (C6, and O41 etc.) were adopted in following analyses, therefore, the atoms were numbered as shown in Fig.1 for easy understanding. This specific structure played an important role in stabilizing the AmBEr channel. Previous studies indicated that both SLC and DLC models are able to conduct water molecules [53]. The optimized structure of the single-layer AmBEr channel consists of eight amphotericin B chains and eight ergosterol monomers. Generally, an AmBEr channel complex was inserted into dimyristoylglycerophosphatidylcholine (DMPC) as a biomimetic membrane. However, the structure of the channel/lipid system was too large for computer simulation, and, therefore, the DMPC layer was removed, and carbon atoms were fixed in certain places in the amphotericin B and ergosterol monomer to provide smaller and reliable structures [54]. The fixed carbon atoms and structures are shown in Fig. 4.2.

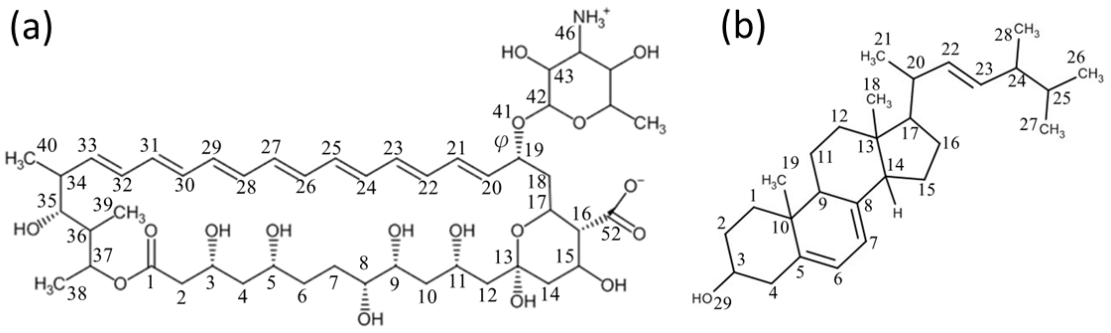

Fig.4.1 Chemical structures of (a) Amphotericin B, and (b) Ergosterol.

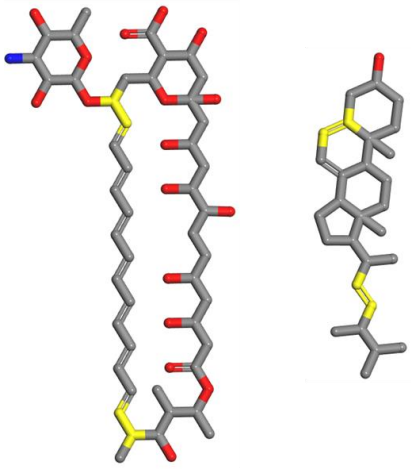

Fig.4.2 Specific fixed carbon atoms (yellow) in amphotericin B and ergosterol, respectively

As an amphoteric molecule, amphotericin B forms a channel with its hydrophilic hydroxyl groups pointing toward the channel's center. These amphotericin B molecules are symmetrically located in a cylindrical pore configuration. Ergosterol monomers are located at the wedges between the neighboring amphotericin B molecules. Sixteen monomers (eight amphotericin B and eight ergosterol monomers) were used as the starting conformation for the SLC AmBEr model. Two SLC models were connected in a tail-to-tail (hydroxyl group connect to C35 as shown in Fig. 1(a)) bilayer that formed the DLC model, as shown in Fig.

4.3. The detailed structural properties of the two types of simulation models are shown in Table 4.1.

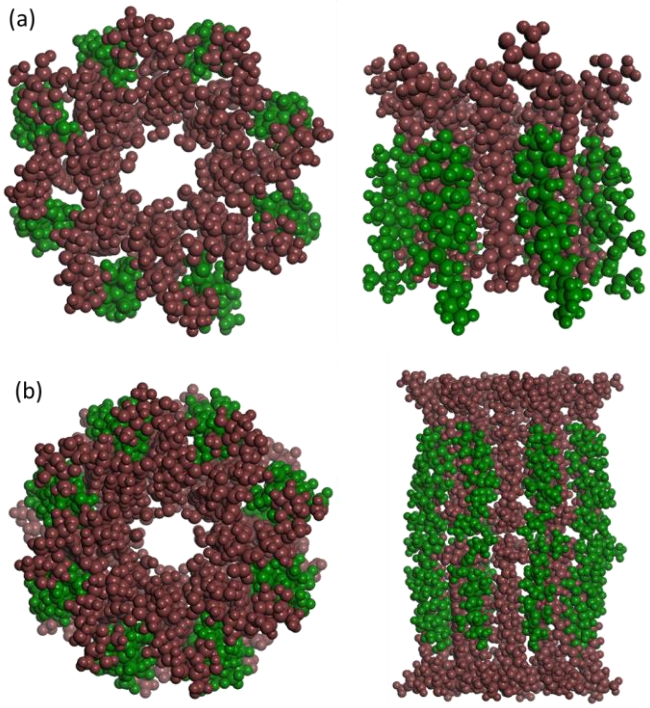

Fig.4.3 (a) Single layer AmBEr channel top view (left) side view (right), and (b) Double layer channel AmBEr channel top view (left) side view (right)
(brown: Amphotericin B, greed: ergosterol)

Table 4.1 Structural properties of AmBEr channel.

	SLC channel	DLC Channel
No. of Amphotericin B monomer [-]	8	16
No. of Ergosterol monomer [-]	8	16
Fixed Carbon Atoms [-]	64	128
Average Radius [Å]	5.9	5.2

In the first step, "Geometry Optimization" was introduced to optimize the energy of the model structure. In this process, energy calculation and changes in the structures of 5,000 iterations were carried out to establish sensible initial AmBEr channel structures. Next, the MD duration with a *NVT* ensemble (fixed atom number, system volume and temperature) at 298 K for 50-ps was applied to reach molecular structures under an equilibrium state. Finally, an equilibrated structure was adopted for the structural characterization and analysis of water transport behavior. The details of the simulation procedures for preparing the AmBEr channel model are described in the supplementary information. In this study, the Condensed-phase Optimized Molecular Potential for Atomistic Simulation Studies (COMPASS) force field [55-57] was adopted in order to perform energy minimization and MD calculation processes. The various functional forms in this force field are illustrated as follows:

$$
\begin{aligned}
E = & \sum_{b}\left[K_2(b-b_0)^2 + K_3(b-b_0)^3 + K_4(b-b_0)^4\right] \\
& \textbf{(a)} \\
& + \sum_{\theta}\left[H_2(\theta-\theta_0)^2 + H_3(\theta-\theta_0)^3 + H_4(\theta-\theta_0)^4\right] \\
& \textbf{(b)} \\
& + \sum_{\phi}\left\{V_1\left[1-\cos\left(\phi-\phi_1^0\right)\right] + V_2\left[1-\cos\left(2\phi-\phi_2^0\right)\right] + V_3\left[1-\cos\left(3\phi-\phi_3^0\right)\right]\right\} \\
& \textbf{(c)} \\
& + \sum_{x} K_x x^2 + \sum_{b}\sum_{b'} F_{bb'}(b-b_0)(b'-b'_0) + \sum_{\theta}\sum_{\theta'} F_{\theta\theta'}(\theta-\theta_0)(\theta'-\theta'_0) \\
& \textbf{(d)} \qquad\qquad \textbf{(e)} \qquad\qquad \textbf{(f)} \\
& + \sum_{b}\sum_{\theta} F_{b\theta}(b-b_0)(\theta-\theta_0) + \sum_{b}\sum_{\phi}(b-b_0)\left[V_1\cos\phi + V_2\cos 2\phi + V_3\cos 3\phi\right] \\
& \textbf{(g)} \qquad\qquad\qquad\qquad \textbf{(h)} \\
& + \sum_{b'}\sum_{\phi}(b'-b'_0)\left[V_1\cos\phi + V_2\cos 2\phi + V_3\cos 3\phi\right] \\
& \textbf{(i)} \\
& + \sum_{\phi}\sum_{\theta}\sum_{\theta'} K_{\phi\theta\theta'}\cos\phi(\theta-\theta_0)(\theta'-\theta'_0) + \sum_{i>j}\frac{q_i q_j}{\varepsilon r_{ij}} + \sum_{i>j}\left[\frac{A_{ij}}{r_{ij}^9} - \frac{B_{ij}}{r_{ij}^6}\right] \\
& \textbf{(j)} \qquad\qquad \textbf{(k)} \qquad \textbf{(l)}
\end{aligned}
\tag{1}
$$

The energy terms are composed of three categories: bonded energy terms, cross-interaction terms, and non-bonded energy terms. The bonded energy terms include (a) the covalent bond-stretching energy terms, (b) the bond-angle bending energy terms, and (c) the torsion-angle rotation energy terms. The designation (d) is the out-of-plane energy or improper term. The terms for cross-interaction consist of the dynamic variations among bond stretching, bending, and torsion angle rotation interactions ((e)–(j)). The non-bonded energy terms, (k) and (l), represent the Coulombic electrostatic interaction force and the van der Waals (vdW) potential force, respectively.

4.2.2. Physical property analysis

The present study was focused on elucidating the structural properties and water-molecule transport behaviors in an AmBEr channel via the application of MD simulation techniques. Details of physical properties are described in this section.

4.2.2.1 Structural characteristics

To describe and compare the channel morphology of SLC and DLC AmBEr simulation models, the channel morphology and inner diameter were discussed. First, the channel morphology was analyzed to determine how the tunnel design affected the transport of water molecules in those channels. Second, the inner diameter of the opposing amphotericin B subunit was estimated in order to compare the channel structures of the two simulation models. Both the channel morphology and the internal diameter were estimated based on van der Waals radii of the simulation models, and these were obtained using the Visualizer Module in BIOVIA Materials Studio® commercial software.

4.2.2.2 Hydrogen bond analysis

The affinity between water molecules and channel surface was considered an important factor for water mobility in the AmBEr channels. Thus, the distribution of the hydrogen bonds was analyzed to explore the inner affinities of the AmBEr channel simulation models. The distribution of the hydrogen bonds between water-channels was obtained using the Visualizer Module in BIOVIA Materials Studio® commercial software and an *NVT*-MD

simulation ensemble at a temperature of 298 K, and with 80 and 100 water molecules within the SLC and DLC AmBEr models, respectively.

4.2.2.3 Water sorption isotherm

The process of water molecules sorption in an AmBEr channel can be described using the Grand Canonical Monte Carlo (GCMC) method. In a simulation, the relative probabilities of the different states of a system were represented using a Metropolis algorithm. The adsorbed amount of water molecules was represented by four types of configurations: conformer, rotation, translation, and regrowth. The sorption analysis calculation in this work was processed 5,000,000 times. The number of water molecules adsorbed by the inner AmBEr channels was recorded, and the sorption loading was evaluated as a function of the water vapour pressure.

2.2.4 Mean-squared displacement (MSD)

The mean-squared displacement (MSD) of water molecules in the AmBEr channel was calculated using the *NVT* MD simulation method in order to analyze the transport abilities and differences in the diffusion behavior of the water molecules in the two AmBEr simulation models. The diffusion coefficient of the water in the AmBEr channel was easily obtained using the Einstein relationship:

$$MSD(t) = \frac{1}{N}\sum_{i=1}^{N}\{[r_i(t_0 + t) - r_i(t_0)]^2\} = B + d_n D \times \mathrm{t} \qquad (2)$$

where N is the total number of atoms, r_i (t_0+t) and r_i (t_0) are the positions at time t_0+t and time t_0, respectively, B is a constant, d_n is the geometrical dimension of diffusion, and D is the diffusion coefficient. The diffusion coefficient can be calculated from the slope of the MSD curve. In this work, water molecules were inserted into the channel and provided an 800 ps calculation period in order to obtain the MSD diagrams as a function of elapsed MD simulation time. To obtain the free diffusion in a bulk phase, $d_n = 6$ is generally used. In an AmBEr channel, however, diffusivity in the direction of the water channel was significant, and it is plausible to assume that diffusion is a one-dimensional property. Therefore, $d_n = 2$ was adopted to calculate the water diffusion coefficient inside the AmBEr channel.

4.3. Results and discussion

4.3.1. Model validation

To confirm the feasibility of all the molecular models in this work, some specific properties of the two types of channel models (SLC and DLC) were explored. These properties are helpful in validating the correctness and applicability of the simulation. Both SLC and DLC AmBEr models were constructed for validation before further exploration. The equilibrated structures of these two models of channels were achieved using MD simulation and *NVT* ensemble calculation. Simulation research that focused on AmB channel structures was widely investigated. The results of those studies indicated that the interaction between amphotericin B and ergosterol is an important factor for the stability of a structure [58-60]. For validation, the intramolecular and intermolecular properties of the channel models found in the present study were compared with the results of previous studies.

(a) Intramolecular properties

As mentioned, fixed carbon atoms were used instead of the DMPC bilayers in order to offset the issue of computer limitations. The rotation of the flexible segment with hydrophilic functional groups of amphotericin B was first verified by tracking the ability of amphotericin B monomers to form intramolecular hydrogen bonds. With the rotation of a polyhydroxyl segment, hydroxyl functional groups which connected to a carbon on the flexible fragment of amphotericin B molecule could form an intramolecular hydrogen bond with neighboring hydroxyl groups, as shown in Fig.4.1. The time frame for the evolution of the number of intramolecular hydrogen bonds is presented for two types of AmBEr simulation models in Fig. 4.4. The difference between the SLC and DLC simulation models was limited around 5 hydrogen bonds per amphotericin B molecular. The DLC AmBEr channel exhibited a somewhat higher value for the hydrogen bond compared with that of the SLC AmBEr. The similar number of hydrogen bonds suggested that the flexible segment of simulation model was able to rotate freely while specific carbon atoms remained fixed.

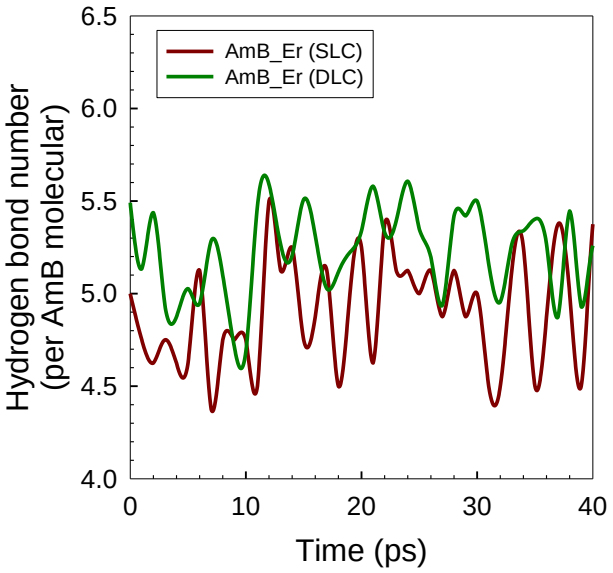

Fig.4.4 Intramolecular hydrogen bond analysis

The amino sugar moiety of amphotericin B is the most flexible of monomer fragments, and this flexibility is due to the rotation around the C19-O41 and O41-C42 bonds. These dihedral angles determine how the amino sugar moiety is positioned. As shown in a previous study [61], the distribution of the dihedral angles reflects two formations: open and closed. In the open ($\phi \approx -150°$) configuration, the amino sugar moiety and carboxyl groups have the ability to form intermolecular hydrogen bonds with the neighboring amphotericin B monomers. This interaction helps stabilize the channel. By contrast, the moiety and carboxyl groups in the closed ($\phi \approx -60°$) configuration tend to form intramolecular hydrogen bonds. The closed location did not contribute to channel stability. The distributions of the dihedral angles for SLC and DLC are shown in Figs. 4.5(a) and Fig. 4.5(b), respectively. Both angles of the SLC and DLC simulation models were located in the open formation field. This shows that the channel complex formation would be a valid subject for further exploration.

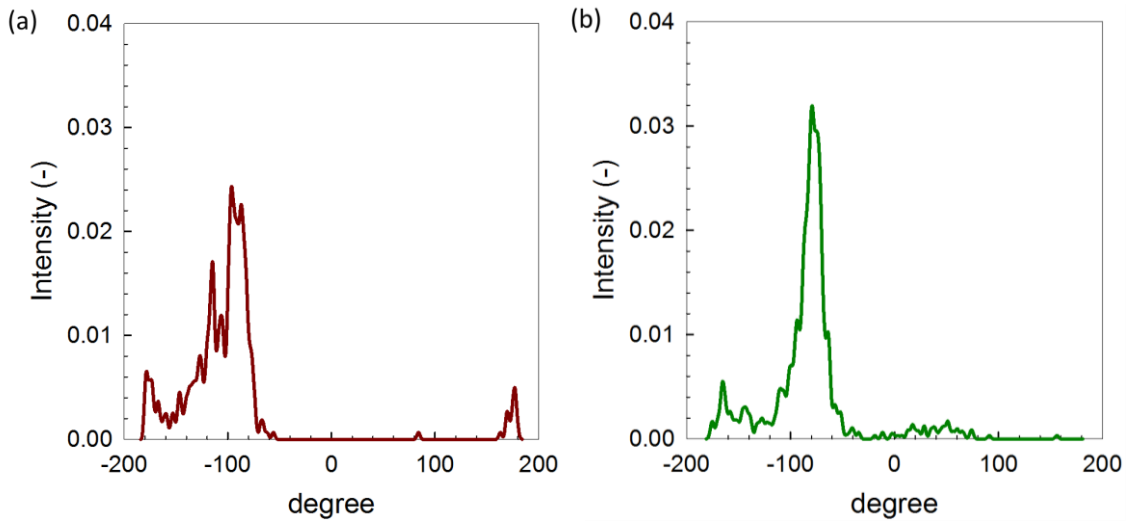

Fig.4.5 Distribution of dihedral angle of Amphotericin B monomer (a) SLC, (b) DLC simulation model.

(b) Intermolecular properties

Because the channel complex consists of amphotericin B and ergosterol monomers, the intermolecular interactions between adjacent amphotericin B and between neighbouring amphotericin B and ergosterol are analyzed. Among these two, the interactions between neighbor amphotericin B were considered to be critical for the stability of the channel structure. Based on the chemical structure of an amphotericin B monomer, with proper orientation of the hydroxyl functional groups, amphotericin B forms either intramolecular hydrogen bonds or intermolecular hydrogen bonds. This was revealed by the number of hydrogen bonds between neighboring pairs of amphotericin B, as shown in the investigation of MD trajectories that is illustrated in Fig. 4.6. The distribution of the intermolecular hydrogen bonds was similar between the SLC and DLC simulation models. The DLC simulation model, however, showed slightly higher values. The intermolecular hydrogen

bonds between adjacent amphotericin B monomers are indispensable for channel stability, which explains how the channel structure of both types of simulation models remained stable during the diffusion and sorption calculations.

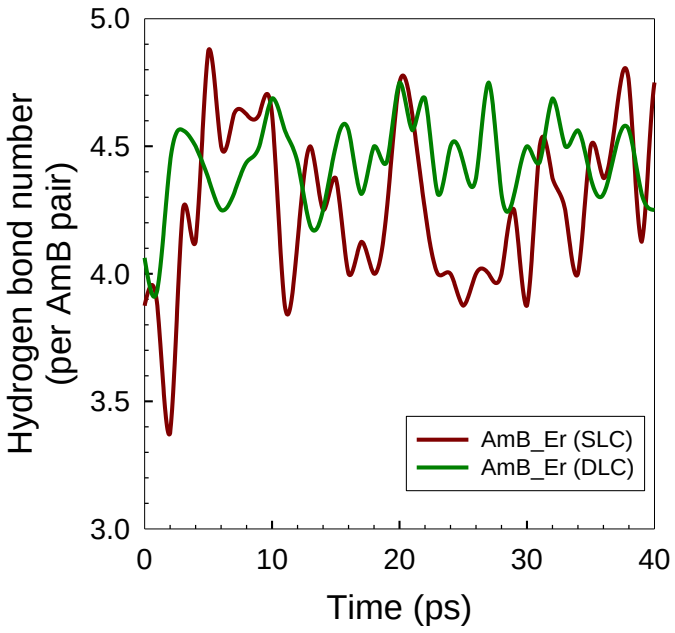

Fig.4.6 Intermolecular hydrogen bond analysis

Intermolecular hydrogen bond distribution shows the interaction between adjacent amphotericin B monomers. In order to further explore the channel structural geometry, the specific distances between selected carbon atoms in the inflexible parts of amphotericin B and ergosterol monomers were tracked and investigated: (i) distance between the C9 carbon atom of amphotericin B and the C19 carbon atoms of ergosterol; and, (ii) distance between the C22 carbon atom of amphotericin B and the C19 carbon atom of ergosterol (Fig. 4.1). These two selected distances reflect the relative position between amphotericin B and ergosterol monomers, which shows the up and down movement of amphotericin B as well as

the length of its axis. The degree of similarity for these distances reflects the stability of the channel complex. The values of the distances for the two types of channel models are shown in Fig. 4.7. The C9 (amphotericin B)-C19 (ergosterol) and C22 (amphotericin B)-C19 (ergosterol) distances between amphotericin B and ergosterol were similar (around 7.5 Å) in both types of simulation models, which revealed that amphotericin B would correspond to a parallel array of an ergosterol monomer.

These results were compared with those of previous research [61]. Although the absolute values of the distance (around 7 Å) differed slightly, the conformation of the amphotericin B monomer amino groups and the stability of the channel complex were successfully described by the two types of simulation models. Thus, the molecular models used in this work were validated.

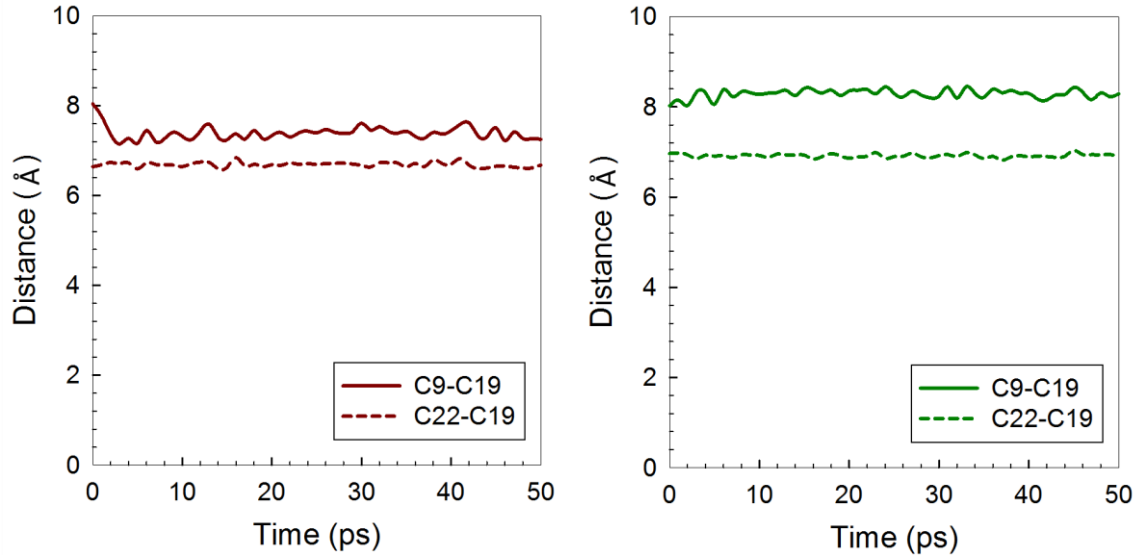

Fig.4.7 Time course of specific distance between amphotericin B and ergosterol.

4.3.2. Channel volume analysis

The sectional views of the two types of channel models (SLC and DLC) are shown in Fig. 4.8. The characteristics of the channel shape and inner diameter were dominant factors in the water transport performance. To study the structural properties of the two types of simulation models, the inner diameter and morphology of the channel models were examined in detail. The different configurations for SLCs and DLCs are shown in Fig. 4.8. The green dot regions indicate the pathways inside the channels. In both channel models the tunnel had a funneled shape so that the entrance and exit of the channel provided a large space that would benefit the movement of molecules. Also, the narrower mid-portion of the channel provided selectivity. The red dashed line in Fig. 8 reveals the narrowest distance of each channel model.

The results that determined the internal diameter (C6-C6 as shown in Fig. 4.1(a)) are shown in Fig. 4.9 as a function of MD simulation time. The values of the two types of channel models remained very close with respect to channel diameter at a steady state during the calculation.

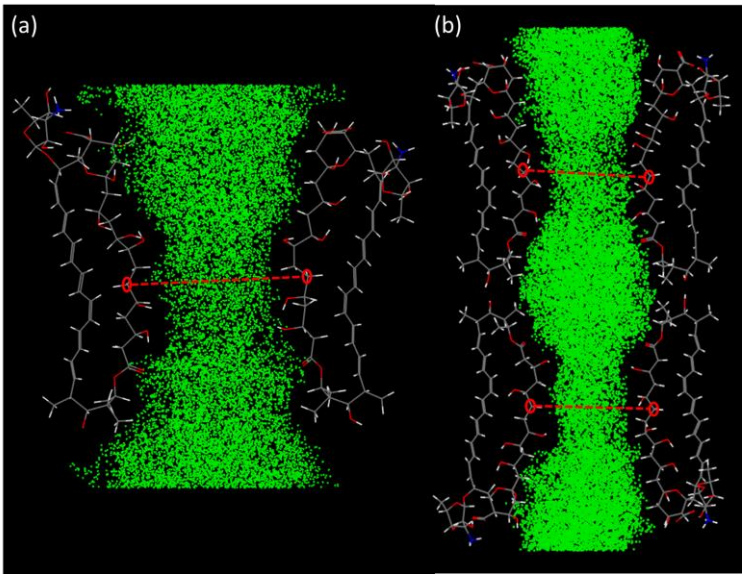

Fig.4.8 Section view of SLC and DLC simulation channel model.

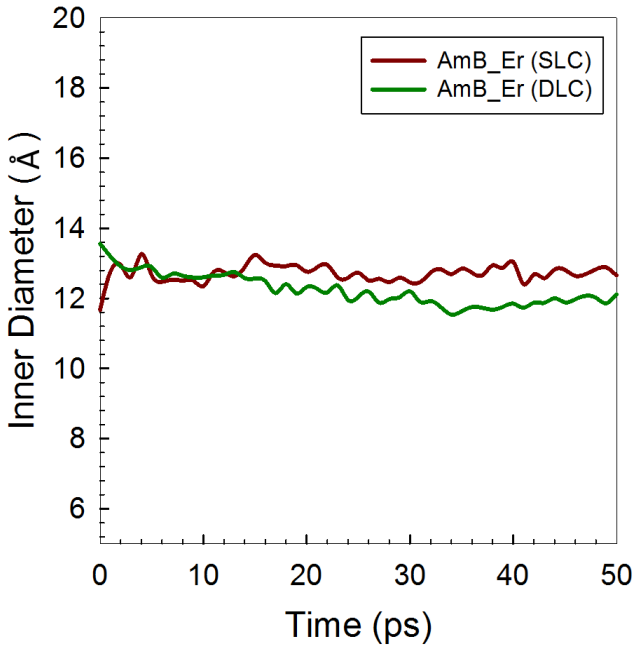

Fig.4.9 Internal diameter of SLC and DLC simulation channel model.

4.3.3. Hydrogen bond analysis

As previously mentioned, this research was undertaken to construct and explore SLC and DLC AmBEr models. To understand how the affinity between water molecules and AmBEr channels affects the transport behavior of water, the hydrogen bonds between AmBEr channels and water molecules were discussed. The water molecules were straight put inside channel at initial. After calculation, water molecules freely transported within channel. During the calculation period, the trajectory of water molecules was recorded and some specific time points were selected for hydrogen bond analysis. The number of water molecules was decided according to the result of sorption isotherm as shown in Fig. 4.13, where the saturated water molecules number at low pressure region was 80 and 100 for SLC and DLC, respectively. The distribution of the numbers of hydrogen bonds between the

AmBEr channels and water molecules in the two types of simulation models is shown in Fig. 4.10. Based on our observations of each of the models, the value of the number of hydrogen bonds was slightly altered for a calculation period of more than 300 ps. In other words, the formation of a hydrogen bond can be attributed to two different regions. First, between 100 and 300 ps, the water molecules are transported within the hydrophobic region of an AmBEr channel. Second, after 300 ps, the water molecules are conducted from the narrow hydrophobic middle tunnel to the hydrophilic segment of the AmBEr channel (head and tail of channel), as shown in Fig. 4.11.

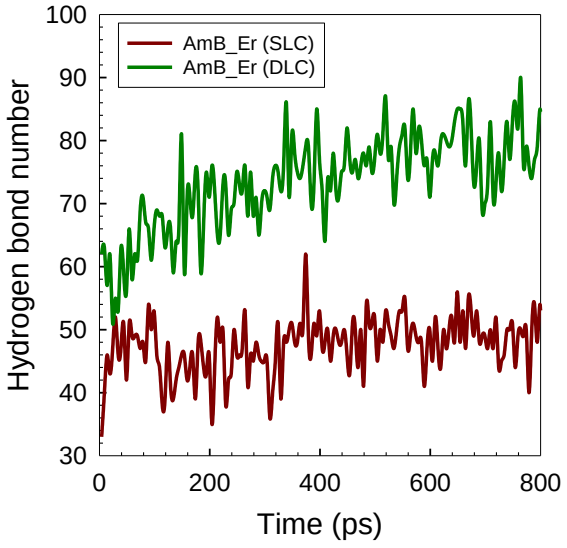

Fig.4.10 Intermolecular hydrogen bond between AmBEr channel and water molecules.

As the calculation time increases, the hydrophilic head and tail of the channel attract more water molecules, which increases the number of hydrogen bonds. This finding agrees with the results of the structural properties, wherein the hydrophilic and hydrophobic properties on an amphotericin B monomer were reflected for simultaneous interactions with water

molecules. The most apparent difference between the results for the SLC and DLC AmBEr channels was that the distribution of trend of amphotericin B–water hydrogen bonds had a slightly more variation in the DLC channel. This could be suggesting that water molecules within DLC channel was more unstable because of the hydrophobic centre. In the case of the SLC channel, there was no significant changing during the calculation period. This property divergence reflects different transport mechanism in following analysis.

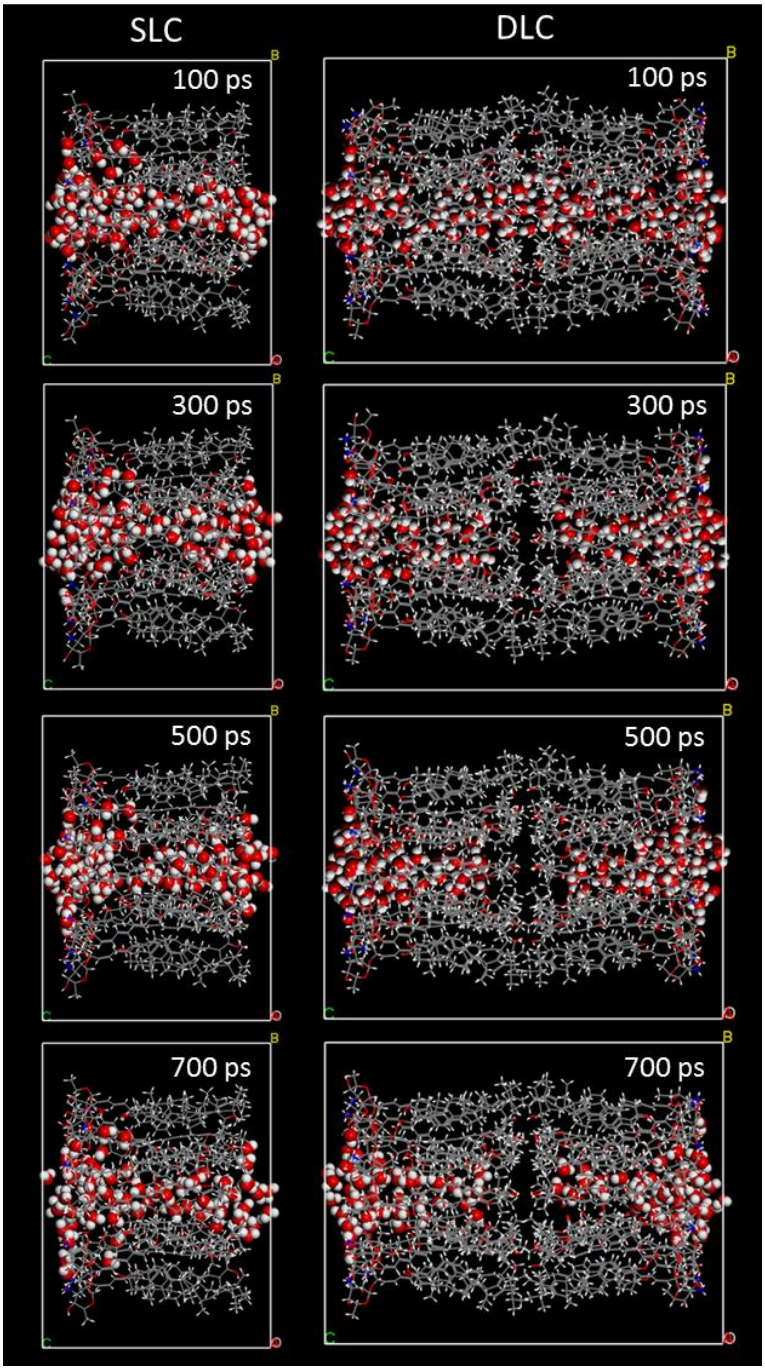

Fig.4.11 Snapshots during MSD simulation period at 100 ps, 300 ps, 500 ps and 700 ps.

3.3.4. Molecular transport behaviors

The solution-diffusion model can be used to examine the transport behavior during theoretical calculation. In other words, permeability is dependent on both the sorption and diffusion behaviors. Therefore, these two dominating factors will be discussed separately in order to promote a full understanding of the water transport in both SLC and DLC AmBEr models.

(a) Sorption of water molecules

The sorption position of water molecules in the SLC and DLC AmBEr models are shown in Fig. 4.12. Based on this adsorption site snapshot, the sorption behavior can be explained in three steps. First, in the low-pressure region, the molecules tended to adsorb at the entrance and exit of the AmBEr channel — the most hydrophilic portions in the AmBEr channel complex. Second, when increasing the water vapor pressure to the middle-pressure region, the adsorption sites are the entrance and exit tended to be saturated. Besides, in the DLC AmBEr channel model, the molecules started to adsorb in the middle of the channel. Third, when increasing the pressure to 1 atm, almost all adsorption sites tended to be saturated with water molecules and some molecules were even adsorbed in the narrow hydrophobic zone of the channel. In simple terms, as shown in the snapshot, the affinity of the narrow hydrophobic zone was too low to adsorb molecules, and most of the molecules were adsorbed around the hydrophilic segment of the channel complex.

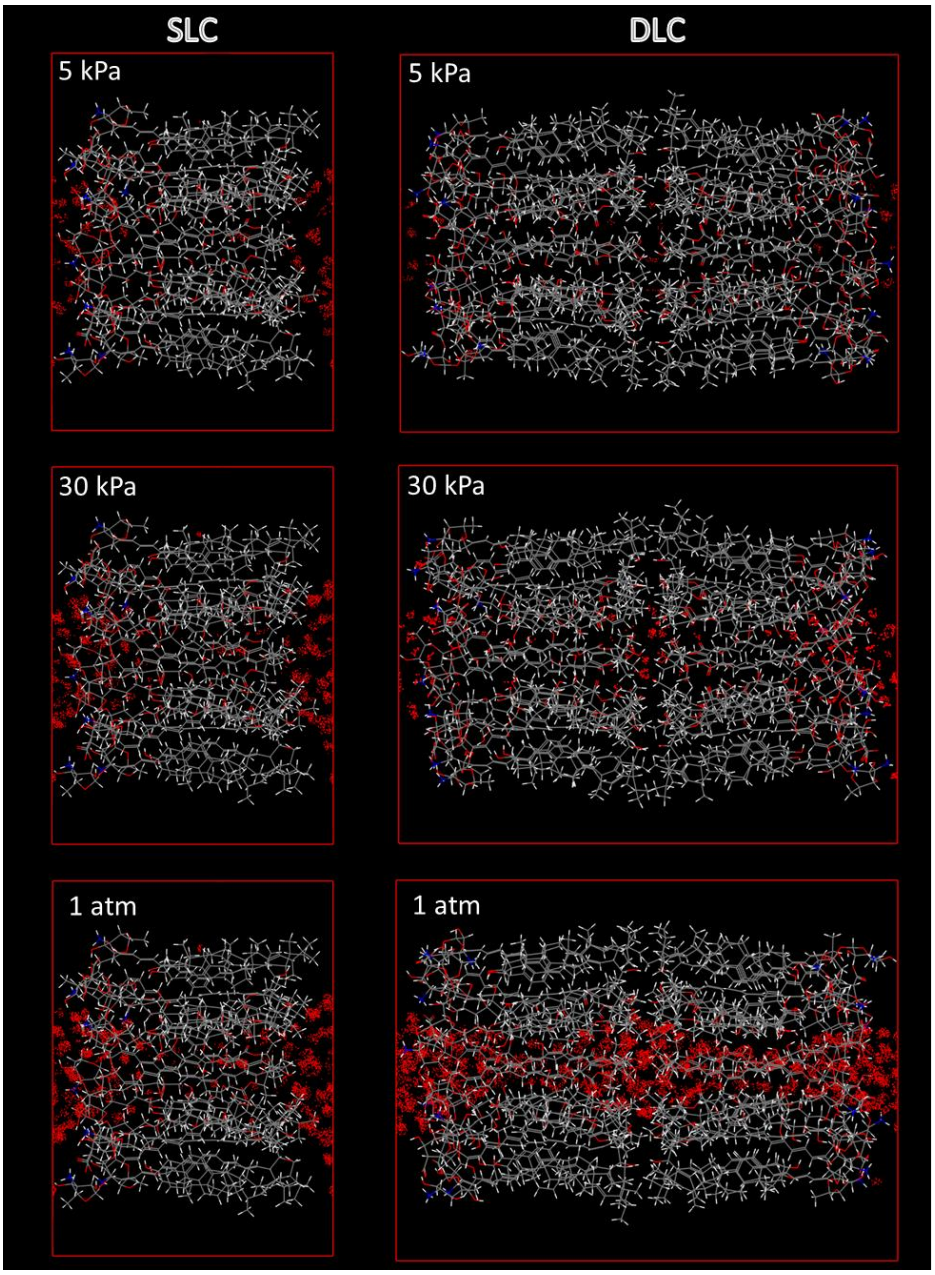

Fig.4.12 Adsorption location under 5 kPa, 30 kPa and 101.3 kPa (1 atm). (Adsorption sites represents by red dots)

Since the channel shapes and internal diameters of these two types of AmBEr channels were similar, water-channel affinity was considered a critical issue for sorption behavior. To better understand the sorption behaviors inside the channels, the sorption isotherms of the

SLC and DLC AmBEr models were studied. Fig. 4.13 shows the water molecule sorption isotherms at 298 K up to a pressure of 1 atm. The sorption isotherms indicated comparable sorption behaviors for two different AmBEr channel models whereby similar three-step sorption mechanisms were observed in the adsorption site analyses. High affinity between water molecules and the channel (head and tail) introduced a hydrophilic adsorption phenomenon, which was observed in the curves of both types of channel models in low-pressure regions. With increasing pressure, the isotherm showed a temporary saturated landing because the high-affinity adsorption sites were filled with water molecules. After this stage, the adsorption amounts increased again until a final saturated condition was reached. In general, the adsorption capacity of a DLC model should be two-fold that of an SLC model. The unfavorable result shown in Fig. 4.13 was caused by an effective adsorption site. Water molecules easily and quickly occupy the hydrophilic heads and tails of SLCs. When two SLCs were connected tail-to-tail to form a DLC model, however, the channel-water molecule affinity was decreased, although the hydrophilic interaction contributed to this channel connection. Some analyses can be evidence for the hydrophobicity of centre of DLC channel.

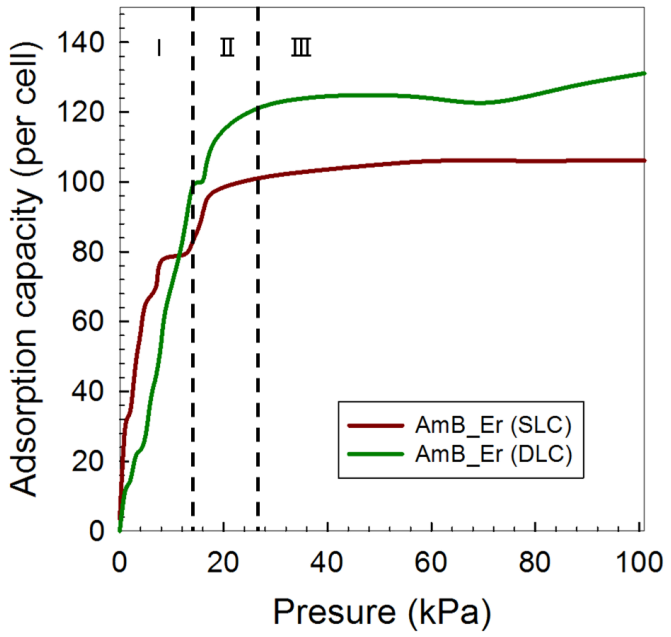

Fig.4.13 Adsorption isotherm curve of water in AmBEr channel models.

From the snapshot of DLC model during MSD simulation as shown in Fig. 4.11. With the calculation time increasing, water molecules were transported to the entrance and exited channel. As the result, no water molecules existed in the centre of channel at 700 ps. This phenomenon reflected the hydrophobicity of the centre of DLC channel. Further, based on the results of the adsorption isotherms, when an equilibrated sorption pressure was 10 kPa, the adsorption capacity of DLC channel should be two-fold more than SLC channel, however unexpected result was shown in Fig. 4.13. The unpredicted lower sorption capacity of DLC channel also suggested the low affinity of centre of DLC channel. Furthermore, as shown in Fig. 4.10, the hydrogen bond numbers between channel/water molecules in the DLC layer were not two-fold higher than that of a SLC layer. In other words, the efficiency of the

adsorption sites was less than we expected, which resulted in the disappointing sorption amounts in the DLC.

(b) MSD and diffusivity

Fig. 4.14 shows the mean squared displacement (MSD) diagrams of water molecules for the two types of channel models during the *NVT* MD simulation for a period of 800 ps at 298 K. The displacement and slope indicates the transport ability of water molecules inside the AmBEr channels. In the MSD diagrams of water molecules, large values for the displacement and slope indicate the high mobility of water molecules. As shown in Fig. 4.14, the DLC AmBEr model revealed larger values of displacement. This result was due to the larger channel volume and lower affinity to water molecules inside the narrow channel [48]. The large and hydrophobic narrow internal tunnel provided sufficient space, and the reduced transport barrier allowed water molecules to move more rapidly inside the AmBEr channels. After 600 ps, however, the displacement dramatically decreased because water molecules were attracted by the hydrophilic segments (head and tail) of the channel complex. Accordingly, the displacement of the water molecules in the SLC model was much lower than that in the DLC model due to the shorter channel length and the attraction to the hydrophilic head and tail.

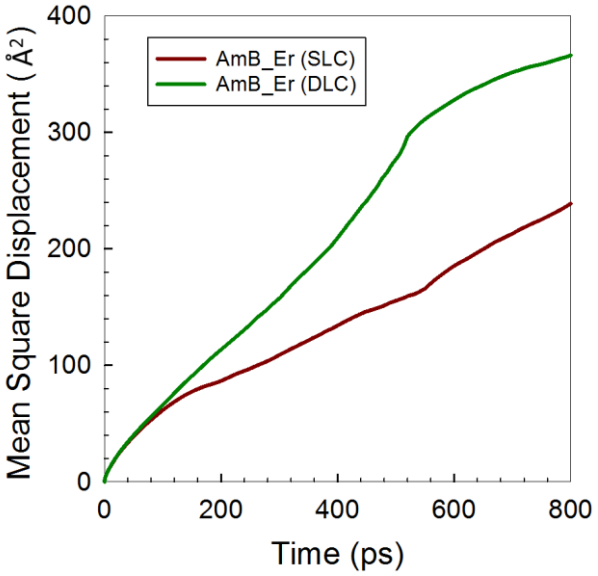

Fig.4.14 MSD curve of water in AmBEr channel models.

In general, the displacement and slope was expected to close in both types of AmBEr channel models because of the similar inner diameter and channel shape, as discussed above. As shown by the MSD curves, the DLC model exhibited higher displacement than that of the SLC model. This finding agreed well with the results of the hydrogen bond distribution between water-AmBEr channels. Water molecules within the channel were attracted to the hydrophilic segments of the AmBEr channel complex. The shorter channel length of the SLC AmBEr model created a situation whereby the water molecules were more easily affected by the hydrophilic segments. On the other hand, in the DLC AmBEr model, the middle section of the hydrophobic tunnel was long enough to mitigate the attraction by the hydrophilic head and tail, which allowed water molecule transport. This apparent difference in water molecular diffusion reflected the distinct diffusion conductance of these two types of AmBEr channels.

(c) Water permeability

The overall permeability was based on the solubility and diffusivity of the solution-diffusion model [62]. The values for the solubility, diffusivity coefficients, and permeability data of the two types of AmBEr channel models are summarized in Table 4.2. First, the values of water permeability indicate how the water molecules permeate different types of channels. When the diffusivity and solubility coefficients inside the tunnel-shaped channel models were compared, the two types of simulation models showed totally different properties. Due to a short channel length and hydrophilic head and tail segments, water molecules easily entered the SLC AmBEr model. In other words, the highly effective adsorptive behavior led to a higher solubility coefficient value in the SLC model. Although the long channel length of the DLC AmBEr model decreased the adsorption effectiveness, the sufficient hydrophobic space and the diminished attractive interaction by the hydrophilic head and tail allowed water molecule movement. As a result, a higher mobility of water molecules was observed in the DLC AmBEr model. When comparing these two estimates of permeability data, we concluded that the permeability performance of AmBEr channels is affected mainly by channel affinity. As illustrated in Table 2, the SLC and DLC AmBEr models had similar permeability values, as we expected. In the transport procedure, both sorption and diffusion ability were influenced by the channel-water affinity. The trade-off relationship between channel affinity-diffusion and the proportional relationship between channel affinity-adsorption is an important issue for membrane material development in water treatment applications.

Table 4.2 Solubility coefficient, diffusivity coefficient, and permeability.

	SLC	DLC
Solubility Coefficient [mol/m^3]	4.75	2.66
Diffusion Coefficient [m^2/s]	1.3×10^{-9}	2.1×10^{-9}
Permeability [$mole\ m/(m^2\ s\ Pa)$]	6.2×10^{-9}	5.6×10^{-9}

In this work, the SLC and DLC AmBEr models showed similar levels of water permeability, and they are expected to provide high efficiency in the water transport process. The different water transport mechanisms between the two types of channel models could supply a variety of possible biomimetic membranes that could have a wide range of applications. However, in actual water permeation in saturated liquid phase through the channel, the higher density of the permeating molecules and the resistance at entrance of the channel from the bulk water phase can be reason for reducing water permeabilty. In order to predict more realistic permeability values, those effect should be considered in molecular simulation models. Another concern is the ion rejection performance of these types of channel, which should be also in future work.

4.4. Conclusion

The structural characteristics and transport behaviors of the two types of AmBEr channel models were thoroughly analyzed via MD and MC simulations. The intramolecular properties of the amphotericin B subunits and the intermolecular interaction between

amphotericin B and ergosterol monomers were explored for model validation. The results illustrated the feasibility of the model construction method and validate the simulation model in this study. The channel morphology and calculated internal diameter revealed the funnel shape of the AmBEr channel models. The shape suggests space for the head and tail sufficient to provide the diffusion of water molecules with a tight middle tunnel that could contribute to selectivity during the separation process. Hydrogen bond analysis and an adsorption site snapshot indicated an affinity between water molecules and the AmBEr channels. The results demonstrated that the hydrophilic segment of the channel complex easily attracts water molecules. Based on mean squared displacement analyses, the DLC AmBEr model had a longer hydrophobic tunnel that promotes the transport of water molecules. Water molecules within the SLC model having a shorter tunnel were more easily attracted by the hydrophilic segments, which led to a lower level of displacement. In addition, although the diffusion and adsorption properties of SLC and DLC AmBEr models were quite different, the permeability performance was similar. In other words, transport behavior was dominated by molecular diffusion, and was controlled by sorption behavior. Since the structural features of element are similar, the performance of sorption behavior must be governed by the channel surface-water molecule affinity. In these two different types of channels, the channel-water affinity and channel length are the critical issues. Based on chemical structure, both the SLC and DLC models have hydrophilic head and tail segments therefore, in the adsorption isotherm, these two types of channels show similar adsorption behaviors. However, water molecules can enter the SLC AmBEr more easily because of the shorter channel length. In other word, the SLC model should have more effective adsorption behavior and a lower-pressure region,

which would lead to higher solubility. In contrast, the length of the long-channel of the DLC model should contribute to high mobility in the diffusion of water molecules. This long hydrophobic tunnel provides sufficient space and low affinity for water transport. By combining the results of diffusion and sorption, we attained similar water permeability performance despite the different transport mechanisms of these two AmBEr channel models.

The structural properties of the SLC and DLC AmBEr models were described in this study. Molecular simulations demonstrated different transportation mechanisms when these two examined AmBEr channels were compared. These results indicated that a computational experimental and analytical method on a microscopic scale, such as the present study, holds great promise as a method that could be used in the design and development of biomimetic membranes.

4.5 Reference

[1] D. Sammon, Membrane processes, Pure and Applied Chemistry, 37 (1974) 423-436.
[2] R.W. Baker, Membrane technology and applications, John Wiley & Sons, Ltd, (2004) 96-103.
[3] A.P. Rao, N. Desai, R. Rangarajan, Interfacially synthesized thin film composite RO membranes for seawater desalination, Journal of membrane science, 124 (1997) 263-272.
[4] Y. Kaufman, A. Berman, V. Freger, Supported lipid bilayer membranes for water purification by reverse osmosis, Langmuir, 26 (2010) 7388-7395.
[5] Y. Kaufman, S. Grinberg, C. Linder, E. Heldman, J. Gilron, Y.-x. Shen, M. Kumar, R. Lammertink, V. Freger, Towards supported bolaamphiphile membranes for water filtration: Roles of lipid and substrate, Journal of membrane science, 457 (2014) 50-61.
[6] T.D. Lazzara, C. Carnarius, M. Kocun, A. Janshoff, C. Steinem, Separating attoliter-sized compartments using fluid pore-spanning lipid bilayers, ACS nano, 5 (2011) 6935-6944.
[7] X. Li, R. Wang, C. Tang, A. Vararattanavech, Y. Zhao, J. Torres, T. Fane, Preparation of supported lipid membranes for aquaporin Z incorporation, Colloids and Surfaces B: Biointerfaces, 94 (2012) 333-340.
[8] G. Von Heijne, The membrane protein universe: what's out there and why bother?, Journal of internal medicine, 261 (2007) 543-557.

[9] M. Kumar, M. Grzelakowski, J. Zilles, M. Clark, W. Meier, Highly permeable polymeric membranes based on the incorporation of the functional water channel protein Aquaporin Z, Proceedings of the National Academy of Sciences, 104 (2007) 20719-20724.
[10] M.A. Knepper, S. Nielsen, Peter agre, 2003 Nobel Prize winner in chemistry, Journal of the American Society of Nephrology, 15 (2004) 1093-1095.
[11] C. Tang, Y. Zhao, R. Wang, C. Hélix-Nielsen, A. Fane, Desalination by biomimetic aquaporin membranes: Review of status and prospects, Desalination, 308 (2013) 34-40.
[12] H. Wang, T.S. Chung, Y.W. Tong, K. Jeyaseelan, A. Armugam, Z. Chen, M. Hong, W. Meier, Highly Permeable and Selective Pore‐Spanning Biomimetic Membrane Embedded with Aquaporin Z, Small, 8 (2012) 1185-1190.
[13] H.L. Wang, T.-S. Chung, Y.W. Tong, K. Jeyaseelan, A. Armugam, H.H.P. Duong, F. Fu, H. Seah, J. Yang, M. Hong, Mechanically robust and highly permeable AquaporinZ biomimetic membranes, Journal of membrane science, 434 (2013) 130-136.
[14] W. Xie, F. He, B. Wang, T.-S. Chung, K. Jeyaseelan, A. Armugam, Y.W. Tong, An aquaporin-based vesicle-embedded polymeric membrane for low energy water filtration, Journal of Materials Chemistry A, 1 (2013) 7592-7600.
[15] P.S. Zhong, T.-S. Chung, K. Jeyaseelan, A. Armugam, Aquaporin-embedded biomimetic membranes for nanofiltration, Journal of membrane science, 407 (2012) 27-33.
[16] P. Agre, D. Kozono, Aquaporin water channels: molecular mechanisms for human diseases1, FEBS letters, 555 (2003) 72-78.
[17] M. Hashido, M. Ikeguchi, A. Kidera, Comparative simulations of aquaporin family: AQP1, AQPZ, AQP0 and GlpF, FEBS letters, 579 (2005) 5549-5552.
[18] M. Hashido, A. Kidera, M. Ikeguchi, Water transport in aquaporins: osmotic permeability matrix analysis of molecular dynamics simulations, Biophysical journal, 93 (2007) 373-385.
[19] M. Ozu, H.A. Alvarez, A.N. McCarthy, J.R. Grigera, O. Chara, Molecular dynamics of water in the neighborhood of aquaporins, European Biophysics Journal, 42 (2013) 223-239.
[20] F. Zhu, E. Tajkhorshid, K. Schulten, Theory and simulation of water permeation in aquaporin-1, Biophysical Journal, 86 (2004) 50-57.
[21] L. Brunet, D.Y. Lyon, K. Zodrow, J.-C. Rouch, B. Caussat, P. Serp, J.-C. Remigy, M.R. Wiesner, P.J. Alvarez, Properties of membranes containing semi-dispersed carbon nanotubes, Environmental Engineering Science, 25 (2008) 565-576.
[22] E. Celik, H. Park, H. Choi, H. Choi, Carbon nanotube blended polyethersulfone membranes for fouling control in water treatment, Water research, 45 (2011) 274-282.
[23] J.-H. Choi, J. Jegal, W.-N. Kim, Fabrication and characterization of multi-walled carbon nanotubes/polymer blend membranes, Journal of Membrane Science, 284 (2006) 406-415.
[24] S. Kim, J.R. Jinschek, H. Chen, D.S. Sholl, E. Marand, Scalable fabrication of carbon nanotube/polymer nanocomposite membranes for high flux gas transport, Nano letters, 7 (2007) 2806-2811.
[25] S. Fernandez-Lopez, H.-S. Kim, E.C. Choi, M. Delgado, J.R. Granja, A. Khasanov, K. Kraehenbuehl, G. Long, D.A. Weinberger, K.M. Wilcoxen, Antibacterial agents based on the cyclic D, L-α-peptide architecture, Nature, 412 (2001) 452-455.
[26] M.R. Ghadiri, J.R. Granja, R.A. Milligan, D.E. McRee, N. Khazanovich, Self-assembling organic nanotubes based on a cyclic peptide architecture, Nature, 366 (1993) 324-327.

[27] W.S. Horne, C.M. Wiethoff, C. Cui, K.M. Wilcoxen, M. Amorin, M.R. Ghadiri, G.R. Nemerow, Antiviral cyclic d, l-α-peptides: Targeting a general biochemical pathway in virus infections, Bioorganic & medicinal chemistry, 13 (2005) 5145-5153.
[28] A. Finkelstein, O.S. Andersen, The gramicidin A channel: a review of its permeability characteristics with special reference to the single-file aspect of transport, The Journal of membrane biology, 59 (1981) 155-171.
[29] M.Ø. Jensen, O.G. Mouritsen, Single-channel water permeabilities of Escherichia coli aquaporins AqpZ and GlpF, Biophysical journal, 90 (2006) 2270-2284.
[30] P.A. Rosenberg, A. Finkelstein, Water permeability of gramicidin A-treated lipid bilayer membranes, The Journal of general physiology, 72 (1978) 341-350.
[31] Y. Tajima, K. Ono, N. Akaike, Perforated patch-clamp recording in cardiac myocytes using cation-selective ionophore gramicidin, American Journal of Physiology-Cell Physiology, 271 (1996) C524-C532.
[32] B. Wallace, Structure of gramicidin A, Biophysical journal, 49 (1986) 295-306.
[33] T. Belytschko, S. Xiao, G. Schatz, R. Ruoff, Atomistic simulations of nanotube fracture, Physical Review B, 65 (2002) 235430_1-235430_8.
[34] G. Hummer, J.C. Rasaiah, J.P. Noworyta, Water conduction through the hydrophobic channel of a carbon nanotube, Nature, 414 (2001) 188-190.
[35] K. Koga, G. Gao, H. Tanaka, X.C. Zeng, Formation of ordered ice nanotubes inside carbon nanotubes, Nature, 412 (2001) 802-805.
[36] D.J. Mann, M.D. Halls, Water alignment and proton conduction inside carbon nanotubes, Physical review letters, 90 (2003) 195503_1-195503_4.
[37] A. Waghe, J.C. Rasaiah, G. Hummer, Filling and emptying kinetics of carbon nanotubes in water, The Journal of chemical physics, 117 (2002) 10789-10795.
[38] K. Kim, D. Vercauteren, M. Welti, S. Chin, E. Clementi, Interaction of K+ ion with the solvated gramicidin A transmembrane channel, Biophysical journal, 47 (1985) 327-335.
[39] W. Lee, P.C. Jordan, Molecular dynamics simulation of cation motion in water-filled gramicidinlike pores, Biophysical journal, 46 (1984) 805-819.
[40] D. Mackay, P.H. Berens, K.R. Wilson, A. Hagler, Structure and dynamics of ion transport through gramicidin A, Biophysical journal, 46 (1984) 229-248.
[41] A. Skerra, J. Brickmann, Structure and dynamics of one-dimensional ionic solutions in biological transmembrane channels, Biophysical journal, 51 (1987) 969-976.
[42] A. Skerra, J. Brickmann, Simulation of voltage-driven hydrated cation transport through narrow transmembrane channels, Biophysical journal, 51 (1987) 977-983.
[43] G. Chen, S. Su, R. Liu, Theoretical Studies of Monomer and Dimer of Cyclo [(− l-Phe 1-d-Ala 2−) n] and Cyclo [(− l-Phe1-d-Me N-Ala2−) n](n= 3− 6), The Journal of Physical Chemistry B, 106 (2002) 1570-1575.
[44] H. Hwang, G.C. Schatz, M.A. Ratner, Steered molecular dynamics studies of the potential of mean force of a Na+ or K+ ion in a cyclic peptide nanotube, The Journal of Physical Chemistry B, 110 (2006) 26448-26460.
[45] H. Hwang, G.C. Schatz, M.A. Ratner, Ion Current Calculations Based on Three Dimensional Poisson− Nernst− Planck Theory for a Cyclic Peptide Nanotube, The Journal of Physical Chemistry B, 110 (2006) 6999-7008.

[46] E. Khurana, S.O. Nielsen, B. Ensing, M.L. Klein, Self-assembling cyclic peptides: molecular dynamics studies of dimers in polar and nonpolar solvents, The Journal of Physical Chemistry B, 110 (2006) 18965-18972.
[47] J.P. Lewis, N.H. Pawley, O.F. Sankey, Theoretical Investigation of the Cyclic Peptide System Cyclo [(d-Ala-Glu-d-Ala-Gln) m= 1-4], The Journal of Physical Chemistry B, 101 (1997) 10576-10583.
[48] H.-C. Wu, T. Yoshioka, H. Nagasawa, M. Kanezashi, T. Tsuru, D. Saeki, H. Matsuyama, Preparation of cyclic peptide nanotube structures and molecular simulation of water adsorption and diffusion, Journal of Membrane Science, (2017) 101-110.
[49] T.E. Andreoli, THE STRUCTURE AND FUNCTION OF AMPHOTERICIN B‐CHOLESTEROL PORES IN LIPID BILAYER MEMBRANES, Annals of the New York Academy of Sciences, 235 (1974) 448-468.
[50] T.E. Andreoli, V.W. Dennis, A.M. Weigl, The effect of amphotericin B on the water and nonelectrolyte permeability of thin lipid membranes, The Journal of general physiology, 53 (1969) 133-156.
[51] V.W. Dennis, N.W. Stead, T.E. Andreoli, Molecular aspects of polyene-and sterol-dependent pore formation in thin lipid membranes, The Journal of general physiology, 55 (1970) 375-400.
[52] R. Holz, A. Finkelstein, The water and nonelectrolyte permeability induced in thin lipid membranes by the polyene antibiotics nystatin and amphotericin B, The Journal of general physiology, 56 (1970) 125-145.
[53] P. Van Hoogevest, B. De Kruijff, Effect of amphotericin B on cholesterol-containing liposomes of egg phosphatidylcholine and didocosenoyl phosphatidylcholine. A refinement of the model for the formation of pores by amphotericin B in membranes, Biochimica et Biophysica Acta (BBA)-Biomembranes, 511 (1978) 397-407.
[54] V. Khutorsky, Ion coordination in the amphotericin B channel, Biophysical journal, 71 (1996) 2984-2995.
[55] D. Rigby, H. Sun, B. Eichinger, Computer simulations of poly (ethylene oxide): force field, pvt diagram and cyclization behaviour, Polymer International, 44 (1997) 311-330.
[56] H. Sun, COMPASS: an ab initio force-field optimized for condensed-phase applications overview with details on alkane and benzene compounds, The Journal of Physical Chemistry B, 102 (1998) 7338-7364.
[57] H. Sun, P. Ren, J. Fried, The COMPASS force field: parameterization and validation for phosphazenes, Computational and Theoretical Polymer Science, 8 (1998) 229-246.
[58] M. Baginski, J. Czub, K. Sternal, Interaction of amphotericin B and its selected derivatives with membranes: molecular modeling studies, The Chemical Record, 6 (2006) 320-332.
[59] M. Baginski, H. Resat, J.A. McCammon, Molecular properties of amphotericin B membrane channel: a molecular dynamics simulation, Molecular pharmacology, 52 (1997) 560-570.
[60] J. Czub, A. Neumann, E. Borowski, M. Baginski, Influence of a lipid bilayer on the conformational behavior of amphotericin B derivatives—a molecular dynamics study, Biophysical chemistry, 141 (2009) 105-116.
[61] M. Baginski, H. Resat, E. Borowski, Comparative molecular dynamics simulations of amphotericin B–cholesterol/ergosterol membrane channels, Biochimica et Biophysica Acta (BBA)-Biomembranes, 1567 (2002) 63-78.
[62] J. Wijmans, R. Baker, The solution-diffusion model: a review, Journal of membrane science, 107 (1995) 1-21.

Chapter 5

Applying Amphotericin B-Ergosterol in Forward Osmosis: a simulation study

5.1 Introduction

Access to potable water is becoming a serious problem with the growth of pollution and an ever-increasing world population. In recent years, water treatment via membrane processing has attracted much interest because of good performance and high efficiency. Nevertheless, increases in the demand for drinking water have increased the demand for high-performance water treatment membranes. Biomimetic membranes with artificial water channels are expected to be a new generation of membranes because of increases in water transport and higher ion rejection abilities [1-4]. In addition, the enhanced water flux of this type of water-channel design could be suitable for use in forward osmosis (FO) membrane processing [5-7], which is difficult to accomplish with ordinary polymeric membranes.

In order to develop this type of novel membrane, theoretical calculation on a molecular level was considered as a feasible tool [8-11]. This study in molecular dynamic simulation introduces an Amphotericin B-Ergosterol (AmBEr) artificial water channel in the membrane that is applicable to FO filtration.

5.2 Simulation method

5.2.1 Amphotericin B-Ergosterol molecular model

BIOVIA Materials Studio® software was used for the design and modeling via molecular simulation. The chemical structures of Amphotericin B and ergosterol appear in Fig. 5.1(a). A double-layer AmBEr channel was adopted in this FO filtration simulation work, as shown in Fig. 5.2. The optimized structure of the double-layer AmBEr channel consisted of sixteen amphotericin B chains and sixteen ergosterol monomers. Generally, an AmBEr channel complex was inserted into dimyristoylglycerophosphatidylcholine (DMPC) as a biomimetic membrane. However, the scale of the channel/lipid system was too large for computer simulation. Therefore, in this work, the DMPC layer was removed, and carbon atoms were fixed in certain places in the amphotericin B and ergosterol monomer to provide a smaller simulation system with reliable structures. The positions of the fixed carbon atoms are shown in Fig. 5.1(b).

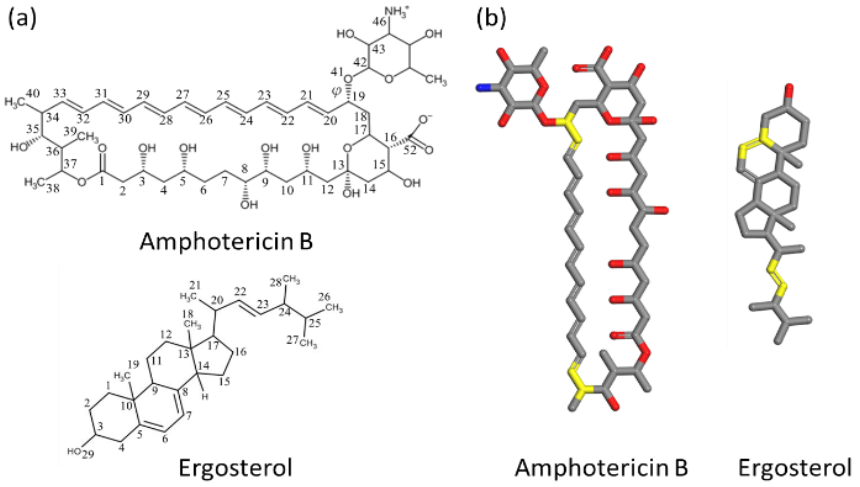

Fig. 5.1 (a) Chemical structure of Amphotericin B and Ergosterol monomers. (b) Specific fixed carbon atoms (yellow) in Amphotericin B and Ergosterol, respectively.

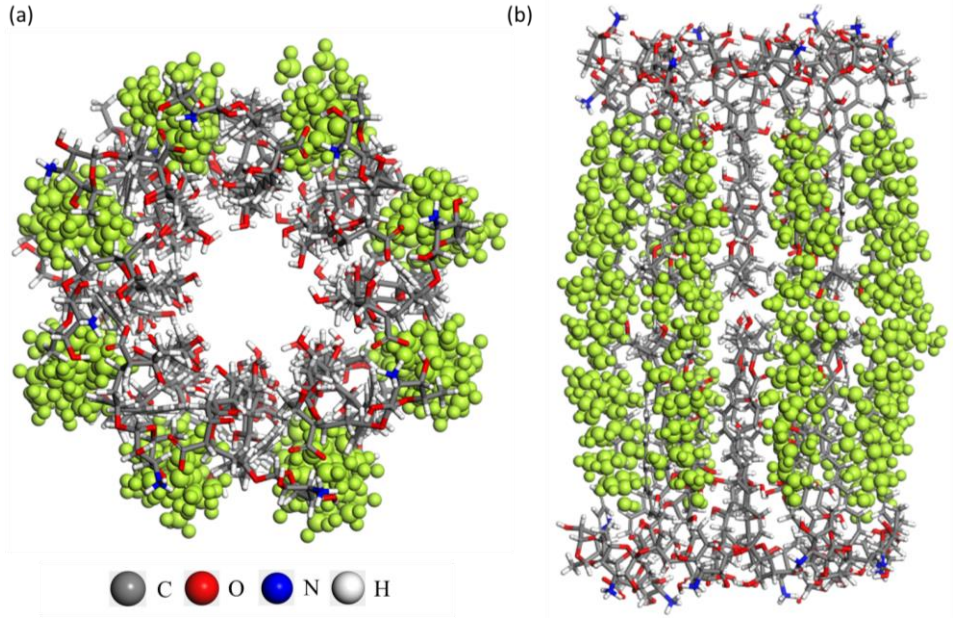

Fig. 5.2 (a) Top view, and (b) side view of a double-layer AmBEr channel. (Ergosterol monomers were represented in green)

After model construction, "Geometry Optimization" was introduced to enhance the energy of the model structure. In this process, energy calculation and changes in the structures of 5,000 iterations were carried out to establish a sensible initial channel structure.

Afterward, MD duration with an *NVT* ensemble (fixed atom number, *N*, system volume, *V*, and temperature, *T*) at 298 K for 4500 ps was applied to simulate the forward osmosis (FO) filtration phenomena. Finally, an observed non-equilibrium quasi-steady state was adopted for water permeability prediction. In this study, the Condensed-phase Optimized Molecular Potential for Atomistic Simulation Studies (COMPASS) force field [12-14] was adopted to perform the energy minimization and MD calculation processes. The various functional forms in this force field are illustrated as follows.

$$
\begin{aligned}
E = & \sum_{b}\left[K_2(b-b_0)^2 + K_3(b-b_0)^3 + K_4(b-b_0)^4\right] \\
& \textbf{(a)} \\
& + \sum_{\theta}\left[H_2(\theta-\theta_0)^2 + H_3(\theta-\theta_0)^3 + H_4(\theta-\theta_0)^4\right] \\
& \textbf{(b)} \\
& + \sum_{\phi}\left\{V_1\left[1-\cos\left(\phi-\phi_1^0\right)\right] + V_2\left[1-\cos\left(2\phi-\phi_2^0\right)\right] + V_3\left[1-\cos\left(3\phi-\phi_3^0\right)\right]\right\} \\
& \textbf{(c)} \\
& + \sum_{x} K_x x^2 + \sum_{b}\sum_{b'} F_{bb'}(b-b_0)(b'-b'_0) + \sum_{\theta}\sum_{\theta'} F_{\theta\theta'}(\theta-\theta_0)(\theta'-\theta'_0) \\
& \textbf{(d)} \qquad \textbf{(e)} \qquad \textbf{(f)} \\
& + \sum_{b}\sum_{\theta} F_{b\theta}(b-b_0)(\theta-\theta_0) + \sum_{b}\sum_{\phi}(b-b_0)\left[V_1\cos\phi + V_2\cos 2\phi + V_3\cos 3\phi\right] \\
& \textbf{(g)} \qquad \textbf{(h)} \\
& + \sum_{b'}\sum_{\phi}(b'-b'_0)\left[V_1\cos\phi + V_2\cos 2\phi + V_3\cos 3\phi\right] \\
& \textbf{(i)} \\
& + \sum_{\phi}\sum_{\theta}\sum_{\theta'} K_{\phi\theta\theta'}\cos\phi(\theta-\theta_0)(\theta'-\theta'_0) + \sum_{i>j}\frac{q_i q_j}{\varepsilon r_{ij}} + \sum_{i>j}\left[\frac{A_{ij}}{r_{ij}^9} - \frac{B_{ij}}{r_{ij}^6}\right] \qquad (1) \\
& \textbf{(j)} \qquad \textbf{(k)} \qquad \textbf{(l)}
\end{aligned}
$$

The energy terms comprise three categories: bonded energy, cross-interaction, and non-bonded energy. The bonded energy terms include (a) covalent bond-stretching energy terms, (b) bond-angle bending energy terms, and (c) torsion-angle rotation energy terms. The

designation (d) represents either out-of-plane energy or an improper term. The terms for cross-interaction represent the dynamic variations that exist among bond stretching, bending, and torsion-angle rotation interactions ((e)–(j)). The non-bonded energy terms (k) and (l) are the Coulombic electrostatic interaction force and the van der Waals (vdW) potential force, respectively.

5.2.2 Molecular model of forward osmosis simulation

In order to set up a model for the FO simulation of water and solute conduction, the simulation model cell was divided into three sections. First, the AmBEr channel that would be filled with water molecules was located in the middle of the simulation cell. The AmBEr channel was set between two reservoirs. The reservoir on the right-hand side was filled with 1615 pure-water molecules and another reservoir on the left-hand side was filled with an ion-pair aqueous solution of 50 Na^+ atoms, 50 Cl^- ion atoms, and 1470 water molecules, which corresponded to a molarity concentration of approximately 1.71 M. This salt concentration is about three times higher than that in actual sea water.

To simulate the FO process of filtration, as shown in Fig. 5.3, the periodic boundary conditions in the z-direction were cut off using two 40 Å fixed graphene layers in both the *x*- and *y*-directions. Each graphene layer helped avoid interactions between the pure-water and seawater reservoirs [15]. Mostly, this type of artificial water channel was surrounded by a lipid bilayer in order to form a biomimetic membrane. The scale of this system was too large for computer calculation. Therefore, instead of setting up a lipid bilayer, some specific carbon

atoms of amphotericin B and ergosterol were fixed in order to decrease the computer calculation load, as described above. To permit motions, rotations and vibrations by the Amphotericin B and ergosterol molecules, less than 5% of the channel atoms were pinned to fixed positions in the center of the cell during the simulation period, which allowed a much less restricted response by the channel structure to the water-flow situations. This structure allowed us to mimic the osmotic pressure-driven water permeation phenomenon. Generally, fixing even a small number of membrane atoms could slightly affect the water transport performance, but when initiated on a molecular scale, it caused no appreciable alteration in the transport mechanisms within the channel [16].

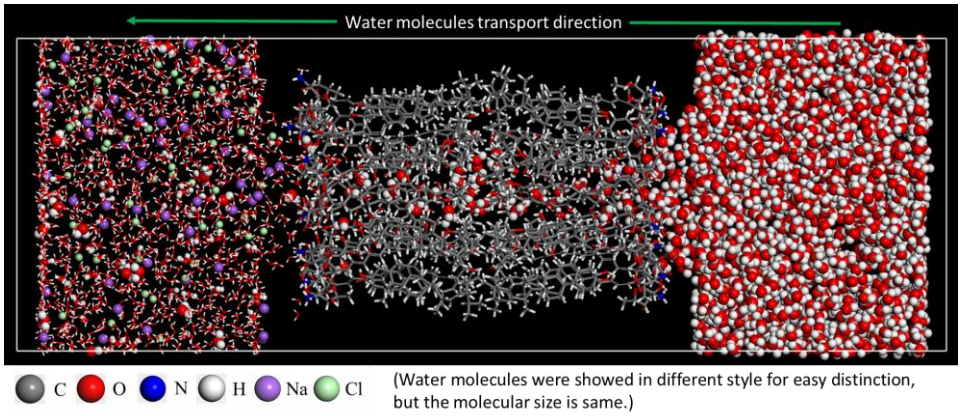

Fig. 5.3 Simulation model of forward osmosis filtration.

5.2.3 Prediction of water permeability

The aim was to illustrate the water molecule transport behavior of an AmBEr channel in the FO process by applying MD simulation. During the calculation period, the number of water molecules in each of the three sections (within AmBEr channel, pure-water, and saltwater reservoirs) was traced and recorded. We obtained the time course curve of water

molecules in the AmBEr channel simulation model as a function of time via the *NVT* MD simulations. The curves that represent the number of water molecules were analyzed to establish the permeation behavior of water molecules in the AmBEr channel. Osmotic pressure was the driving force during the FO simulation period, and was based on calculation using the Van't Hoff equation. Water permeability was based on calculations from the slope of the alteration curve of the water molecules, as shown in Eq. (5.1).

$$Permeability\ [mol\ m/(m^2 s\ Pa)] = \frac{\Delta N\ L}{A\ \Delta t\ \Delta\pi N_A} \qquad (5.1)$$

In Eq. (5.1), ΔN [-] is the change in the number of molecules during a certain period, Δt [s], A [m^2] is the area of a cross-section of the AmBEr channel, $\Delta\pi$ is the mean osmotic pressure during Δt, N_A [mol^{-1}] is Avogadro's number, and L [m] is the channel length, where L = 5.2 x 10^{-9} m. In this study, 100 water molecules were inserted into the AmBEr channel in its initial state as a hydrated water channel, and a 4500-ps calculation period provided diagrams for the time course of the number of water molecules.

5.3 Results and discussion

Water permeability was calculated via alterations in the number of water molecules in a reservoir during FO filtration, as shown in Fig. 5.4(a). During the calculation period, water molecules were transported from the pure-water side to the saltwater side. The water molecules within the pure-water reservoir decreased and those in the saltwater reservoir increased until the simulation system reached a state of equilibrium. The amount of water molecules inside the AmBEr channel remained almost constant at approximately the initial

number. As shown in Fig. 5.4(b) in the enlarged vertical axis, as simulation time increased, the number of water molecules changed and the slope gradually stabilized. The initial slope was adopted to predict water permeability. The values calculated from the slopes of the pure-water and saltwater sides were similar, which explains the steady state of simulation model during the calculation period. The value for water permeability and permeance predicted from the slope of the curve were 1.1×10^{-11} mol m s^{-1} m^{-2} Pa^{-1} and 2.1×10^{-3} mol s^{-1} m^{-2} Pa^{-1}, respectively. It should be noted that this value is a pemeance per one AmB channel area. In order to estimate a realistic permeance, the permeance per one channel should be multiplied by the rate of channel area, or porosity. Experimentally observed water permeance for AmB embedded lipid membranes were 6.7×10^{-5} - 3.7×10^{-4} mol m^{-2} s^{-1} Pa^{-1} [17-19]. From the comparison with previous studies, we can calculate that the porosity of actual lipid membranes was around 3.2~17.6%. Therefore, when we reasonable suppose that the porosity as around 10%, the simulated water permeance seems to show very good agreement with the experimental results.

This novel AmBEr channel is expected to be an artificial water channel that can be inserted into a lipid bilayer to form a biomimetic membrane when a porosity of the membrane surface is assumed to be 1%, computation established the water permeance of AmBEr at approximately 2.1×10^{-5} mol m^{-2} s^{-1} Pa^{-1}. The water flux of a commercial RO membrane (polyamide membrane), as estimated in experimental work, has shown a value of approximately 2 L m^{-2} h^{-1} bar^{-1}, which is equivalent to 3×10^{-7} mol m^{-2} s^{-1} Pa^{-1} [20]. The AmBEr channel membrane is expected to show water permeance performance that is approximately 100-fold higher than that of the commercial RO polyamide membrane. The

simulated permeability should be compared with that of an FO membrane, however, commercial FO membranes are not so common yet. Therefore, we have adopted an RO membrane for comparison. In addition, during a simulation period of 4,500 ps, there was neither permeation nor leakage of ions from the saltwater side through the AmBr channel. This proves that the geometrical channel structures and static electrical interactions effectively rejected the hydrated ions.

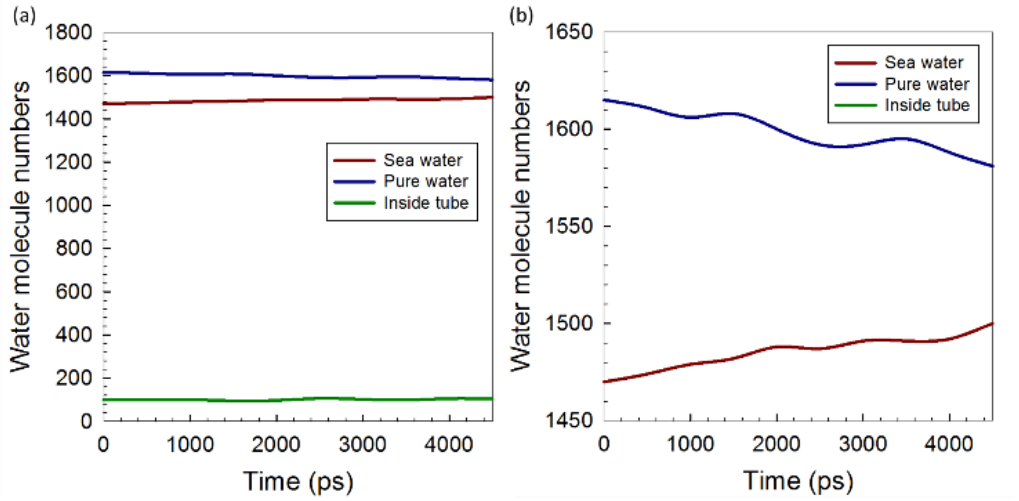

Fig. 5.4 Time course of the number of water molecules during FO simulation using an AmBEr channel. Fig. 5.4 (b) shows an enlarged vertical axis. Data are the same with Fig. 5.4 (a).

5.4 Conclusions

To attain a high level of water permeability performance, a novel AmBEr channel was applied to FO filtration and investigated using dynamic simulation. Molecular simulations allowed inspection of the transport mechanism of molecules within the membrane. The FO filtration phenomenon using the AmBEr channel was successfully described via molecular dynamics simulation. A biomimetic membrane with AmBr channels showed water

permeability that could be as much as 100-fold greater than that of a commercial RO polyamide membrane. This equates to a high likelihood that the AmBEr artificial water channel could usher in a new generation of water treatment membranes. Molecular simulation revealed the unique properties of the AmBEr channel. Computational simulation and analysis at the microscopic level can be a helpful and reliable tool for the design and development of novel materials for biomimetic membranes. The details of the mechanism of ion rejection by such a biomimetic channel can also be applied on a molecular scale and should be helpful in revealing other ion rejection mechanisms.

5.5 Reference

[1] L. Brunet, D.Y. Lyon, K. Zodrow, J.-C. Rouch, B. Caussat, P. Serp, J.-C. Remigy, M.R. Wiesner, P.J. Alvarez, Properties of membranes containing semi-dispersed carbon nanotubes, Environmental Engineering Science, 25 (2008) 565-576.
[2] Y. Le Duc, M. Michau, A. Gilles, V. Gence, Y.M. Legrand, A. van der Lee, S. Tingry, M. Barboiu, Imidazole‐Quartet Water and Proton Dipolar Channels, Angewandte Chemie International Edition, 50 (2011) 11366-11372.
[3] X. Li, K. Yang, J. Su, H. Guo, Water transport through a transmembrane channel formed by arylene ethynylene macrocycles, RSC Advances, 4 (2014) 3245-3252.
[4] S. Fernandez-Lopez, H.-S. Kim, E.C. Choi, M. Delgado, J.R. Granja, A. Khasanov, K. Kraehenbuehl, G. Long, D.A. Weinberger, K.M. Wilcoxen, Antibacterial agents based on the cyclic D, L-α-peptide architecture, Nature, 412 (2001) 452-455.
[5] W. Ding, J. Cai, Z. Yu, Q. Wang, Z. Xu, Z. Wang, C. Gao, Fabrication of an aquaporin-based forward osmosis membrane through covalent bonding of a lipid bilayer to a microporous support, Journal of Materials Chemistry A, 3 (2015) 20118-20126.
[6] H.T. Madsen, N. Bajraktari, C. Hélix-Nielsen, B. Van der Bruggen, E.G. Søgaard, Use of biomimetic forward osmosis membrane for trace organics removal, Journal of Membrane Science, 476 (2015) 469-474.
[7] S. Wang, J. Cai, W. Ding, Z. Xu, Z. Wang, Bio-inspired aquaporinz containing double-skinned forward osmosis membrane synthesized through layer-by-layer assembly, Membranes, 5 (2015) 369-384.
[8] B.L. de Groot, H. Grubmüller, Water permeation across biological membranes: mechanism and dynamics of aquaporin-1 and GlpF, Science, 294 (2001) 2353-2357.
[9] K. Kim, D. Vercauteren, M. Welti, S. Chin, E. Clementi, Interaction of K+ ion with the solvated gramicidin A transmembrane channel, Biophysical journal, 47 (1985) 327-335.
[10] T. Belytschko, S. Xiao, G. Schatz, R. Ruoff, Atomistic simulations of nanotube fracture, Physical Review B, 65 (2002) 235430.

[11] H.-C. Wu, T. Yoshioka, H. Nagasawa, M. Kanezashi, T. Tsuru, D. Saeki, H. Matsuyama, Preparation of cyclic peptide nanotube structures and molecular simulation of water adsorption and diffusion, Journal of Membrane Science, 537 (2017) 101-110.
[12] D. Rigby, H. Sun, B. Eichinger, Computer simulations of poly (ethylene oxide): force field, pvt diagram and cyclization behaviour, Polymer International, 44 (1997) 311-330.
[13] H. Sun, COMPASS: an ab initio force-field optimized for condensed-phase applications overview with details on alkane and benzene compounds, The Journal of Physical Chemistry B, 102 (1998) 7338-7364.
[14] H. Sun, P. Ren, J. Fried, The COMPASS force field: parameterization and validation for phosphazenes, Computational and Theoretical Polymer Science, 8 (1998) 229-246.
[15] W. Gao, F. She, J. Zhang, L.F. Dumée, L. He, P.D. Hodgson, L. Kong, Understanding water and ion transport behaviour and permeability through poly (amide) thin film composite membrane, Journal of Membrane Science, 487 (2015) 32-39.
[16] M. Kotelyanskii, N. Wagner, M. Paulaitis, Molecular dynamics simulation study of the mechanisms of water diffusion in a hydrated, amorphous polyamide, Computational and Theoretical Polymer Science, 9 (1999) 301-306.
[17] V.W. Dennis, N.W. Stead, T.E. Andreoli, Molecular aspects of polyene-and sterol-dependent pore formation in thin lipid membranes, The Journal of general physiology, 55 (1970) 375-400.
[18] R. Holz, A. Finkelstein, The water and nonelectrolyte permeability induced in thin lipid membranes by the polyene antibiotics nystatin and amphotericin B, The Journal of general physiology, 56 (1970) 125-145.
[19] T.E. Andreoli, THE STRUCTURE AND FUNCTION OF AMPHOTERICIN B‐CHOLESTEROL PORES IN LIPID BILAYER MEMBRANES, Annals of the New York Academy of Sciences, 235 (1974) 448-468.
[20] K.P. Lee, T.C. Arnot, D. Mattia, A review of reverse osmosis membrane materials for desalination—development to date and future potential, Journal of Membrane Science, 370 (2011) 1-22.

Chapter 6

Conclusions

The structural characteristics and transport behaviors of two types of candidates of water channel, cyclic peptide nanotube and amphotericin b channel, were thoroughly analyzed via MD and MC. The nanotube/channel morphology, internal diameter, and simulated tunnel volume results revealed the structural properties of molecular model. Hydrogen bond and interaction energy analysis indicated that the affinity between nanotube/channel and water molecular. Afterwards, the water molecular transport performance within nanotube/channel could be studied from diffusion and sorption behavior, and the water permeability would be calculated by solution-diffusion model. Further, these two types of artificial water channel were applied on forward osmosis simulation model. The performance of water permeability and ion rejection ability was introduced.

From the results, the nano-scale tunnel provide enough space for water molecule transport and the affinity analysis suggested that the hydrophobic tunnel could assist water molecule diffusion. In transport performance, two types of simulation model showed the comparable water permeability property. The prediction value is much higher than commercial reverse osmosis membrane. In the other hand, the permeability performance from forward osmosis simulation model was much lower than the results from solution-diffusion model, because of the resistance of entrance. However, the result suggested the high ion rejection ability during the calculation period. From the above description, we could see the potential of cyclic

peptide nanotube and amphotericin b to instead aquaporin, and also the feasibility of forward osmosis application.

In summary, in order to find the suitable material for artificial water channel, molecular simulation technique was adopted to investigate the properties of candidate materials under atom scale in this work. Computational simulation and analysis at the microscopic level can be a helpful and reliable tool for the design of novel materials for biomimetic membranes. The details of the mechanism of ion rejection by such a biomimetic channel can also be applied on a molecular scale and should be helpful in revealing other ion rejection mechanisms. In simple word, molecular simulation shows great promise as a method that could assist in the design of novel material.

List of publications:

Wu, H. C., Yoshioka, T., Nagasawa, H., Kanezashi, M., Tsuru, T., Saeki, D., & Matsuyama, H. (2017). Preparation of cyclic peptide nanotube structures and molecular simulation of water adsorption and diffusion. Journal of Membrane Science, 537, 101-110.

Wu, H. C., Yoshioka, T., Nakagawa, K., Shintani, T., Tsuru, T., Saeki, D., Chen, Y. R., Tung, K. L., & Matsuyama, H. (2017). Water transport and ion rejection investigation for application of cyclic peptide nanotubes to forward osmosis process: A simulation study. Desalination, 424, 85-94.

Wu, H. C., Yoshioka, T., Nakagawa, K., Shintani, T., Tsuru, T., Saeki, D., Shaikh, A. R., & Matsuyama, H. (2018). Preparation of Amphotericin B-Ergosterol structures and molecular simulation of water adsorption and diffusion. Journal of Membrane Science, 545, 229-239.

Wu, H. C., Yoshioka, T., Nakagawa, K., Shintani, T., Tsuru, T., Saeki, D., & Matsuyama, H. (2017). Applying Amphotericin B-Ergosterol in Forward Osmosis: a simulation study, Membrane, 42(6), 250-254

Doctoral Dissertation, Kobe University

“A molecular simulation study on structural properties and performance investigation of biomimetic artificial water channels”, 148 pages

Submitted on 01, 16, 2018

The date of publication is printed in cover of repository version published in Kobe University Repository Kernel.